SHOALING AND BREAKING RANDOM WAVES
ON A 1:35 LABORATORY BEACH

Glenn D. Bowen
and
James T. Kirby

Research Report No. CACR-94-14

June 1994

CENTER FOR APPLIED COASTAL RESEARCH
Ocean Engineering Laboratory
University of Delaware
Newark, Delaware 19716

Abstract

Normally incident random wave trains were generated on a 1:35 wooden laboratory beach for a variety of H_{rms} and T_p conditions. Capacitance wave gages were used to measure the free surface oscillation at 47 locations (44 along the slope), providing a detailed view of the surfzone. In addition to providing a complete data set for analysis and comparison to numerical model output, the experiments resulted in a verification of the performance of the recently constructed precision wave flume and associated hardware.

Due to the enclosed nature of the tank and the wooden beach, low frequency energy not associated with wave groups was observed. Statistically significant seiching was seen to occur, raising energy levels in the low frequency modes to values similar to those measured in field experiments. Wave height transformation, energy spectra, and wave shape are calculated and analyzed.

This report was submitted by the first author to the University of Delaware in partial fullfillment of the requirements for the degree of Master of Civil Engineering.

Contents

List of Figures

List of Tables

Chapter 1

Introduction

The basis of this thesis was the generation of random wave trains on a 1:35 wooden laboratory beach in the precision wave flume at the University of Delaware's Center for Applied Coastal Research. The procedures involved in input signal preparation, wave gage calibration, wave generation, data recording, data reduction and analysis will be explained.

These experiments are intended to provide a detailed picture of wave height transformation (to be compared to that of the energetics based model of Thornton and Guza (1983)) and spectral evolution as they occur in the precision wave flume. Laboratory data sets are in general less expensive to collect than field data sets, but there are physical phenomena that occur in the laboratory that do not occur in the field, and due to scaling effects there are quantities measured in the laboratory that are out of proportion to naturally occurring values in the field. Thus, the basic computed wave characteristics will be compared to the results of larger scale studies (in both the laboratory and the field) to judge the appropriateness of using data collected in an idealized laboratory condition *vs.* that collected under natural conditions.

The behavior of the low frequency amplitudes throughout the flume will be carefully considered, as will be the wave shape parameters. Previous numerical spectral shoaling and breaking models, while closely approximating wave height transformation and spectral evolution, have not provided accurate predictions of wave shape.

Chapter 2

Experimental Procedure

2.1 Irregular Wave Trains

2.1.1 Theoretical Background

The numerical model used to compute the paddle displacement time series for generation of the irregular wave trains is based on that of Cox *et al.* (1991). First the desired JONSWAP target wave spectrum is generated according to

$$S_J = S_P(f)\Phi_{PM}(f/f_p)\Phi_J(f, f_p, \gamma, \sigma), \tag{2.1}$$

where the Phillips formula for equilibrium range

$$S_P(f) = \alpha g^2(2\pi)^{-4} f^{-5}, \tag{2.2}$$

the Pierson-Moskowitz shape function

$$\Phi_{PM}(f/f_p) = \exp[(-5/4)(f/f_p)^{-4}], \tag{2.3}$$

and the JONSWAP shape function

$$\Phi_J(f, f_p, \gamma, \sigma) = \exp\left\{\ln(\gamma)\exp[-(f - f_p)^2/2\sigma^2 f_p^2)]\right\} \tag{2.4}$$

with σ and γ being variable coefficients (Cox *et al.*, 1991). The JONSWAP spectrum is extended to finite depth by applying the transformation factor of Kitaigorodskii *et al.* (1975)

$$\Phi_K(\omega_H) = \tanh^2(kh)\left[1 + \frac{2kh}{\sinh 2kh}\right]^{-1} \tag{2.5}$$

to define the TMA spectral form of

$$S_{TMA} = S_J \Phi_K(\omega_H). \tag{2.6}$$

Table 2.1: Input spectra parameters

H_{rms}	7 *cm*	8 *cm*	9 *cm*
$f_p(Hz)$	0.5	0.225	0.225
n	16384	16384	16384
$T_{max}(s)$	1024	1024	1024
γ	3.3	3.3	3.3

Then the transfer function for a piston-type wave paddle

$$F_1(f,h) = \frac{H}{2e} = \frac{4\sinh^2(2\pi h/L)}{4\pi h/L + \sinh(4\pi h/L)} \tag{2.7}$$

(Goda, 1985), where $2e$ equals the maximum paddle stroke from front to back (1.0 meters for the precision wave flume), is applied to the TMA target wave spectrum to develop the paddle displacement spectrum. A random phase scheme

$$\eta(t) = \sum_{n=1}^{N/2} [2S(f_n)\Delta f]^{1/2} \cos(2\pi f_n t + \phi_n) \qquad for\ 0 \leq t < t_{\max} \tag{2.8}$$

where ϕ_n are random phase angles distributed between 0 and 2π (Elgar *et al.*, 1985), is then applied to the paddle displacement spectrum to develop the paddle displacement time series. This modeling was completed on the Sun network system at the University of Delaware's Center for Applied Coastal Research.

2.1.2 Input Spectra

The three input spectra chosen are shown in Figures 2.1 through 2.3. Input parameters for each case are listed in Table 2.1. The three cases are hereinafter referred to as the 7 *cm*, 8 *cm*, and 9 *cm* runs, named to describe the chosen value of H_{rms}. The one-sided input spectra were 16384 points long with a Nyquist frequency of 16 *Hz*. The paddle displacement time series generated were 32768 points in length, of which the last point was deleted as the largest file the wave generation computer would accept was 32767 (2^{15}-1) points. Relaying the signal to the wave paddle at a rate of 32 *Hz* resulted in an experimental trial with a duration of 1024 seconds ($\cong$17 minutes). The first two minutes of the 9 *cm* paddle displacement time series is shown in Figure 2.4.

As Goda (1985) points out, it is important to verify the paddle transfer function by comparing the chosen input target spectrum to measured data. Figure 2.5 compares the 8 *cm* input target spectrum and the measured spectrum 3.0 meters from the wave paddle. The agreement shown verifies the paddle transfer function, although it may be noted that the build up of low frequency motion throughout the tank appears to be robbing some of the energy from the spectral peak.

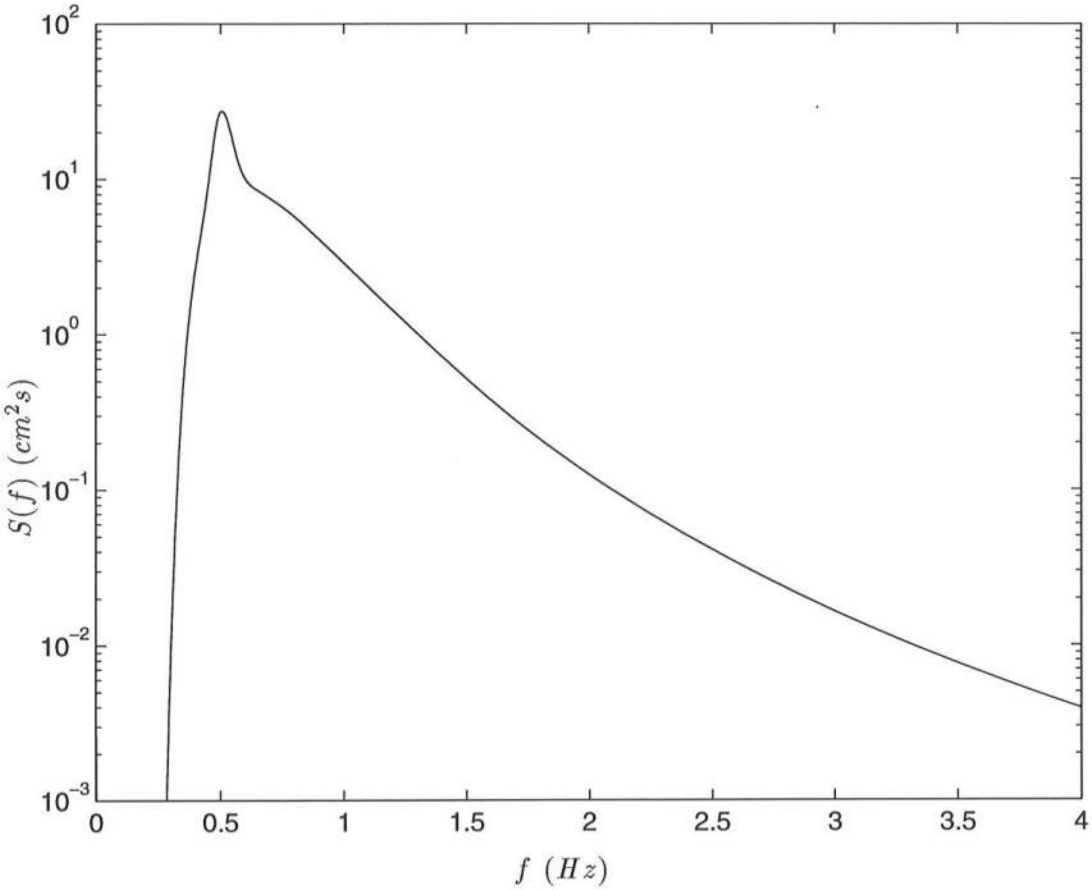

Figure 2.1: Target input spectrum, 7 *cm* run

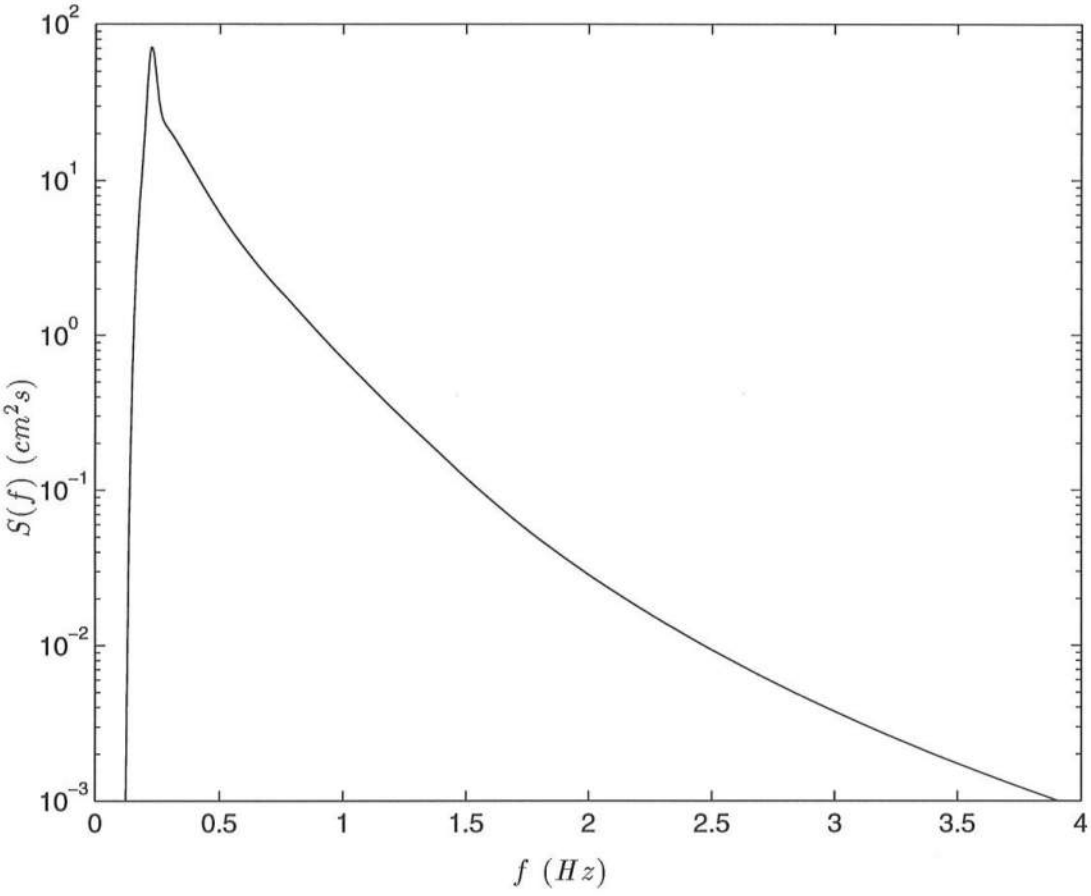

Figure 2.2: Target input spectrum, 8 *cm* run

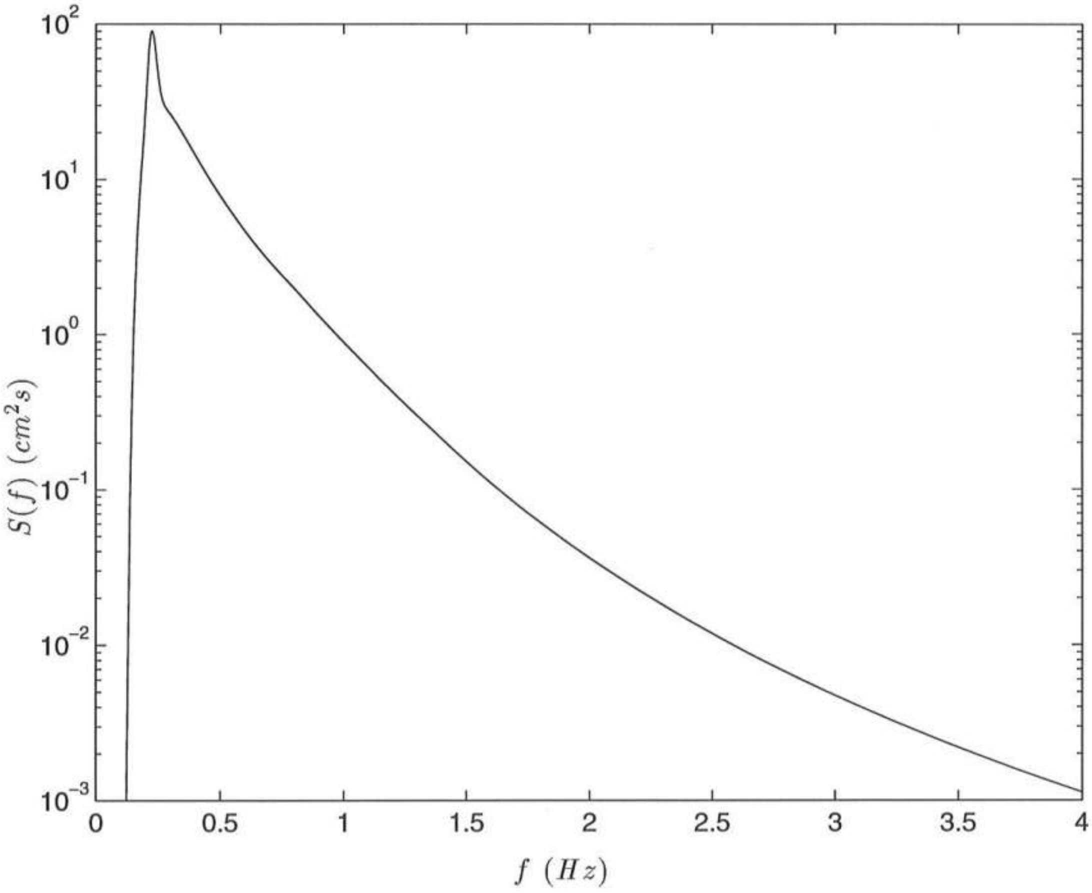

Figure 2.3: Target input spectrum, 9 *cm* run

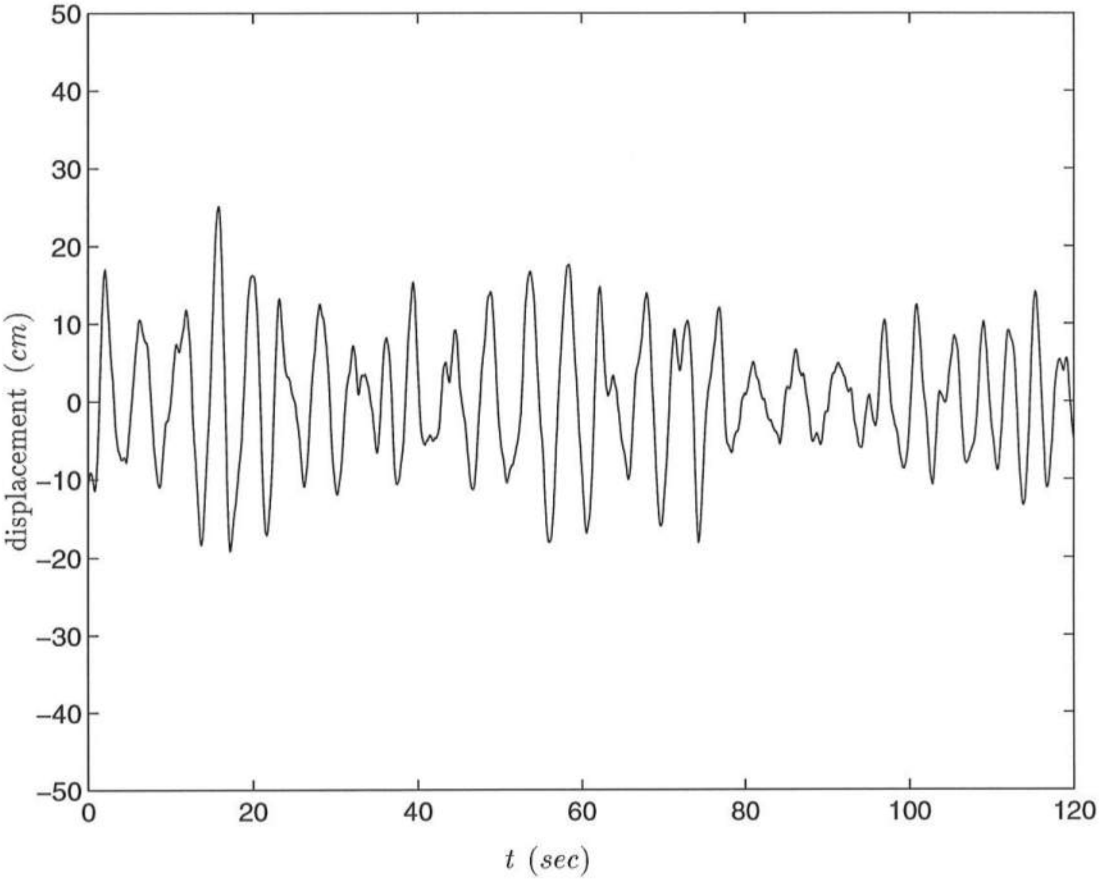

Figure 2.4: Paddle displacement time series, 9 *cm* run, first two minutes

2.2 Precision Wave Flume

The experimental runs were conducted in a newly constructed precision wave flume at the University of Delaware's Center for Applied Coastal Research. The physical dimensions of the flume are: 30 meters long, .8 meters deep, and .6 meters wide. For these experiments, a 1:35 wooden beach was installed beginning at a point 11.5 meters shoreward of the piston-type wave paddle. A diagram is shown in Figure 2.6. Eight-foot long wooden panels were connected to and supported by a unistrut frame. During installation, the unistrut frame was adjusted under each panel to limit error in the beach slope to $\pm .25$ centimeters. Ballast was placed on the legs of the frame to anchor it to the tank floor. Some areas of the beach experienced periodic deflections as the waves passed. These areas were pinned to the unistrut frame to correct this phenomenon to the extent possible. In addition, over time some of the panels experienced a slight warping in the cross-shore direction.

2.2.1 Wave Generation

The paddle displacement time series files were downloaded from the Sun system to floppy disc and transferred to the IBM PC-AT which controlled the wave paddle. Calibration of the wave paddle yielded a calibration constant of -18.367 volts per meter. The wave generation program read in the paddle displacement time series and used the paddle constant to convert the time series points into voltages which the attached Data Translation DT2801 board sent as an input signal to the paddle.

2.2.2 Data Acquisition

Ten capacitance wave gages were used during experimental trials to record the free surface oscillation. The design of these gages originated at the University of Florida. The gages sent a voltage signal, developed as the wetted length of the measuring wire varied during the wave train, to the data acquisition computer.

Attached to each gage's measuring wire was a stepper motor that was used to adjust the elevation of the measuring wire relative to the water surface during calibration. The ten stepper motors were connected to an electronic control box that consisted of three separate control units, each capable of controlling 4 gages simultaneously. The direction of movement was selected by a toggle switch.

The data acquisition computer was an IBM PS2. Labtech Notebook software was used to record the voltages measured by the gages during the experimental trials.

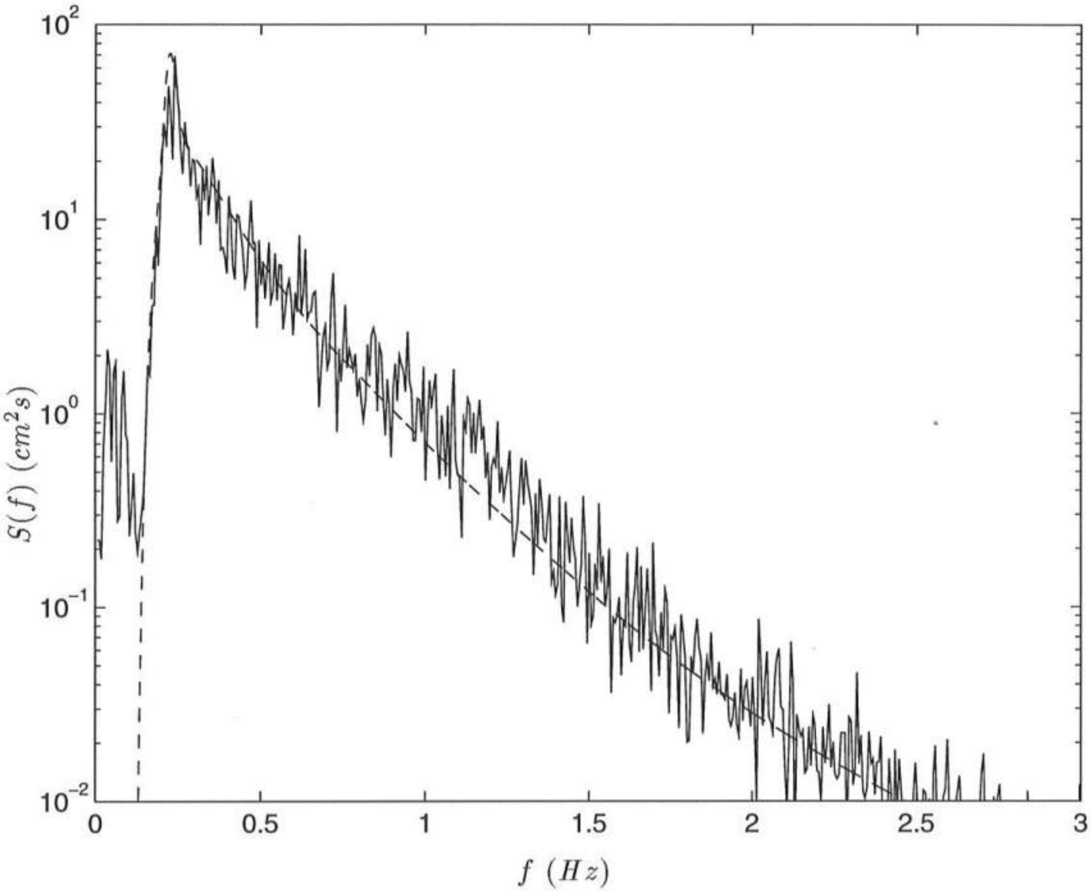

Figure 2.5: Target input spectrum, 8 *cm* run, *vs.* measured spectrum, location=3.0 *m*, *h*=.44 *m*

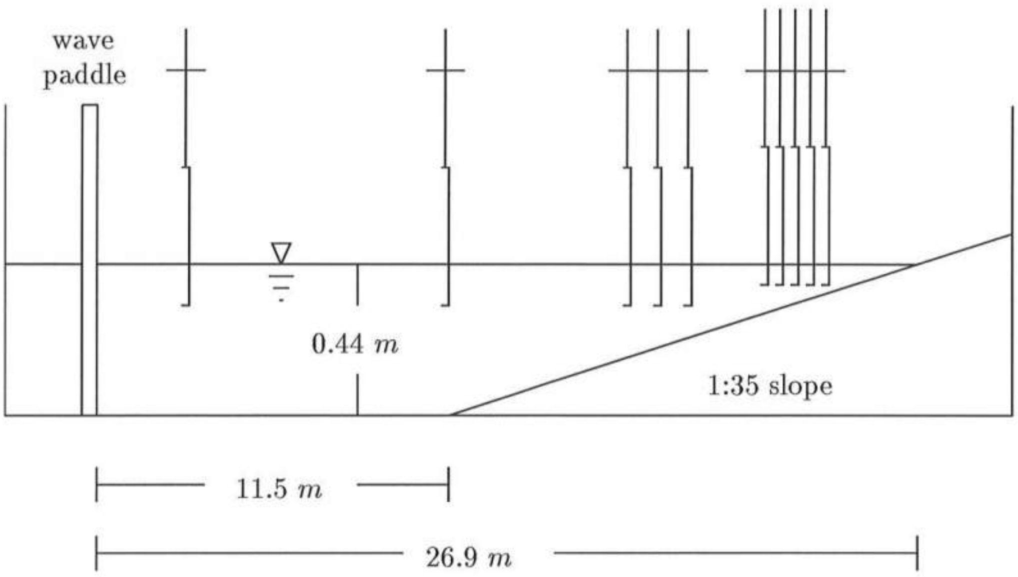

Figure 2.6: Precision wave flume diagram (distorted scale 1H=10V)

2.3 Experimental Trials

2.3.1 Wave Gage Calibration

Before experimental trials were conducted each day, the ten gages were calibrated. The electronic control box contained an amplifier signal conditioner, which was used to set the gain to .25 volts per centimeter. Choosing this value fully utilized the 10 volt monitoring range over the 40 centimeter length of measuring wire. Physical constraints allowed only the lower 30 centimeters of the measuring wire to be calibrated.

The data acquisition computer was used in conjunction with the electronic control box and stepper motors to record voltages for each gage at 1 centimeter increments over the possible 30 centimeter range. First, the wave staffs were adjusted so that 12 centimeters of measuring wire extended below the surface, the normal positioning during experimental trials. The wires were then moved down into the water 1 centimeter at a time for 18 centimeters, back up for 30 centimeters, and finally back down for 12 centimeters. At each elevation, 100 voltage readings were taken for each gage. The 100 values for a gage were averaged to produce a value for that gage at that elevation. During the calibration process, each elevation was visited twice. The two values computed were averaged and written to the output file.

2.3.2 Summary of Wave Trains Generated

Experimental trials were conducted on 5 days in the spring of 1992. One day's experimentation consisted of calibrating the gages and setting them in position along the flume, then generating the irregular wave trains for the 7 *cm*, 8 *cm*, and 9 *cm* runs and recording data. Periodic checks between trials revealed that the drift in the gain was miniscule over the time required to complete the day's experimentation. The same procedure was used each day, with the gages set in different positions along the flume. Tables 2.2 and 2.3 list the dates experiments took place, and the gage placement locations, as measured from the wave paddle.

Data was recorded along the flat bottom, at the toe of the slope, and along the slope as far shoreward as was possible. Before gages were positioned at locations greater than 22.5 meters shoreward of the wave paddle, the electronic control box was used to raise the measuring wires, as the water depth was less than 12 centimeters in that region. This resulted in an apparent water height being measured during the experimental trials which was lower than the actual height. This situation was remedied by noting the wire displacement and adding this amount back in to the wave record during data reduction.

The Labtech Notebook program sampled data at an overall rate of 250 Hz, or 25 Hz per gage. The output wave voltage record file consisted of 10 columns, one per gage, of 25501 points each. At the end of the day, the calibration data file, and the three Labtech Notebook generated output wave voltage record files were downloaded from the data acquisition computer to floppy disc, and transferred to the Sun system for reduction and analysis.

Table 2.2: Experimental trials conducted

Date	Gage	Location (m)	h (m)
18 Mar 1992	01	3.00	0.440
	02	12.50	0.411
	03	12.72	0.405
	04	13.22	0.391
	05	13.50	0.383
	06	13.72	0.377
	07	13.97	0.369
	08	14.22	0.362
	09	14.50	0.354
	10	14.76	0.347
07 Apr 1992	01	3.00	0.440
	02	15.50	0.326
	03	15.72	0.319
	04	16.22	0.305
	05	16.50	0.297
	06	16.72	0.291
	07	16.97	0.284
	08	17.22	0.277
	09	17.50	0.269
	10	17.76	0.261
08 Apr 1992	01	11.50	0.440
	02	18.50	0.240
	03	18.72	0.234
	04	19.22	0.219
	05	19.50	0.211
	06	19.72	0.205
	07	19.97	0.198
	08	20.22	0.191
	09	20.50	0.183
	10	20.76	0.175

Table 2.3: Experimental trials conducted (continued)

Date	Gage	Location (m)	h (m)
20 Apr 1992	01	7.75	0.440
	02	21.50	0.154
	03	21.97	0.141
	04	22.22	0.134
	05	22.50	0.126
	06	22.72	0.119
	07	22.97	0.112
	08	23.22	0.105
	09	23.50	0.097
	10	23.76	0.090
28 Apr 1992	01	11.50	0.440
	02	23.50	0.097
	03	23.97	0.084
	04	24.22	0.077
	05	24.50	0.069
	06	24.72	0.062
	07	24.97	0.055
	08	25.22	0.048
	09	25.50	0.040
	10	25.76	0.033

Chapter 3

Data Analysis

3.1 Data Reduction

3.1.1 Wave Gage Calibration Curves

The first step taken in data reduction was determining best fit curves for the wave gage calibration data. The capacitance gages used here are normally considered linear; however, analysis of the data revealed that a second order fit actually produced the lowest least square errors. This result should not be interpreted as having physical significance though, as Table 3.1, which lists the computed calibration coefficients for one day's experiments, shows that the calibration coefficients for the second order term are 2 orders of magnitude lower than those for the first order term. Figure 3.1, which shows a computed second order gage calibration curve plotted against measured values, is typical of all of the gages, and attests to the linearity of the calibration curves. The coefficients computed by the second order fit were used in the conversion process.

3.1.2 Raw Data Conversion

Once the wave gage calibration coefficients are known, they are applied to the raw voltage data recorded during the experimental trials to convert it into surface displacement data. An in-house program converted one ten column Labtech Notebook generated voltage data file into ten surface displacement time series files, one for each gage, for ease of further analysis. Each resulting time series file has one column of 25501 surface displacement points.

The time series files were each assigned a 9 character filename. The H_{rms} value is assigned to character 1. Character 2 is a place holder. The gage location in centimeters as measured from the wave paddle is assigned to characters 3 through 6. Character 7 is also a place holder. The gage number is assigned to characters 8 and 9. For example, file 8_1950_05 contains the time series of the 8 cm run as recorded by gage 05 at a location 1950 centimeters from the wave paddle. As some filenames are ambiguous (7_0300_01 occurred on March 18

Table 3.1: Calibration coefficients, 18 Mar 1992

2^{nd} order fit				
gage	C_0	C_1	C_2	RMS error
01	-14.92	3.57	0.037	0.29
02	-14.14	3.38	0.045	0.16
03	-14.22	3.32	0.059	0.17
04	-15.00	3.59	0.037	0.31
05	-14.67	3.32	0.084	0.25
06	-14.48	3.50	0.027	0.21
07	-12.17	2.82	0.049	0.00
08	-15.57	3.80	0.024	0.49
09	-15.14	3.64	0.035	0.34
10	-15.48	3.72	0.039	0.42
1^{st} order fit				
gage	C_0	C_1		RMS error
01	-15.59	3.93		0.44
02	-14.92	3.81		0.29
03	-15.26	3.88		0.37
04	-15.69	3.95		0.47
05	-16.14	4.10		0.59
06	-14.98	3.77		0.31
07	-13.00	3.30		0.03
08	-15.96	4.01		0.60
09	-15.77	3.98		0.49
10	-16.20	4.09		0.61

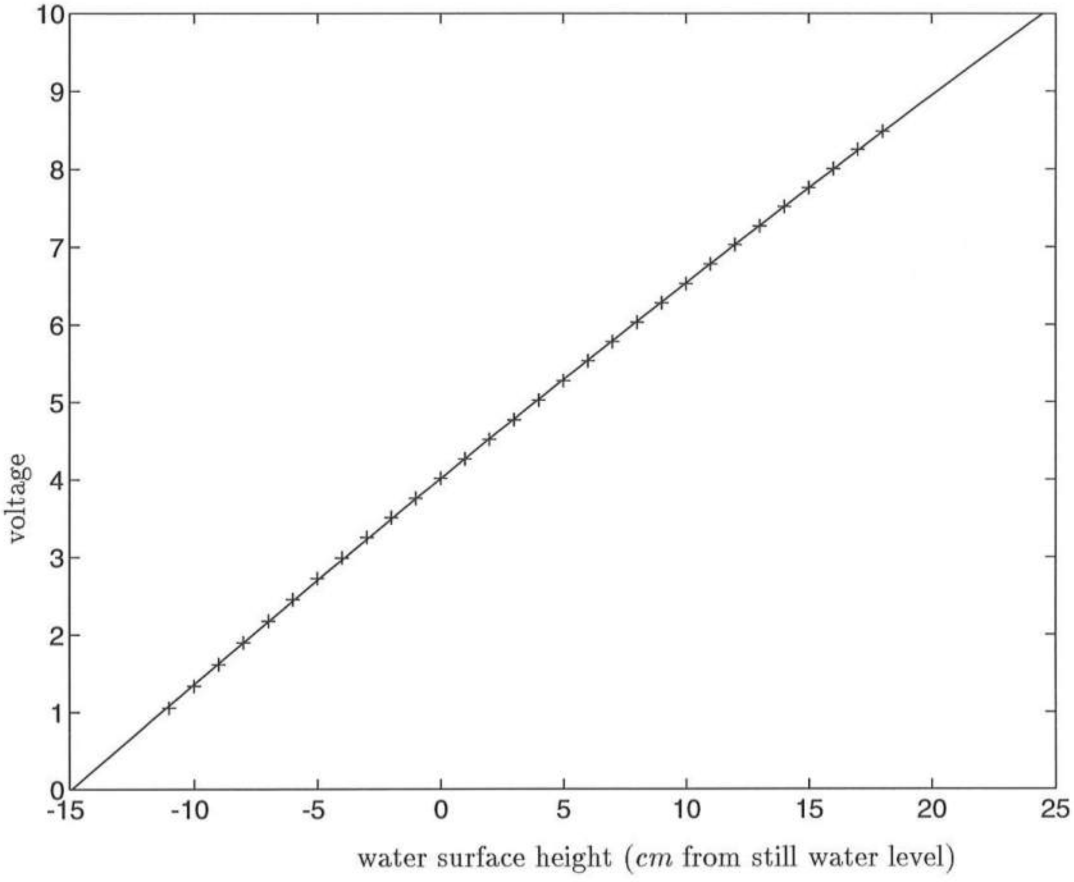

Figure 3.1: Calibration curve for gage 1, 18 Mar 1992 (2^{nd} order fit)

and April 7, 1992), each day's data (and calibration file) is stored in a subdirectory named to reflect the experiment's date. This subdirectory is further divided into four subdirectories, one containing the calibration data, and the other three each containing the data from one of the day's experimental trials. As computed results were also stored in the data subdirectories, this arrangement avoided one overcrowded directory

During this conversion process, the data files for gages which were located shoreward of a point 22.5 meters from the wave paddle were corrected to relate the actual water surface displacement relative to the still water level. This was done by adding back in to the surface displacement record the manual displacement corresponding to the experimental conditions described in Section 2.3.2.

3.2 Basic Data Analysis

3.2.1 Measured Spectra

Once the surface displacement time series are known, Fourier analysis is applied to develop the energy spectra. Figures 3.2 through 3.7 show the spectra through the shoaling and breaking regions for the 7 cm, 8 cm, and 9 cm runs.

In computing the spectra shown in these figures, the first 925 surface displacement points in the time series were ignored, to allow the wave trains to travel the length of the tank. The remaining 24576 points were separated into 24 segments of 1024 points each, fast Fourier transformed (FFT'ed), and ensemble averaged to produce a 512 point one-sided energy spectrum. The spectra have a Nyquist frequency of 12.5 Hz, with the first 2.5 Hz being shown.

In all three runs, the energy in the low frequency modes (less than one half of the peak frequency) monotonically increases in the shoreward direction. Energy is transferred from the spectral peak to the higher frequency modes as the wave train travels over the flat bottom and begins up the slope. This loss takes place slowly in the 7 cm run, and more quickly in the 8 cm and 9 cm runs. In all three runs, the second harmonic of the spectral peak is seen developing as the wave trains travel through the shoaling region (Figures 3.2, 3.4, and 3.6). In the 8 cm and 9 cm runs, the evolution of the third harmonic is seen also during shoaling (Figures 3.4 and 3.6). The third harmonic is not witnessed in the 7 cm run (Figure 3.2). As the waves enter the surfzone and begin to break, the entire spectrum loses energy, with the exception of the low frequency modes (Figures 3.3, 3.5, and 3.7). In the inner surfzone, the spectra for the 8 cm and 9 cm runs are indistinguishable. Thus the 9 cm run must have lost more energy during the breaking process.

3.2.2 Wave Shape Characteristics

Laboratory and field studies have documented the evolution of a sinusoidal wave shape in deep water into a skewed wave shape while shoaling, then into an asymmetric (sawtooth)

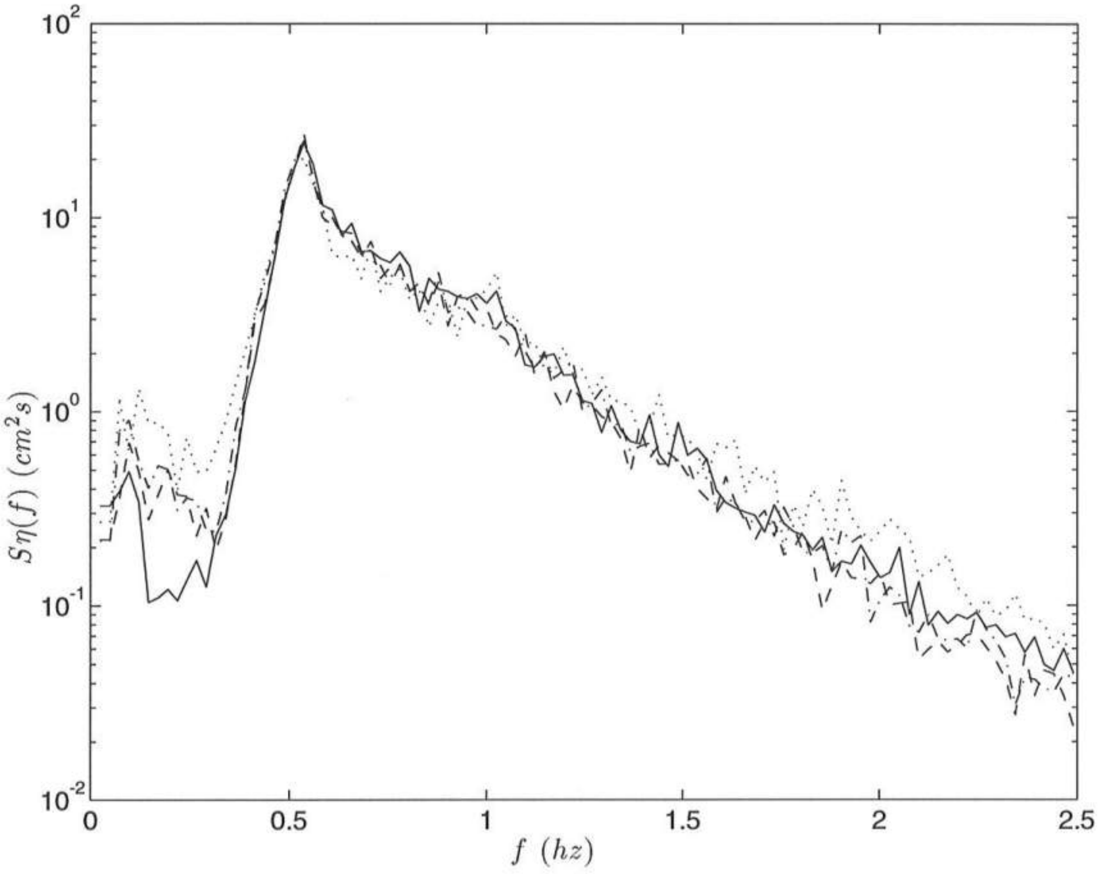

Figure 3.2: Shoaling spectra, 7 *cm* run; (—) x=3.0 m, *h*=.44 m; (- - -) x=11.5 m, *h*=.44 m; (-·-·-) x=14.76 m, *h*=.347 m; (· · · · ·) x=18.5 m, *h*=.24 m

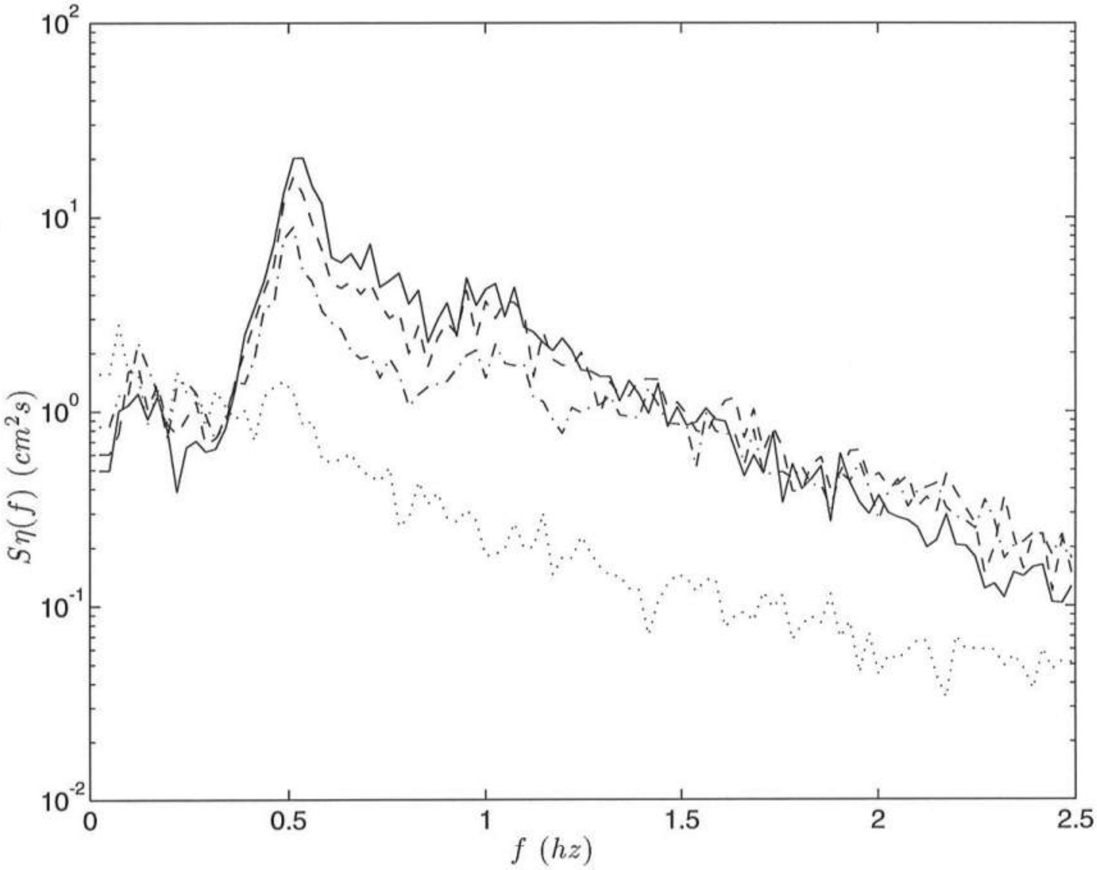

Figure 3.3: Breaking spectra, 7 *cm* run; (——) x=19.5 m, h=.211 m; (- - -) x=21.5 m, h=.154 m; (-·-·-) x=23.5 m, h=.097 m; (· · · · ·) x=25.5 m, h=.04 m

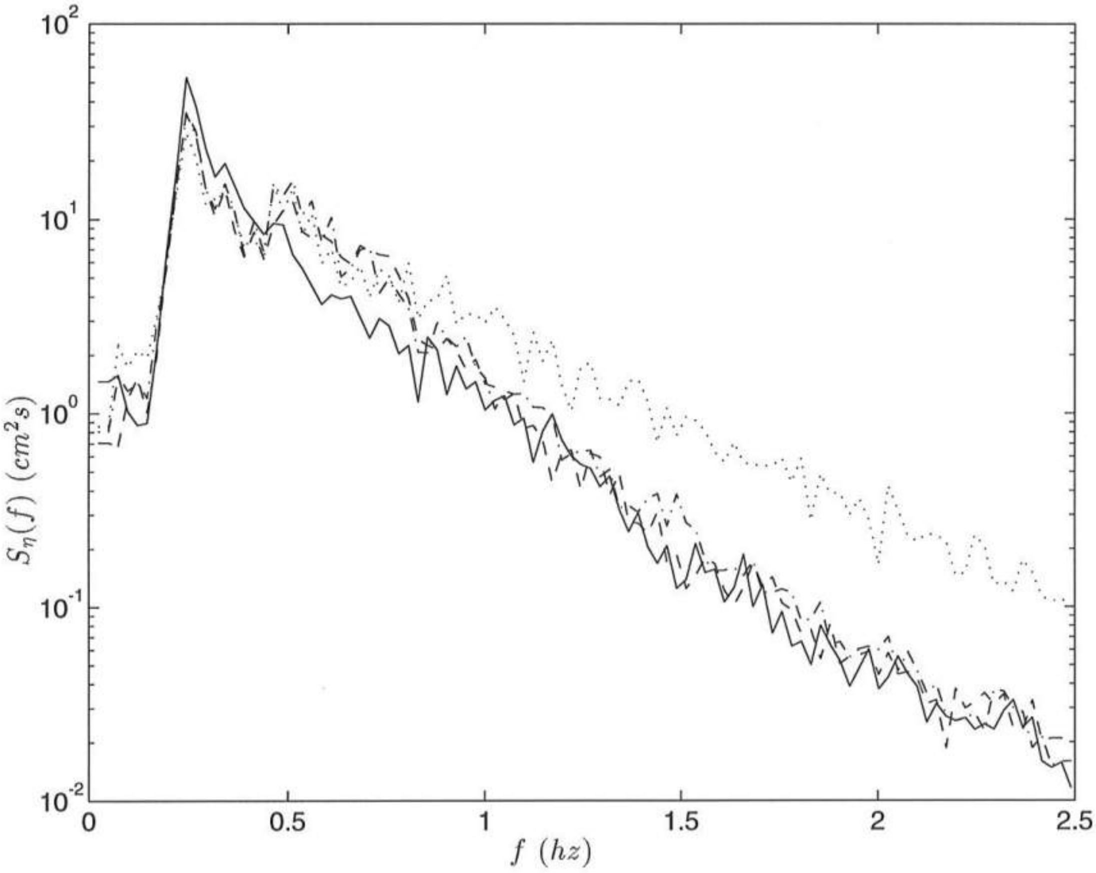

Figure 3.4: Shoaling spectra, 8 *cm* run; (——) x=3.0m, *h*=.44 m; (- - -) x=11.5 m, *h*=.44 m; (-·-·-) x=14.76 m, *h*=.347 m; (· · · · ·) x=18.5 m, *h*=.24 m

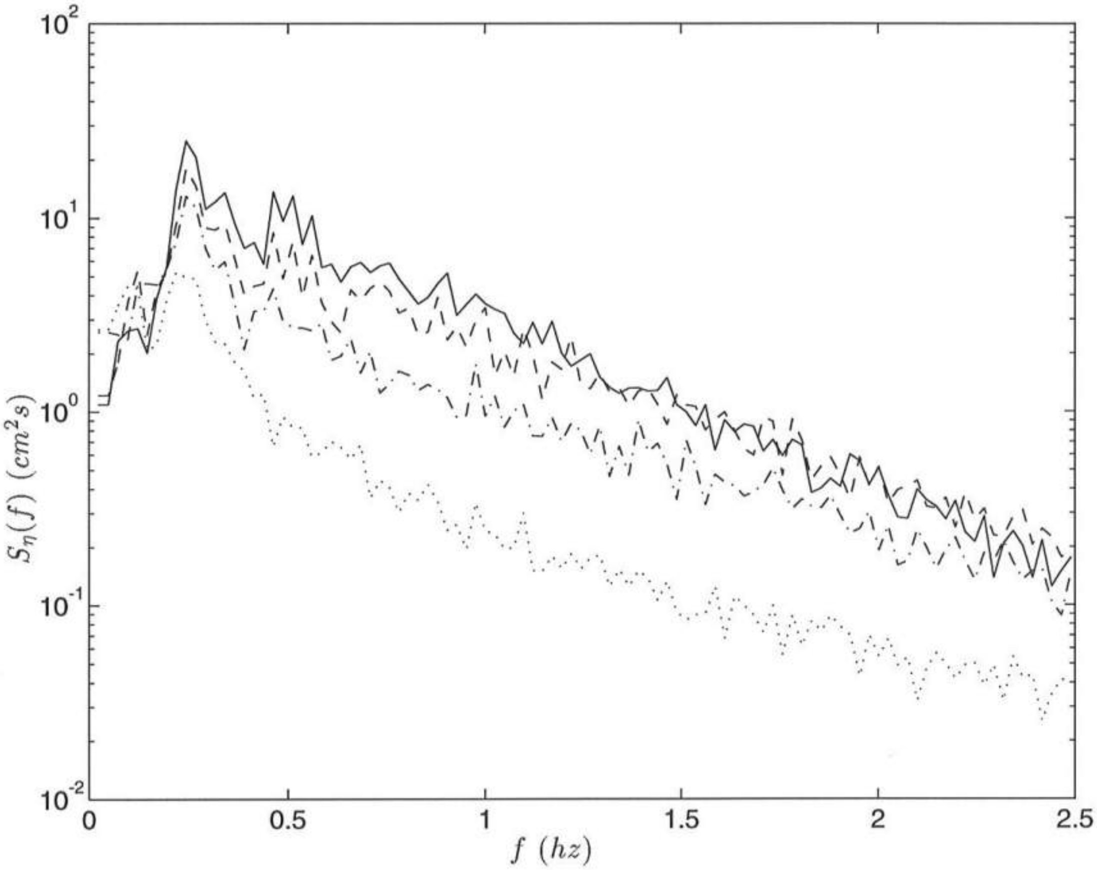

Figure 3.5: Breaking spectra, 8 *cm* run; (——) x=19.5 m, h=.211 m; (- - -) x=21.5 m, h=.154 m; (-·-·-) x=23.5 m, h=.097 m; (· · · · ·) x=25.5 m, h=.04 m

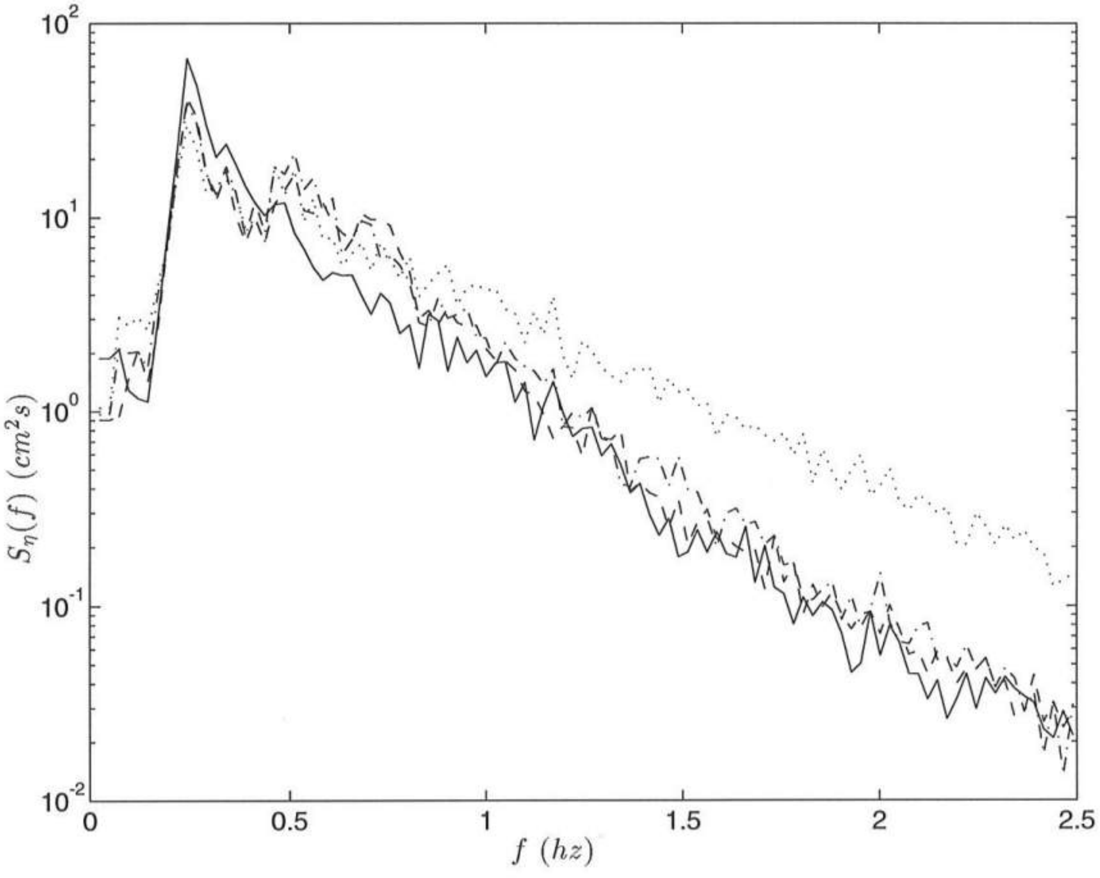

Figure 3.6: Shoaling spectra, 9 *cm* run; (——) x=3.0 m, h=.44 m; (- - -) x=11.5 m, h=.44 m; (-·-·-) x=14.76 m, h=.347 m; (· · · · ·) x=18.5 m, h=.24 m

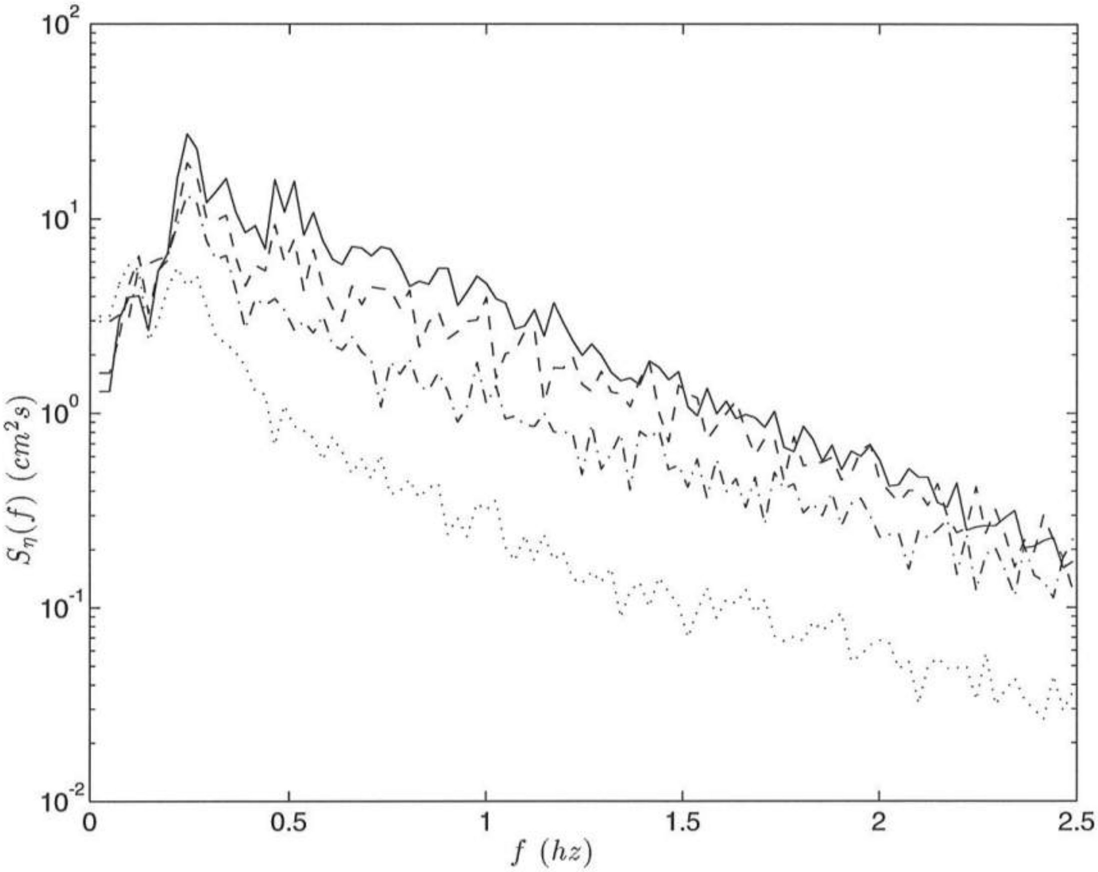

Figure 3.7: Breaking spectra, 9 *cm* run; (—) x=19.5 m, h=.211 m; (- - -) x=21.5 m, h=.154 m; (-·-·-) x=23.5 m, h=.097 m; (· · · · ·) x=25.5 m, h=.04 m

wave shape as the surfzone is approached. A skewed wave has a sharp peak and a flat trough, and progresses into an asymmetric wave with a steeply sloping front face and long flat tail. Skewness is computed statistically as

$$\frac{E[\eta^3]}{E[\eta^2]^{3/2}}. \tag{3.1}$$

Asymmetry is computed statistically as

$$\frac{E[H(\eta)^3]}{E[\eta^2]^{3/2}} \tag{3.2}$$

where $H(\eta)$ is the Hibert transform of the surface displacement time series.

Figures 3.8 through 3.10 show the shoreward evolution of the skewness and asymmetry values for the 7 *cm*, 8 *cm*, and 9 *cm* runs. The results for the 8 *cm* and 9 *cm* runs are nearly identical (Figures 3.9 and 3.10). Comparatively, the 7 *cm* run is not as skewed and reaches its peak skewness further up the slope. The 7 *cm* run achieves nearly the same level of asymmetry, but does so in a more drastic manner than the gradual build up seen in the 8 *cm* and 9 *cm* runs.

3.2.3 Wave Height Transformation

Wave height transformation is commonly observed by calculating the value of H_{rms} through the shoaling and breaking region. Thornton and Guza (1983) propose an average energy flux balance equation

$$\frac{\partial EC_{gx}}{\partial x} = \langle \epsilon_b \rangle + \langle \epsilon_f \rangle \tag{3.3}$$

with a bore dissipation term of

$$\langle \epsilon_b \rangle = \frac{3\pi}{16} \rho g \frac{B^3 \overline{f}}{\gamma^4 h^5} H_{rms}^7 \tag{3.4}$$

and a frictional dissipation term of

$$\langle \epsilon_f \rangle = \rho c_f \frac{1}{16\pi} \left[\frac{2\pi f H_{rms}}{\sinh kh} \right]^3 \tag{3.5}$$

where c_f is the bed friction coefficient, with an accepted value of 0.01 (Shemdin *et al.*, 1978). The frictional dissipation term $\langle \epsilon_f \rangle$ is not considered in the analysis, as it is negligible compared to the bore dissipation term $\langle \epsilon_b \rangle$, leaving

$$\frac{\partial EC_{gx}}{\partial x} = \langle \epsilon_b \rangle. \tag{3.6}$$

Laboratory data for the 7 *cm*, 8 *cm*, and 9 *cm* runs, plotted *vs.* the numerical forward stepping scheme solution to Equation 3.6, are presented in Figures 3.11 through 3.13. The

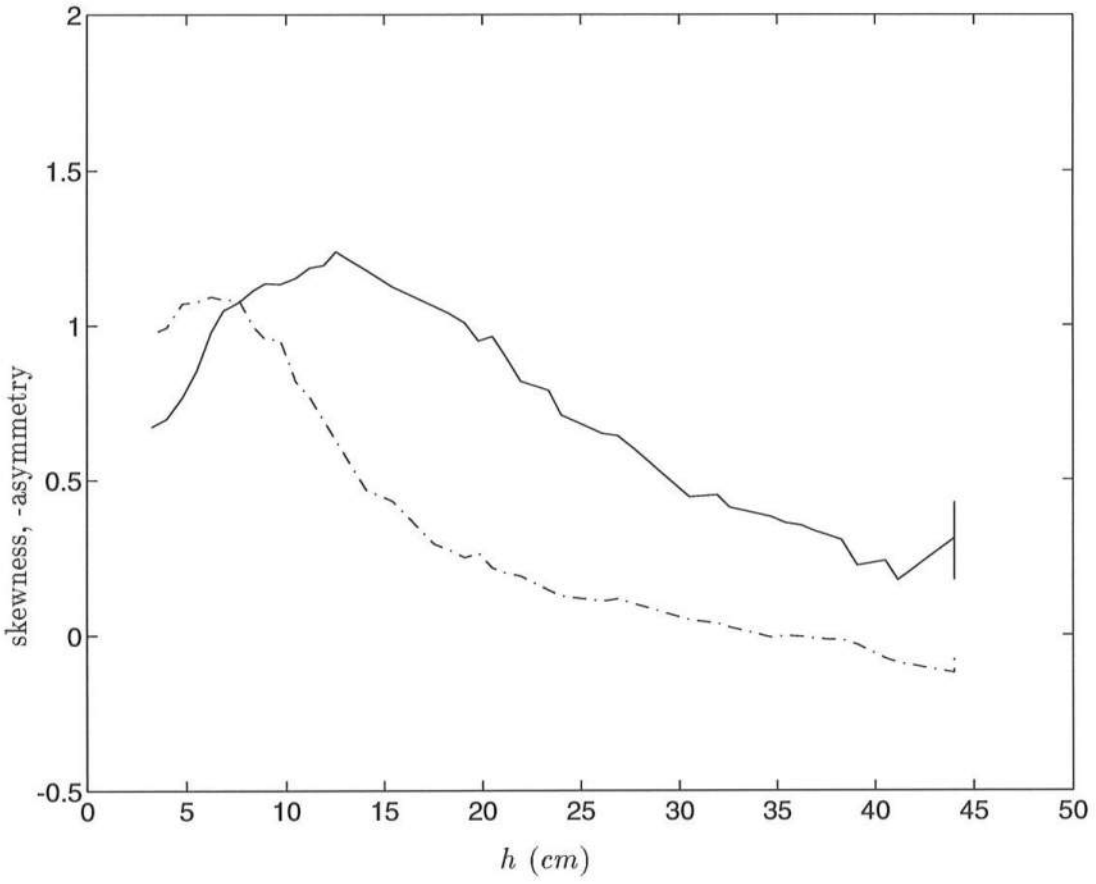

Figure 3.8: Shoreward evolution of skewness and asymmetry, 7 *cm* run; (——) skewness; (-·-·-) asymmetry

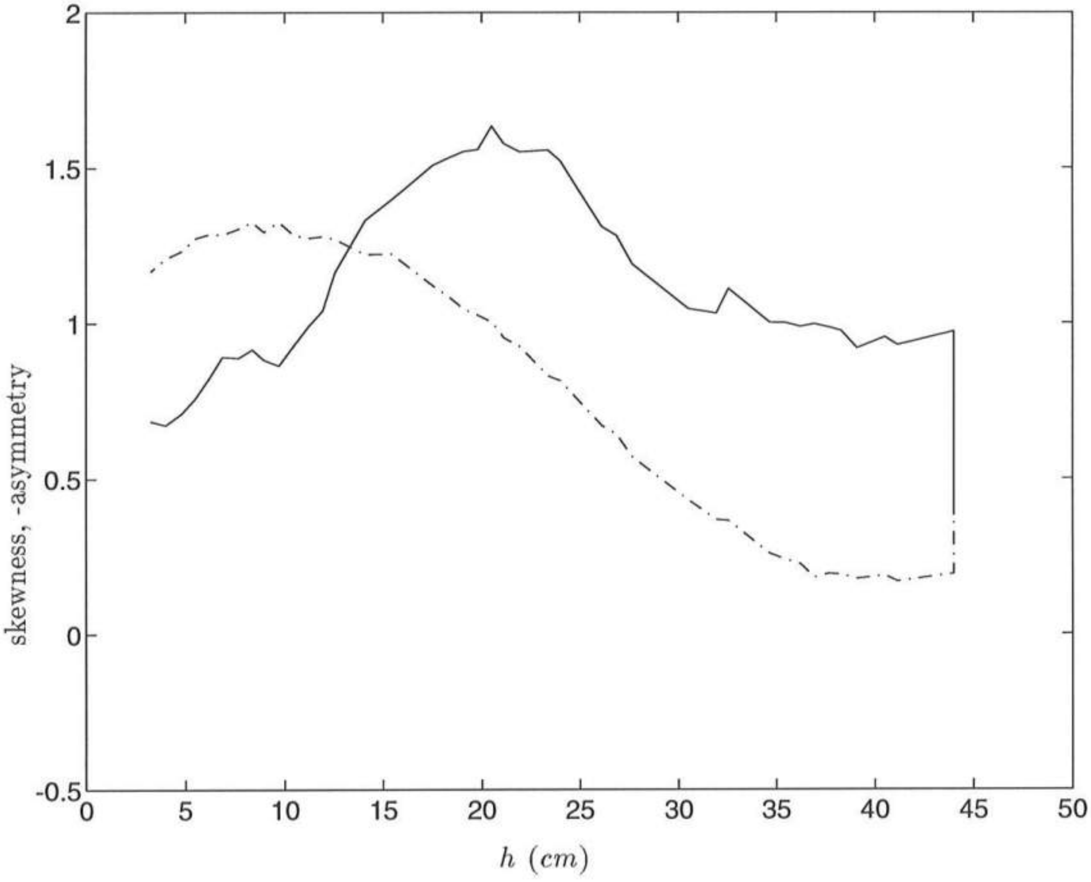

Figure 3.9: Shoreward evolution of skewness and asymmetry, 8 cm run; (——) skewness; (-·-·-) asymmetry

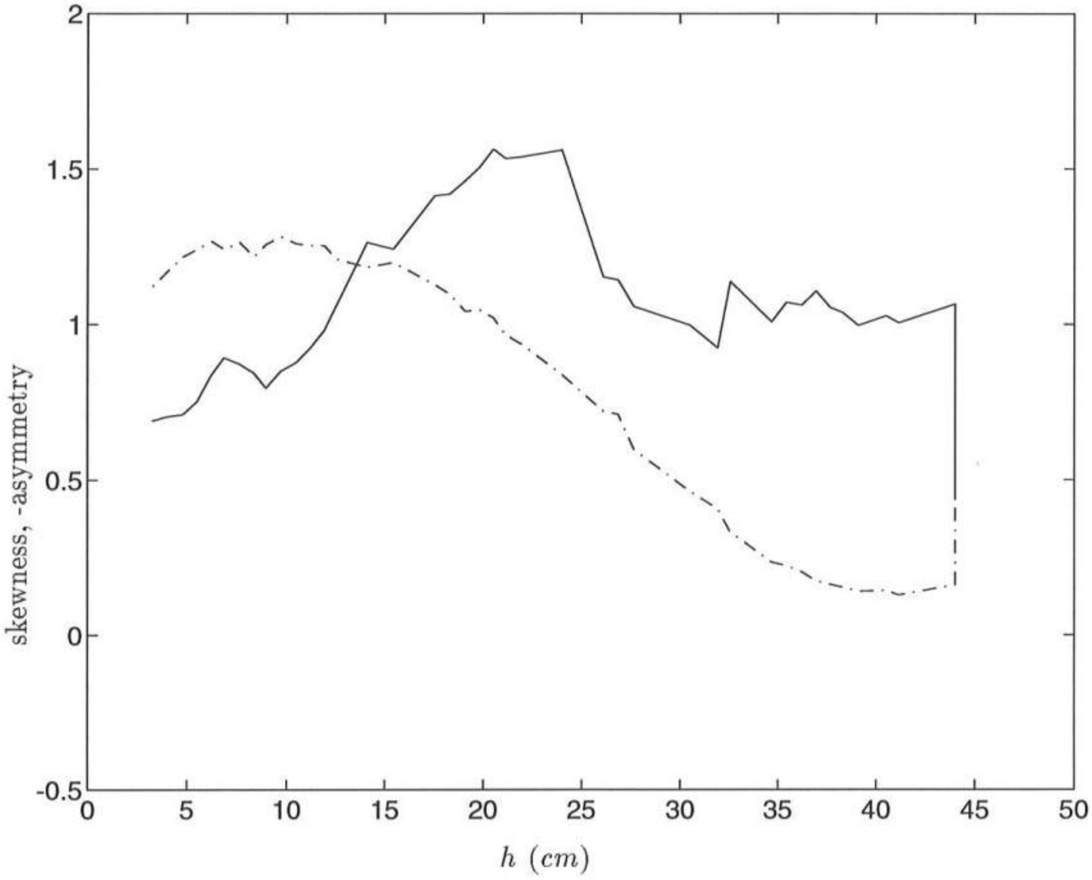

Figure 3.10: Shoreward evolution of skewness and asymmetry, 9 cm run; (——) skewness; (-·-·-) asymmetry

two free parameters in Equation 3.4, γ, the relation between H_{rms} and local depth in the inner surfzone, and B, the amount of foam on the face of the wave, were assigned values of .6 and 1 respectively for initial analysis, following the results of Mase and Kirby (1992). Through the shoaling region, agreement is best for the $7cm$ run (Figure 3.11); the model slightly overpredicts values for the $8cm$ and $9cm$ runs. Adjusting the value of B to 1.15 (γ remains at .6) produces closer agreement between the model and the measured data (Figures 3.14 and 3.15). This increase in B to produce better agreement is most likely due to the waves in these experiments being relatively larger than those in Mase and Kirby (1992), and thus having a greater degree of foam on the front face. In all cases the model overpredicts the dissipation in the inner surfzone, resulting in calculated values up to 50 percent lower than those measured. This is due in part to the model not considering wave setup in the surfzone, as wave setup was not removed from the laboratory data.

The model predicts virtually the same value in the inner surfzone for all cases, as it assumes a limiting height when the wave trains become saturated. Thus, the larger waves in the shoaling region must lose more energy to turbulence. Dissipation is tied to the value of H_{rms}/h, plots of which are shown in Figures 3.16 through 3.18. Figures 3.19 and 3.20 show the model predictions with B adjusted to 1.15.

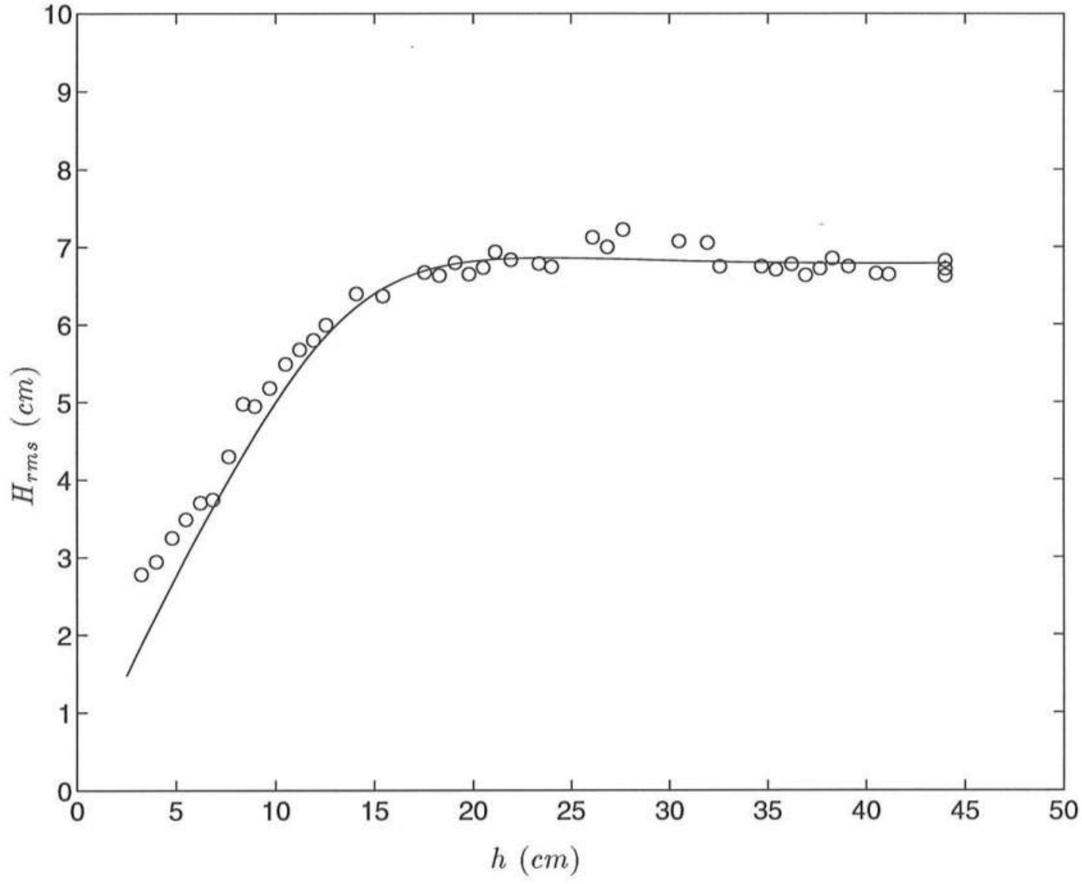

Figure 3.11: Shoreward evolution of H_{rms}, 7 *cm* run; (ooooo) measured data; (—) energy flux balance solution (Thornton and Guza, 1983)

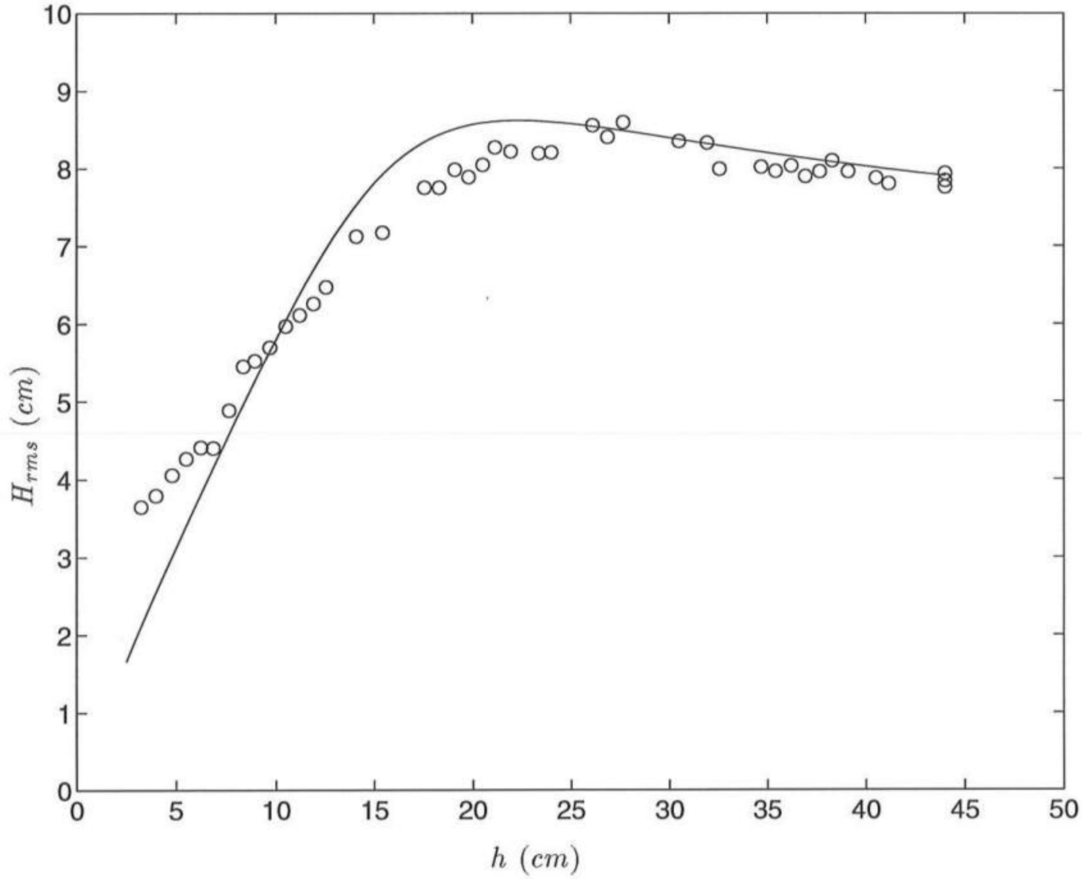

Figure 3.12: Shoreward evolution of H_{rms}, 8 *cm* run; (ooooo) measured data; (—) energy flux balance solution (Thornton and Guza, 1983)

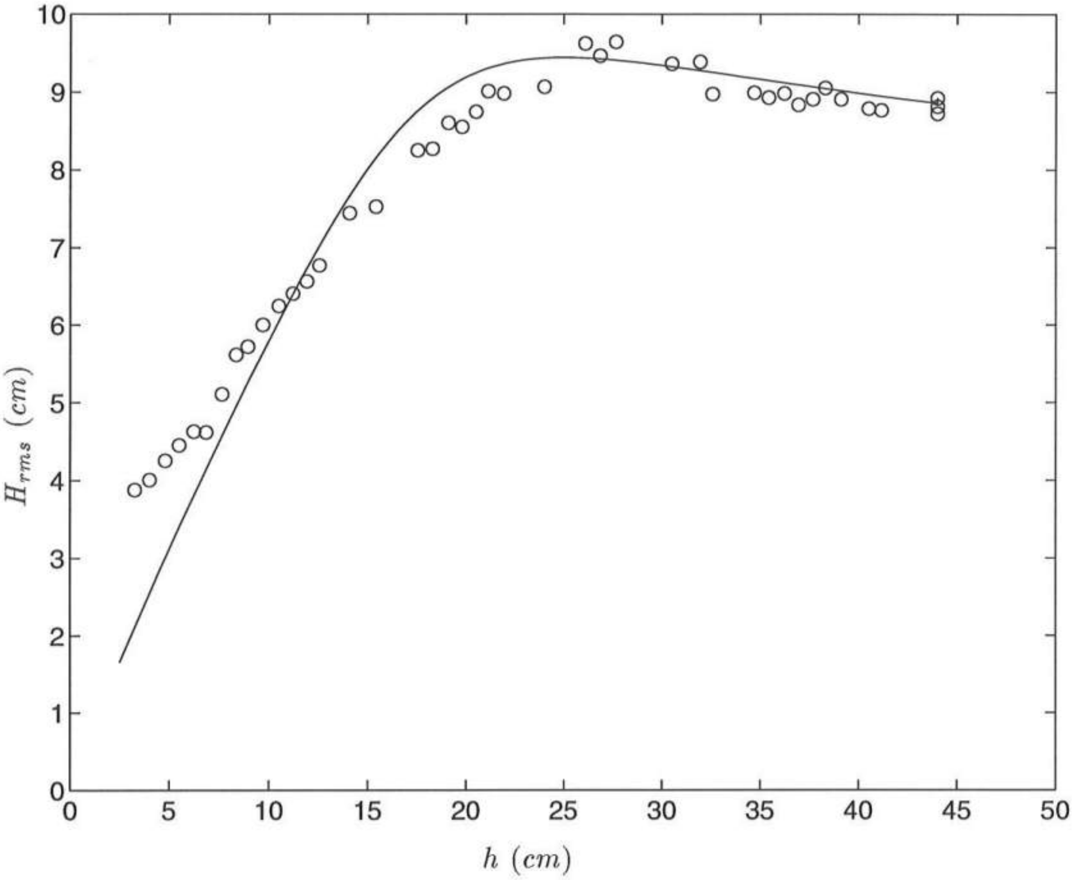

Figure 3.13: Shoreward evolution of H_{rms}, 9 *cm* run; (ooooo) measured data; (—) energy flux balance solution (Thornton and Guza, 1983)

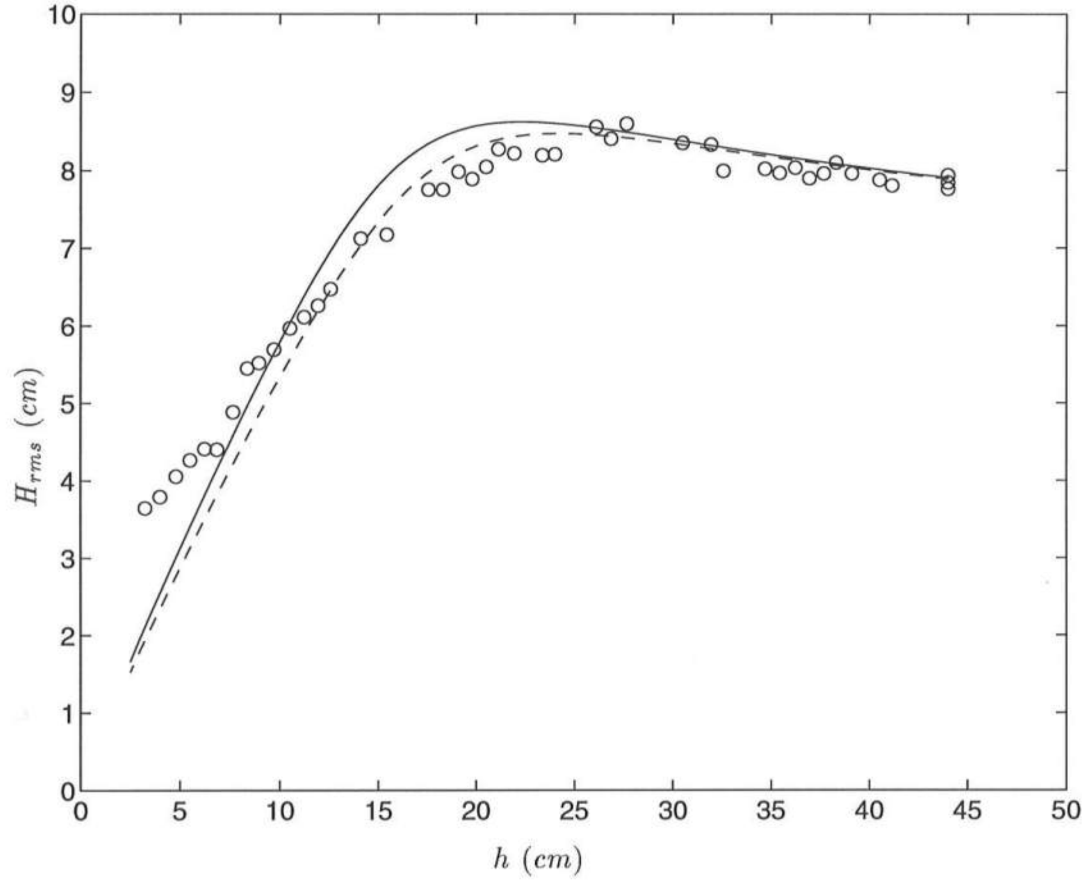

Figure 3.14: Shoreward evolution of H_{rms}, 8 *cm* run; (ooooo) measured data; (- - -) energy flux balance solution with B=1.15 (Thornton and Guza, 1983); (—) B=1

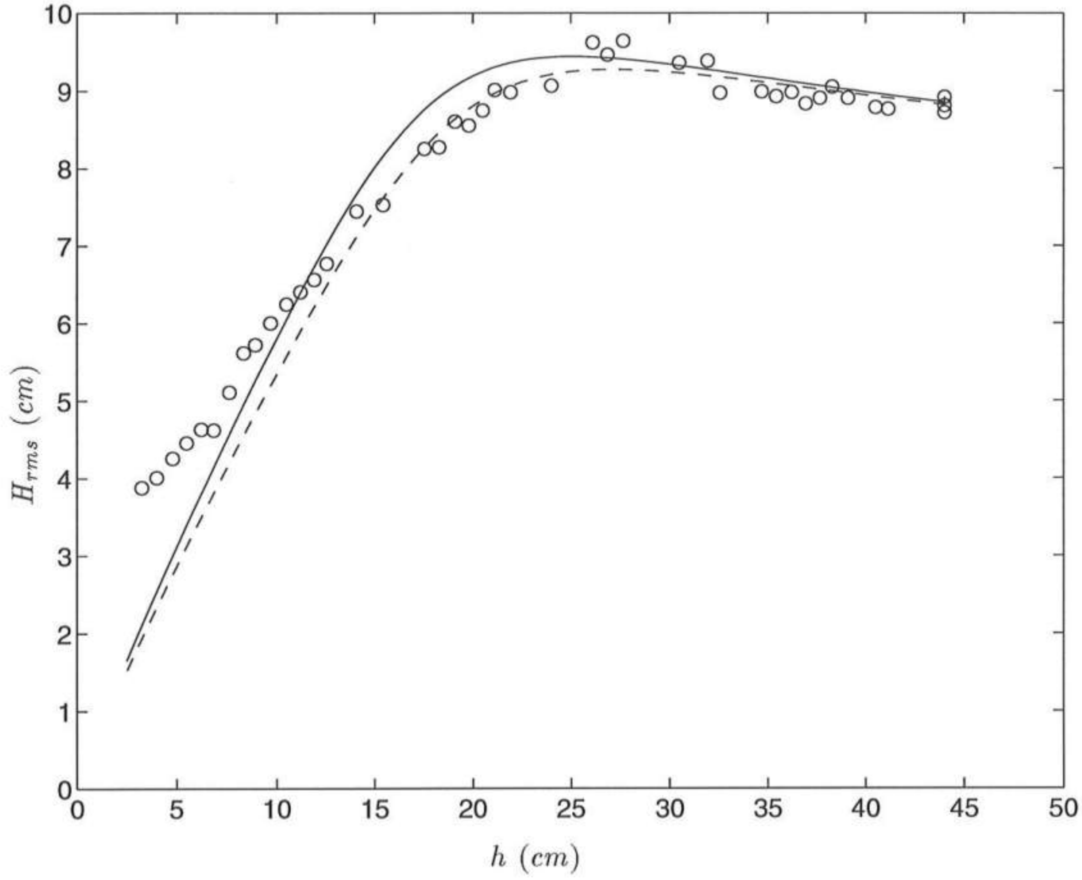

Figure 3.15: Shoreward evolution of H_{rms}, 9 *cm* run; (ooooo) measured data; (- - -) energy flux balance solution with B=1.15 (Thornton and Guza, 1983); (—) B=1

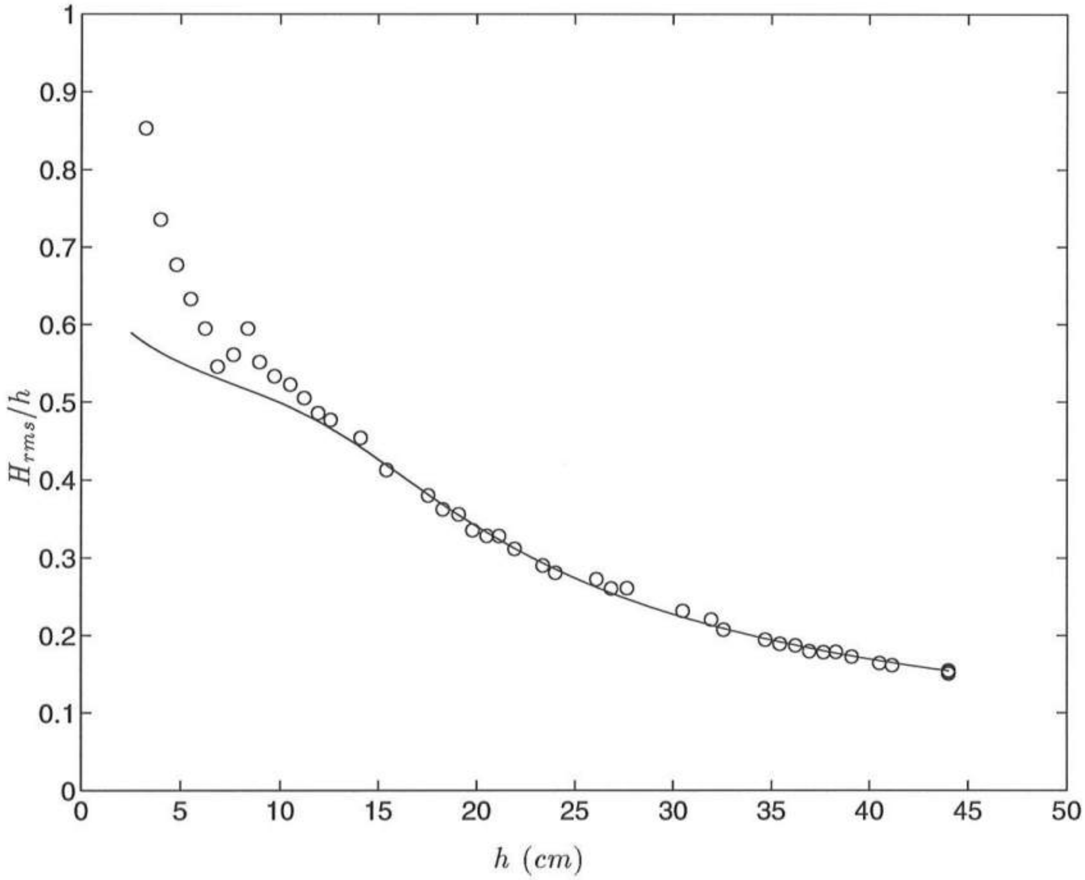

Figure 3.16: Shoreward evolution of H_{rms}/h, 7 cm run; (ooooo) measured data; (—) energy flux balance solution (Thornton and Guza, 1983)

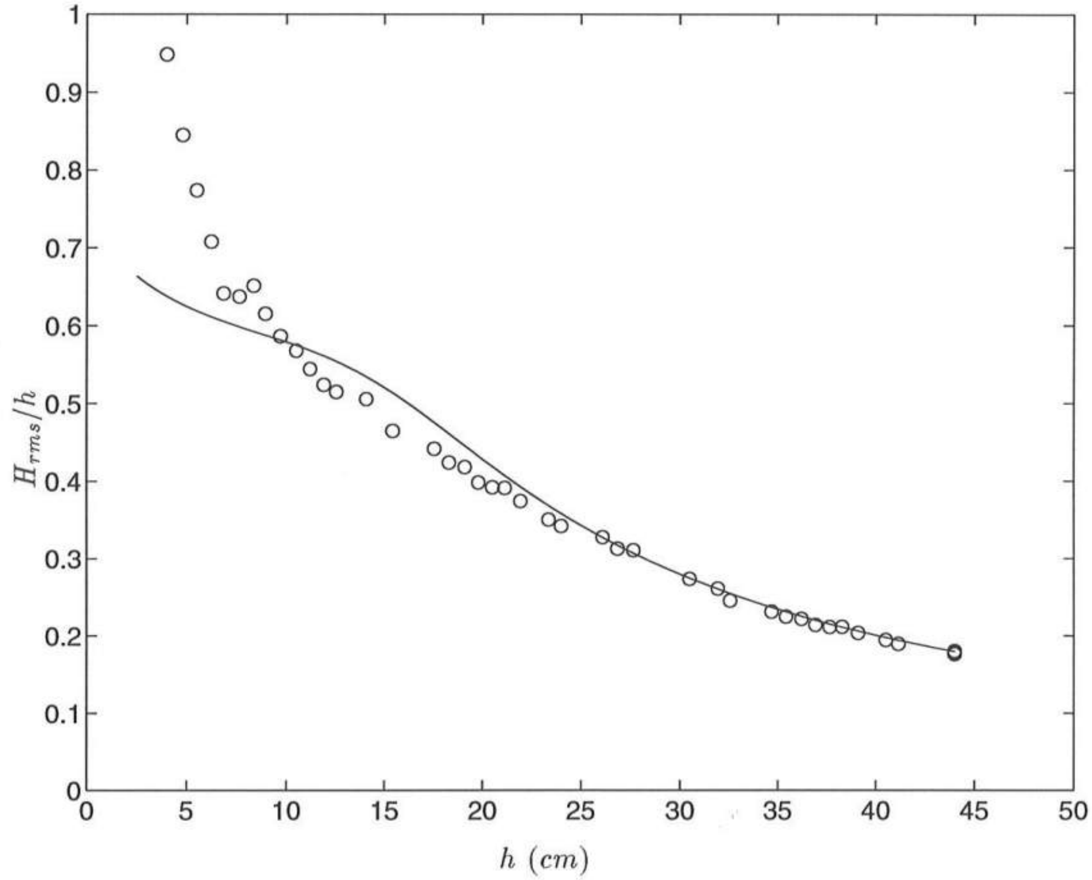

Figure 3.17: Shoreward evolution of H_{rms}/h, 8 *cm* run; (ooooo) measured data; (—) energy flux balance solution (Thornton and Guza, 1983)

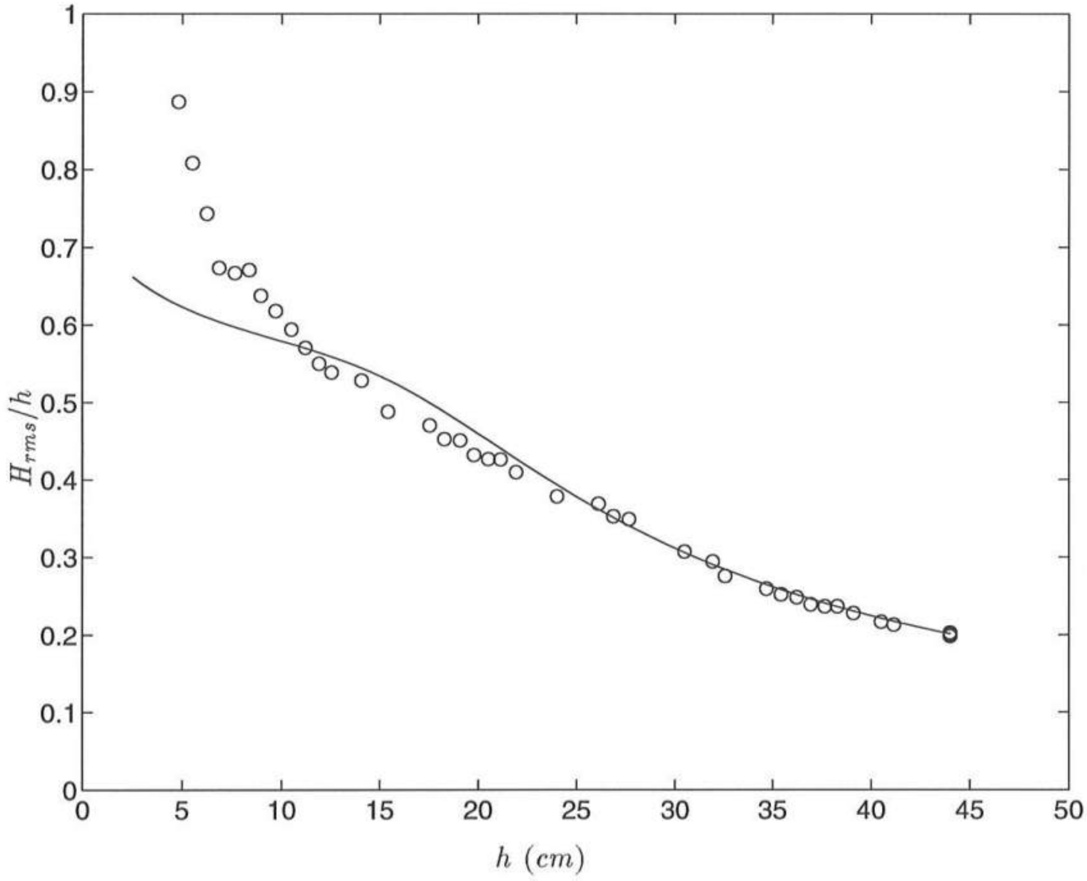

Figure 3.18: Shoreward evolution of H_{rms}/h, 9 *cm* run; (ooooo) measured data; (—) energy flux balance solution (Thornton and Guza, 1983)

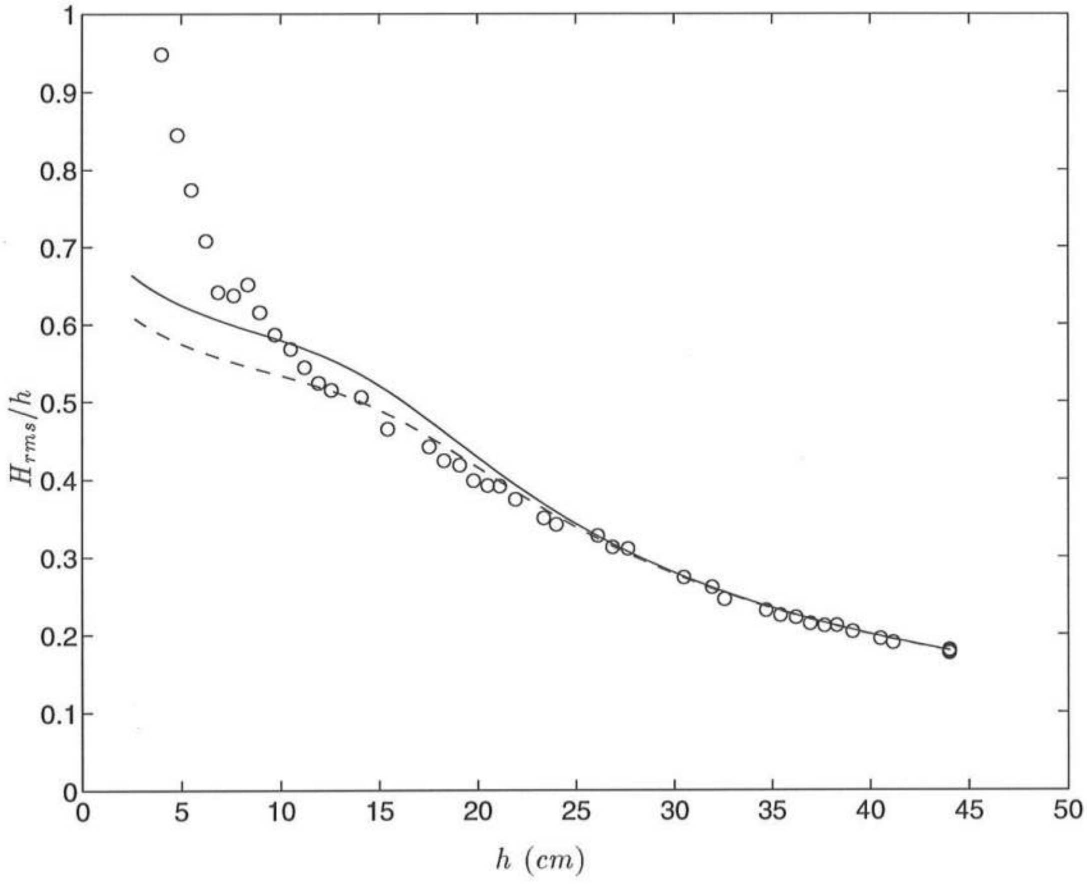

Figure 3.19: Shoreward evolution of H_{rms}/h, 8 *cm* run; (ooooo) measured data; (- - -) energy flux balance solution with B=1.15 (Thornton and Guza, 1983); (—) B=1

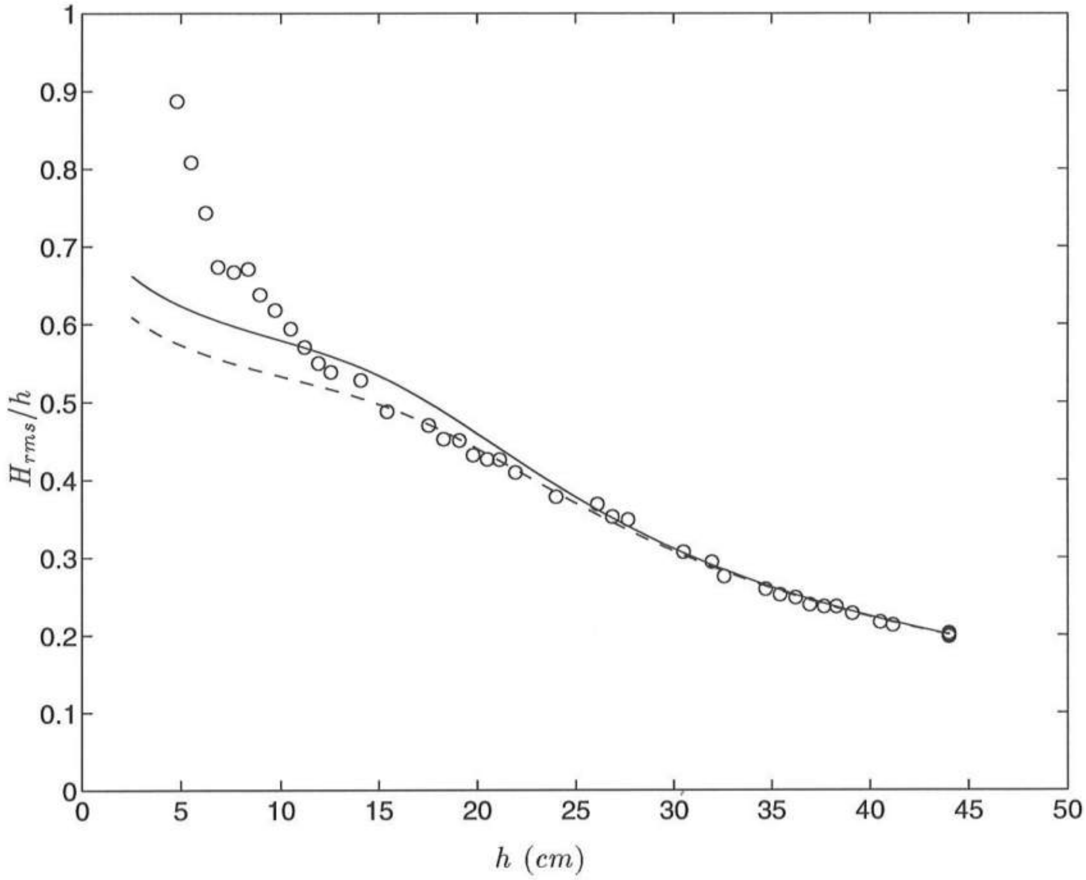

Figure 3.20: Shoreward evolution of H_{rms}/h, 9 *cm* run; (ooooo) measured data; (- - -) energy flux balance solution with B=1.15 (Thornton and Guza, 1983); (—) B=1

Chapter 4

Data Comparisons

4.1 Seiching

When laboratory experiments are conducted in a one-dimensional closed tank, there is no longshore dependence. Thus, edge waves that may be present during field experiments, and their contribution to the low end of the spectrum, are absent. However, the present data shows that energy in the very low frequency modes increases as one moves shoreward (Section 3.2.1). For this reason, the very low frequency portions of the measured spectra were analyzed to determine if the energy present corresponded to the flume's seiching modes.

4.1.1 Governing Equation

To calculate the seiching modes of the flume, the linearized continuity equation

$$\frac{\partial (Uh)}{\partial x} = -\frac{\partial \eta}{\partial t} \tag{4.1}$$

and the linearized frictionless long wave equation of motion

$$\frac{\partial U}{\partial t} = -g\frac{\partial \eta}{\partial x} \tag{4.2}$$

are cross differentiated to yield the governing equation

$$\frac{\partial^2 \eta}{\partial t^2} - \frac{\partial}{\partial x}\left(gh(x)\frac{\partial \eta}{\partial x}\right) = 0. \tag{4.3}$$

The flume is then divided into two regions, the flat bottom and the slope. The profile equations from Wilson (1966) for the two geometries are

$$h(x) = h_o \tag{4.4}$$

Table 4.1: Seiching modes in the precision wave flume

ω (rad/s)	f (Hz)	T (s)
0.1934	0.0308	32.47
0.3477	0.0553	18.08
0.4994	0.0795	12.58
0.6545	0.1042	9.60
0.8105	0.1290	7.75
0.9642	0.1534	6.52

for the flat bottom (rectangular) region, and

$$h(x) = \frac{h_1 x}{L} \tag{4.5}$$

for the sloping (triangular) region. Equation 4.5 is rewritten as

$$h(x) = \frac{h_o(L-x)}{L-x_o} \tag{4.6}$$

where L in Equation 4.6 is the sum of the lengths of both regions and x_o is the value of x at the toe of the slope. Solving the governing equation for each region and matching the solutions at the toe of the slope yields

$$\tan\left(\frac{\omega x_o}{\sqrt{gh_o}}\right) + \frac{J_1\left(\frac{2\omega(L-x_o)}{\sqrt{gh_o}}\right)}{J_0\left(\frac{2\omega(L-x_o)}{\sqrt{gh_o}}\right)} = 0. \tag{4.7}$$

A full derivation is found in Veeramony (1994b). As Figure 2.6 shows, h_o=0.44 m, x_o=11.5 m, and L=26.9 m for the present data set. Values of ω which satisfy Equation 4.7 are the seiching frequencies as measured in rad/s. Dividing ω by 2π results in the seiching frequencies expressed in Hz. Table 4.1 lists the zeroes of Equation 4.7 in rad/s and Hz, and the seiching periods. Figure 4.1 shows the value of the L.H.S. of Equation 4.7 *vs.* ω, generated numerically with a model provided by Veeramony (1994a).

4.1.2 Data Comparison

The very low frequency amplitudes of the measured data were examined at h=.44 m, where they have their lowest values, and at h=.04 m where they have their highest values.

Figure 4.2 shows the very low frequency amplitudes of the measured spectrum with 8 degrees of freedom (computed from 4 segments of 4096 points) for the 7 cm run at h=.44 m, plotted *vs.* the flume's seiching modes. Examining the area of the first three seiching modes, the 95 percent confidence intervals plotted do not confirm that the variation seen in the spectrum may be attributed to statistically significant seiching. In order to tighten the 95 percent confidence intervals while using the same amount of data and not losing the spectral resolution that separates the peaks, the spectrum was recomputed from 7 segments of 4096 points, with a 50 percent overlap, to achieve 14 degrees of freedom. Figure 4.3 shows the very low frequency amplitudes of this spectrum at h=.44 *m* plotted *vs.* the flume's seiching modes. Figures 4.4 and 4.5 show the same comparison for the 8 *cm* and 9 *cm* runs, respectively. Figures 4.6 through 4.8 show the same comparison for each run, with h=.04 *m*. To determine the amount of the increase in energy between the spectra at h=0.44 *m* and the spectra at h=0.04 *m* that is attributable to seiching, the spectra at h=0.44 *m* for the 7 *cm*, 8 *cm*, and 9 *cm* runs were shoaled to h=0.04 *m* according to Green's Law

$$\frac{a}{a_o} = \left(\frac{h}{h_o}\right)^{-1/4} \tag{4.8}$$

or in this case

$$\frac{S}{S_o} = \left(\frac{h}{h_o}\right)^{-1/2} \tag{4.9}$$

and plotted *vs.* the spectra at h=0.04 *m* in Figures 4.9, 4.10, and 4.11. These plots reveal that statistically significant seiching is occuring, as may be expected in a closed tank, and that a simple standing wave analysis accounts for most of the low frequency variance in the tank. It is thus not evident that much of the low frequency motion is directly forced surf beat energy.

4.2 Wood *vs.* Sand Beach Comparison

An important concern in laboratory experimentation, especially when a rigid beach is employed, is correctly reproducing the energy in the low frequency portion of the spectrum. As a basis for comparison for the flume data, the following two subsections present results of the measured data *vs.* those of a larger scale laboratory experiment with a sand beach, and a full scale field experiment.

4.2.1 SUPERTANK

Experimental Parameters

The SUPERTANK Laboratory Data Collection Project took place from July 29 to September 20, 1991 in the large wave tank at the O.H. Hinsdale Wave Research Laboratory at Oregon State University. The multi-institutional project was overseen by U.S. Army Corps of Engineers (USACE) Coastal Engineering Research Center (CERC) personnel. The physical dimensions of the large wave tank are: 104 meters long, 4.6 meters deep, and 3.7 meters wide. As the large wave tank is roughly 3.5 times longer and 6 times deeper and wider than the precision wave flume, scaling effects are expected to be much less significant.

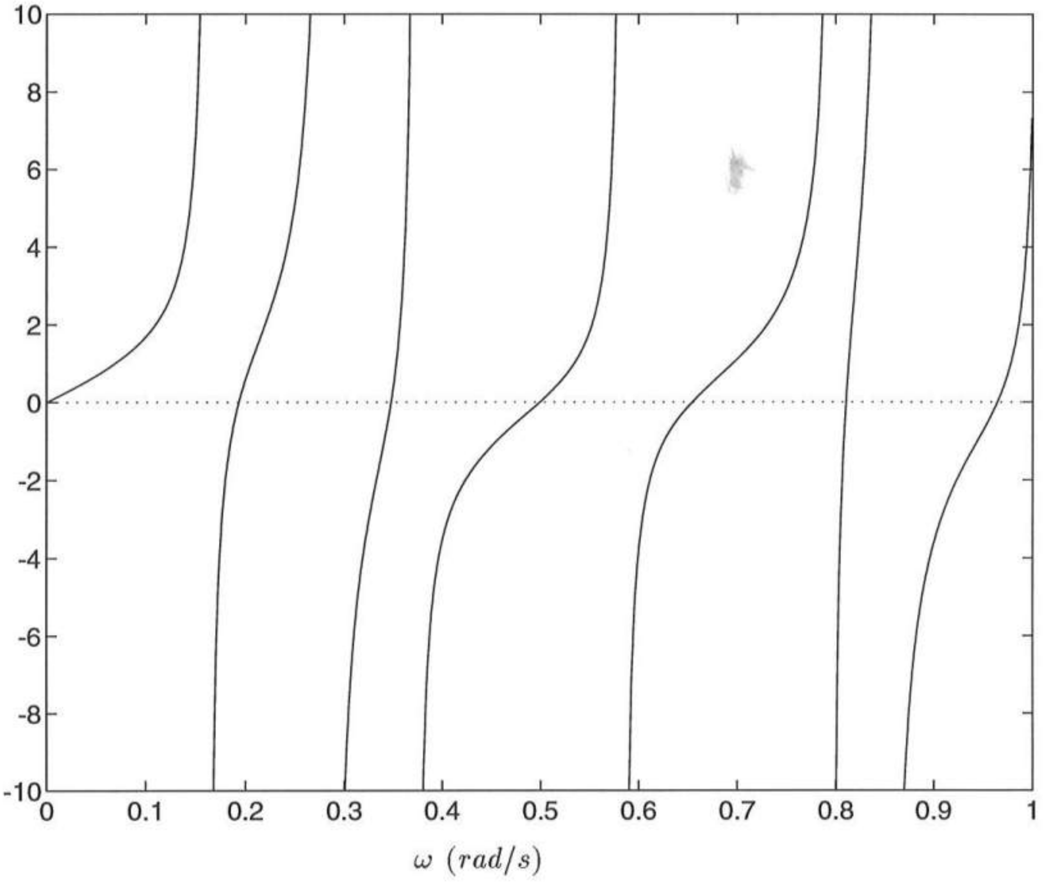

Figure 4.1: L.H.S. of Equation 4.7, (curve crosses zero line at the seiching frequencies of the precision wave flume with h_o=0.44 m, x_o=11.5 m, and L=26.9 m)

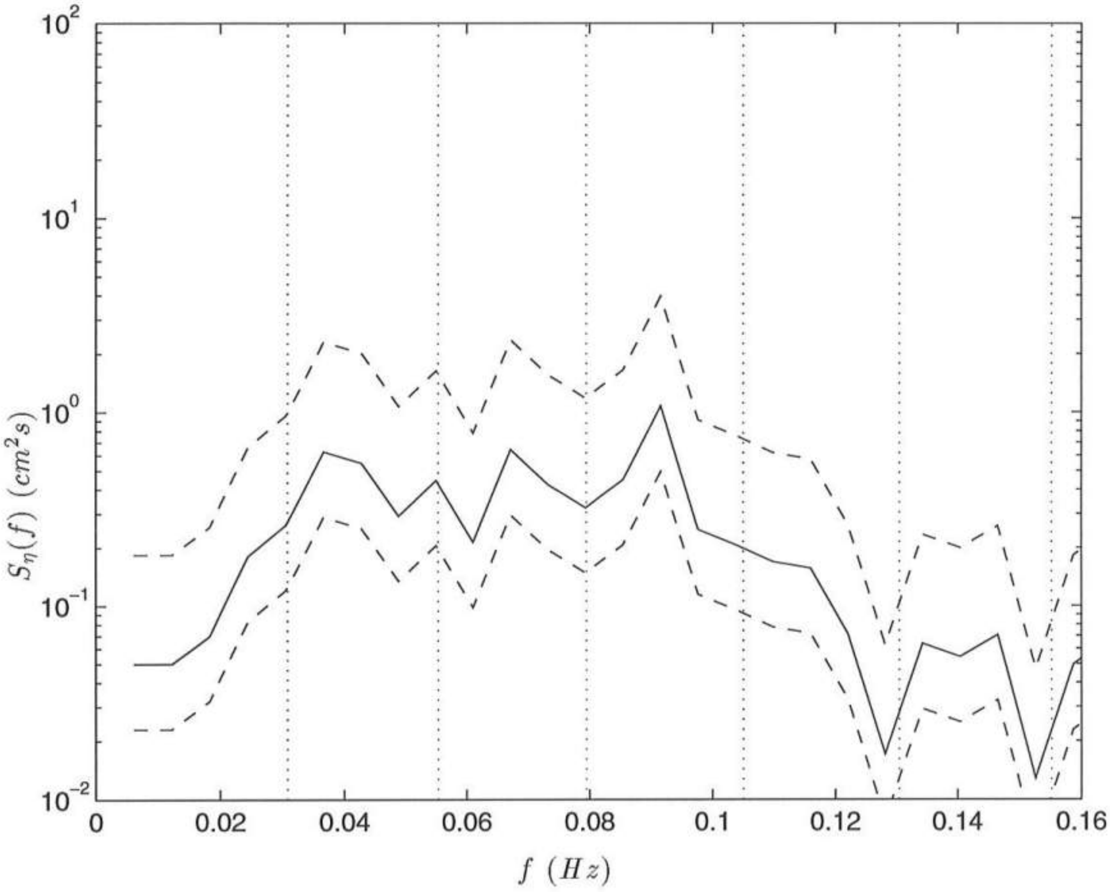

Figure 4.2: Low frequency portion of energy spectrum, 7 *cm* run, 8 DOF; (—) energy spectrum, x=3.0 m, *h*=0.44 m; (- - -) 95% confidence interval limits; (· · · · ·) seiching frequencies

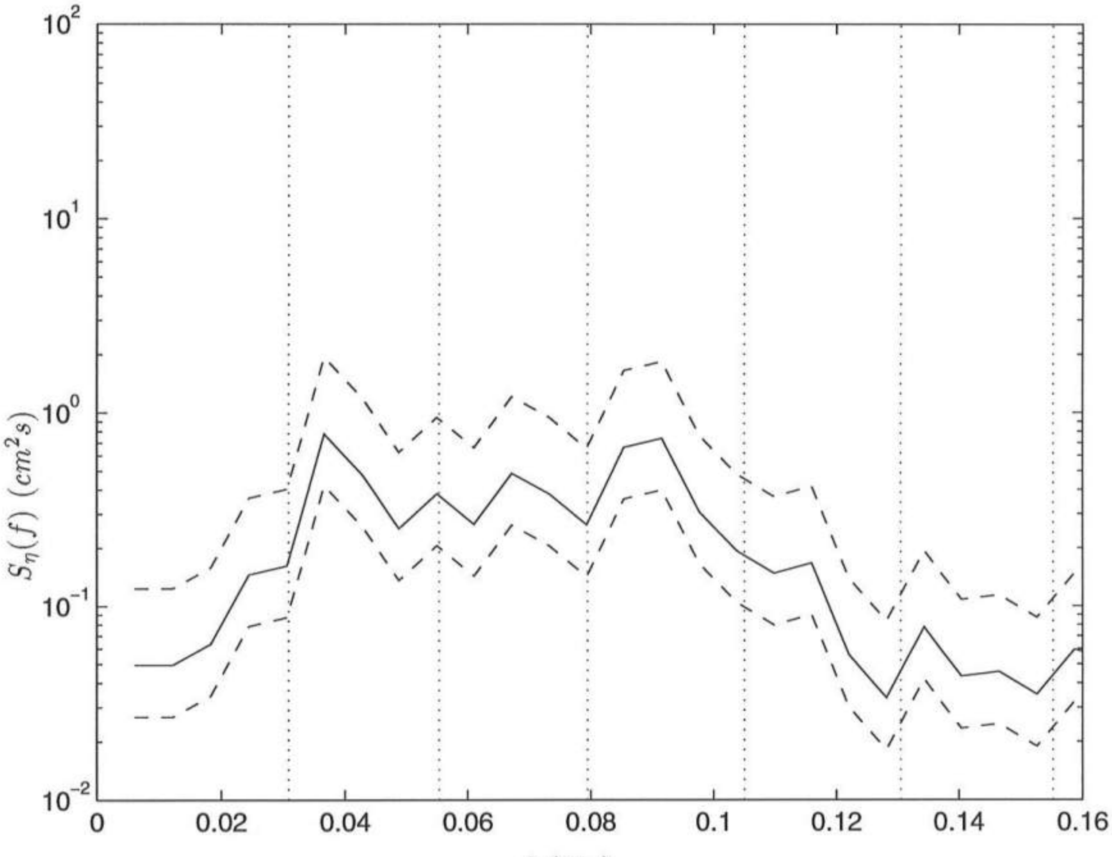

Figure 4.3: Low frequency portion of energy spectrum, 7 *cm* run, 14 DOF; (—) energy spectrum, x=3.0 m, h=0.44 m; (- - -) 95% confidence interval limits; (· · · · ·) seiching frequencies

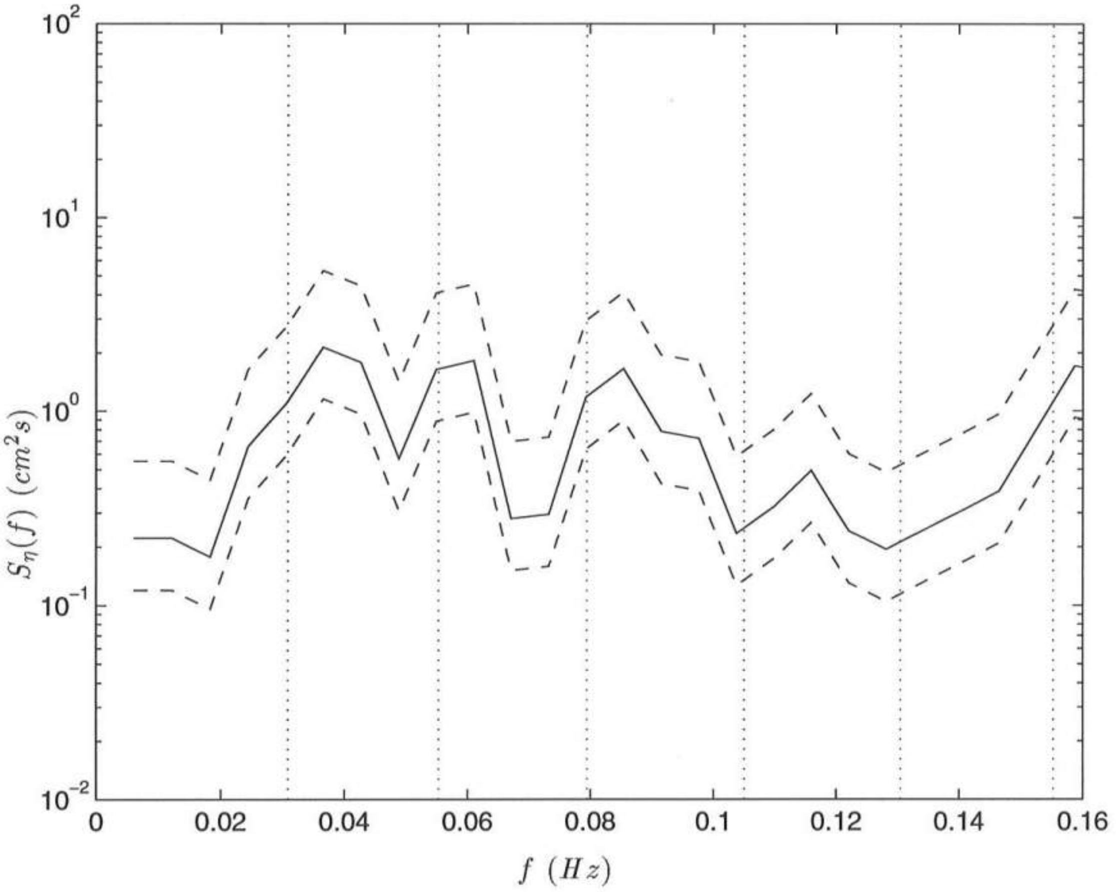

Figure 4.4: Low frequency portion of energy spectrum, 8 *cm* run, 14 DOF; (—) energy spectrum, x=3.0 m, *h*=0.44 m; (- - -) 95% confidence interval limits; (· · · · ·) seiching frequencies

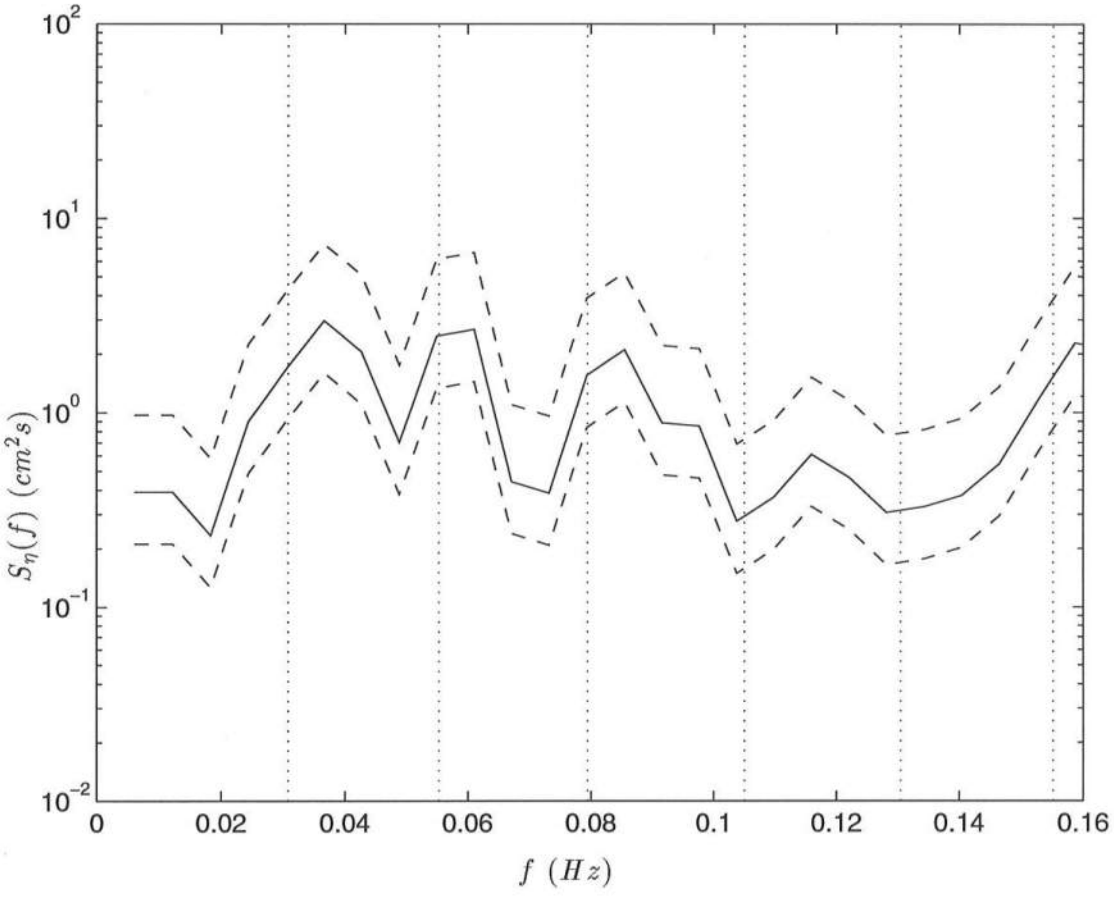

Figure 4.5: Low frequency portion of energy spectrum, 9 *cm* run, 14 DOF; (—) energy spectrum, x=3.0 m, h=0.44 m; (- - -) 95% confidence interval limits; (· · · · ·) seiching frequencies

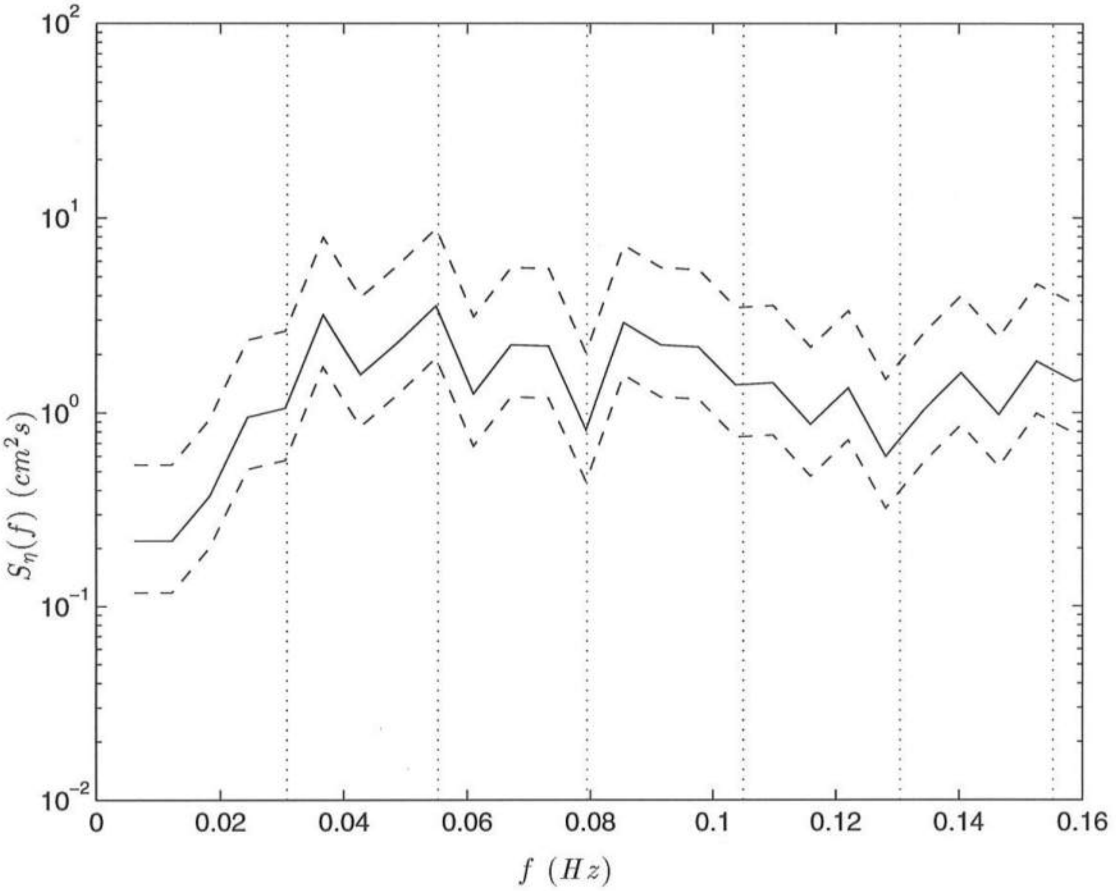

Figure 4.6: Low frequency portion of energy spectrum, 7 *cm* run, 14 DOF; (——) energy spectrum, x=25.5 m, *h*=0.04 m; (- - -) 95% confidence interval limits; (· · · · ·) seiching frequencies

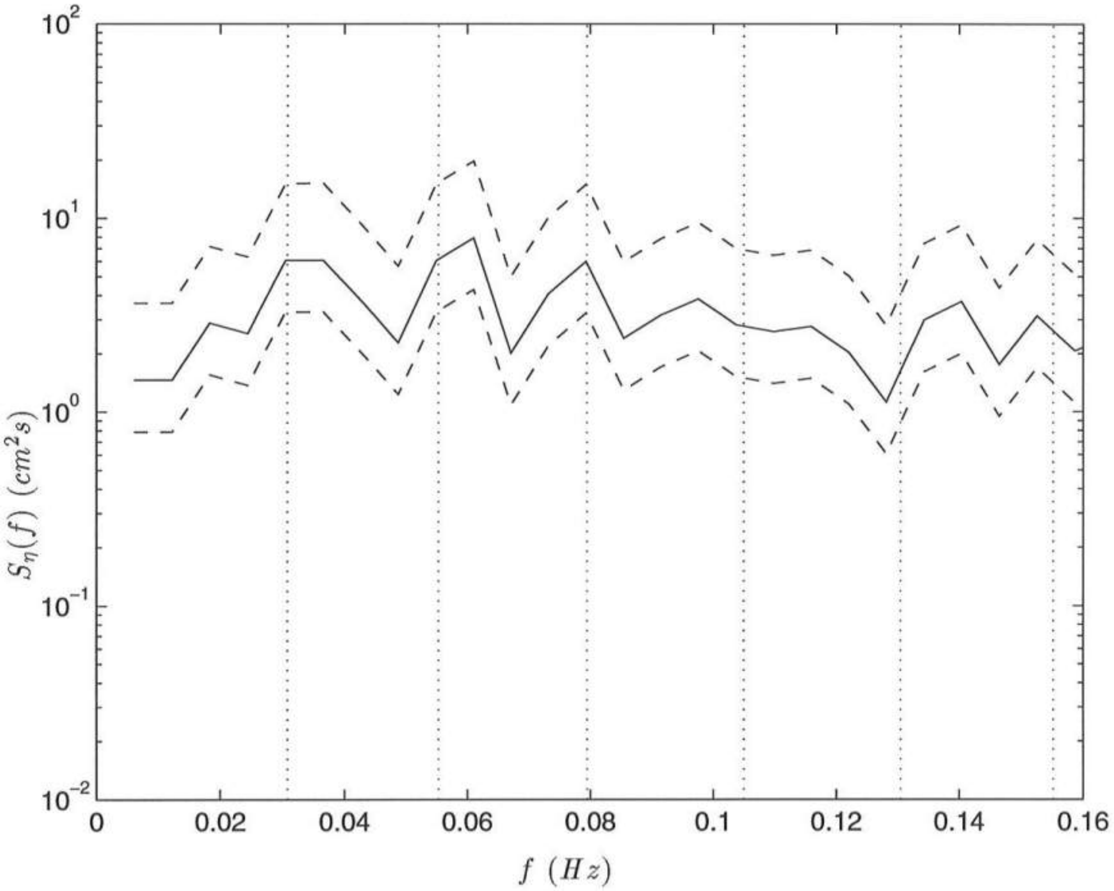

Figure 4.7: Low frequency portion of energy spectrum, 8 *cm* run, 14 DOF; (—) energy spectrum, x=25.5 m, h=0.04 m; (- - -) 95% confidence interval limits; (· · · · ·) seiching frequencies

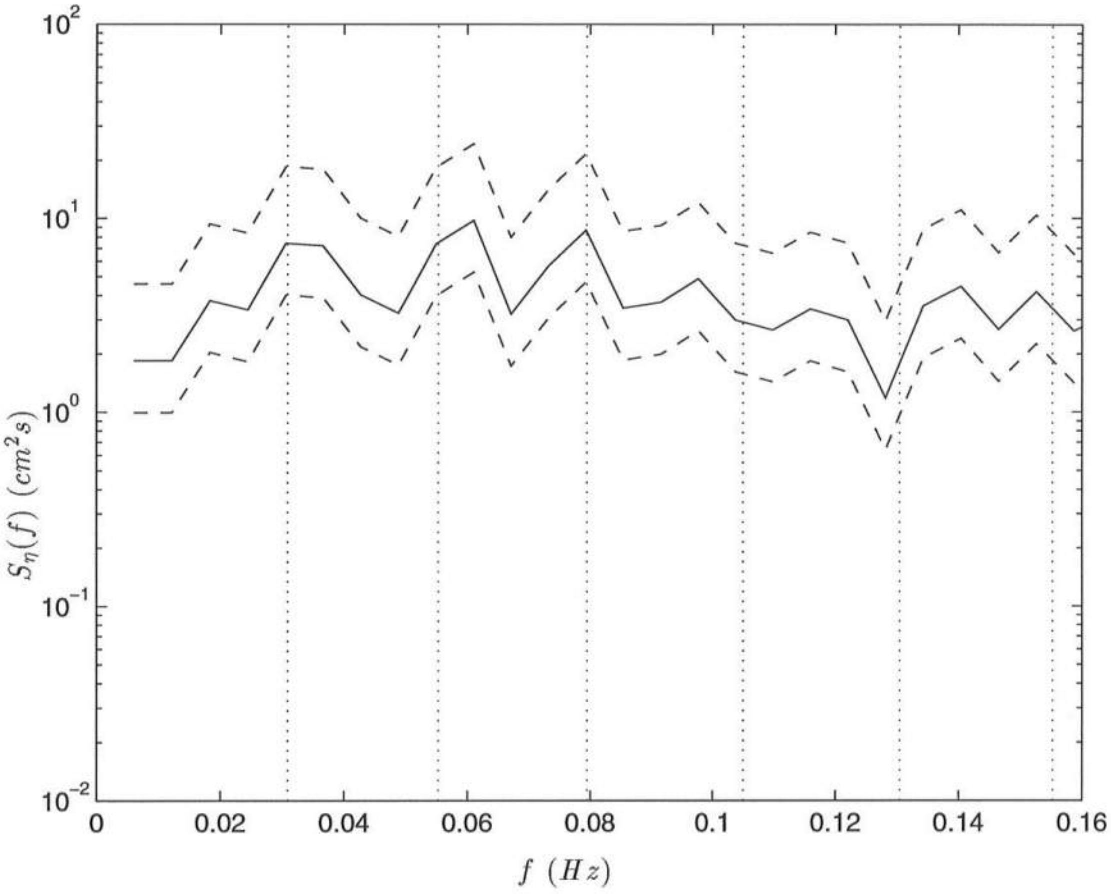

Figure 4.8: Low frequency portion of energy spectrum, 9 *cm* run, 14 DOF; (—) energy spectrum, x=25.5 m, h=0.04 m; (- - -) 95% confidence interval limits; (· · · · ·) seiching frequencies

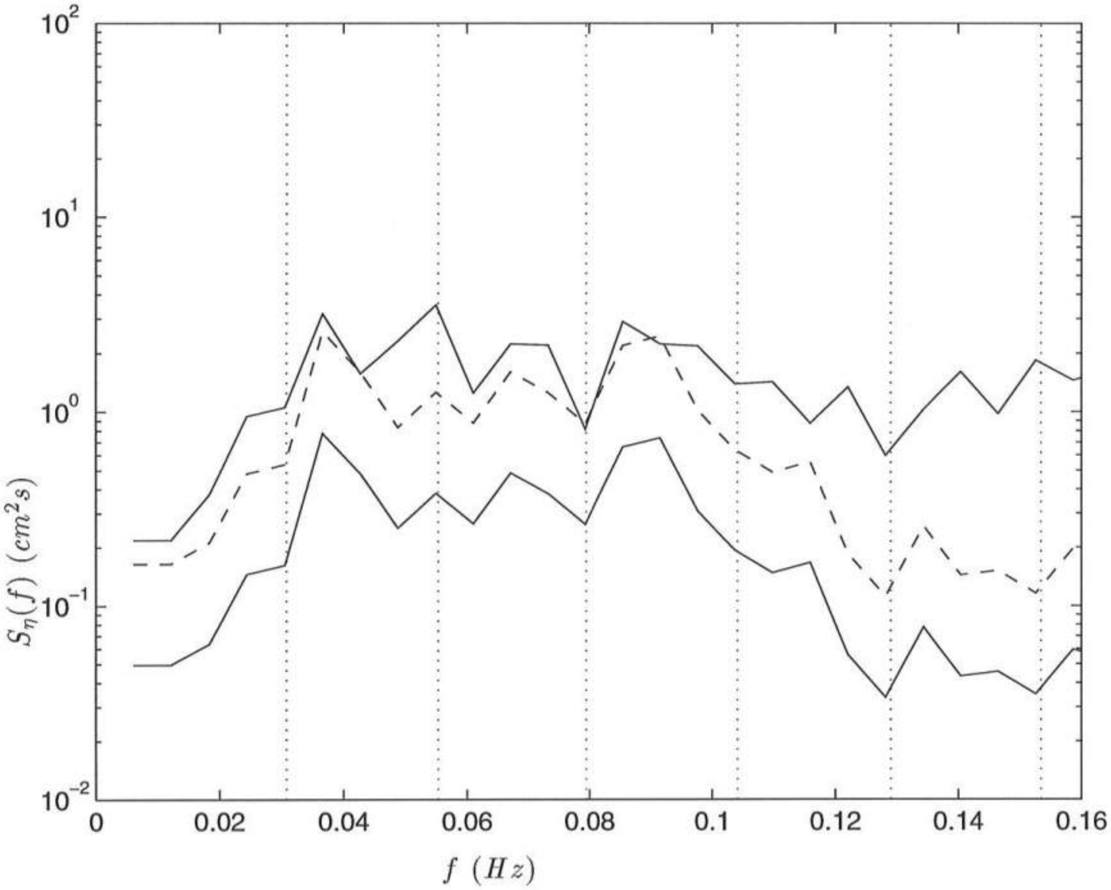

Figure 4.9: Low frequency portion of energy spectrum, 7 *cm* run, 14 DOF; from bottom to top: (—) energy spectrum, x=3.0 m, h=0.44 m; (- - -) energy spectrum, x=3.0 m, h=0.44 m, shoaled to h=0.04 m by Green's Law; (—) energy spectrum, x=25.5 m, h=0.04m

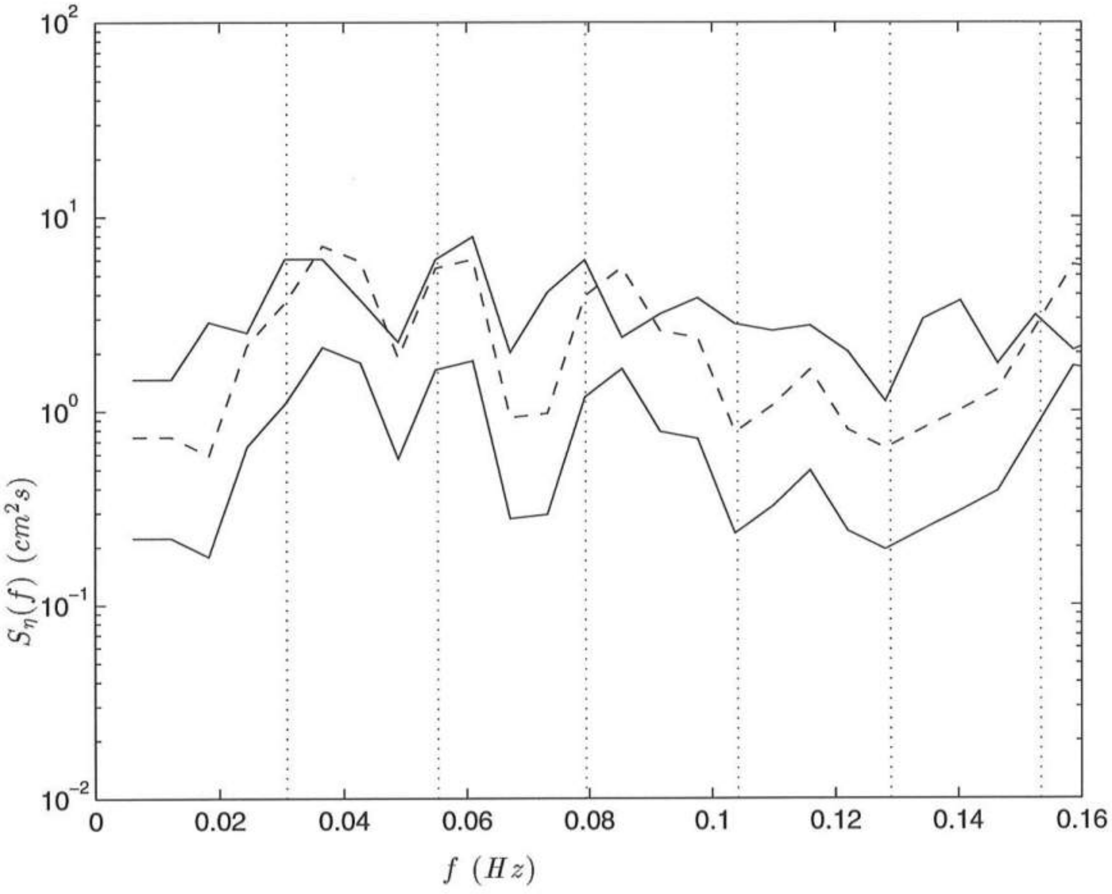

Figure 4.10: Low frequency portion of energy spectrum, 8 *cm* run, 14 DOF; from bottom to top: (—) energy spectrum, x=3.0 m, h=0.44 m; (- - -) energy spectrum, x=3.0 m, h=0.44 m, shoaled to h=0.04 m by Green's Law; (—) energy spectrum, x=25.5 m, h=0.04m

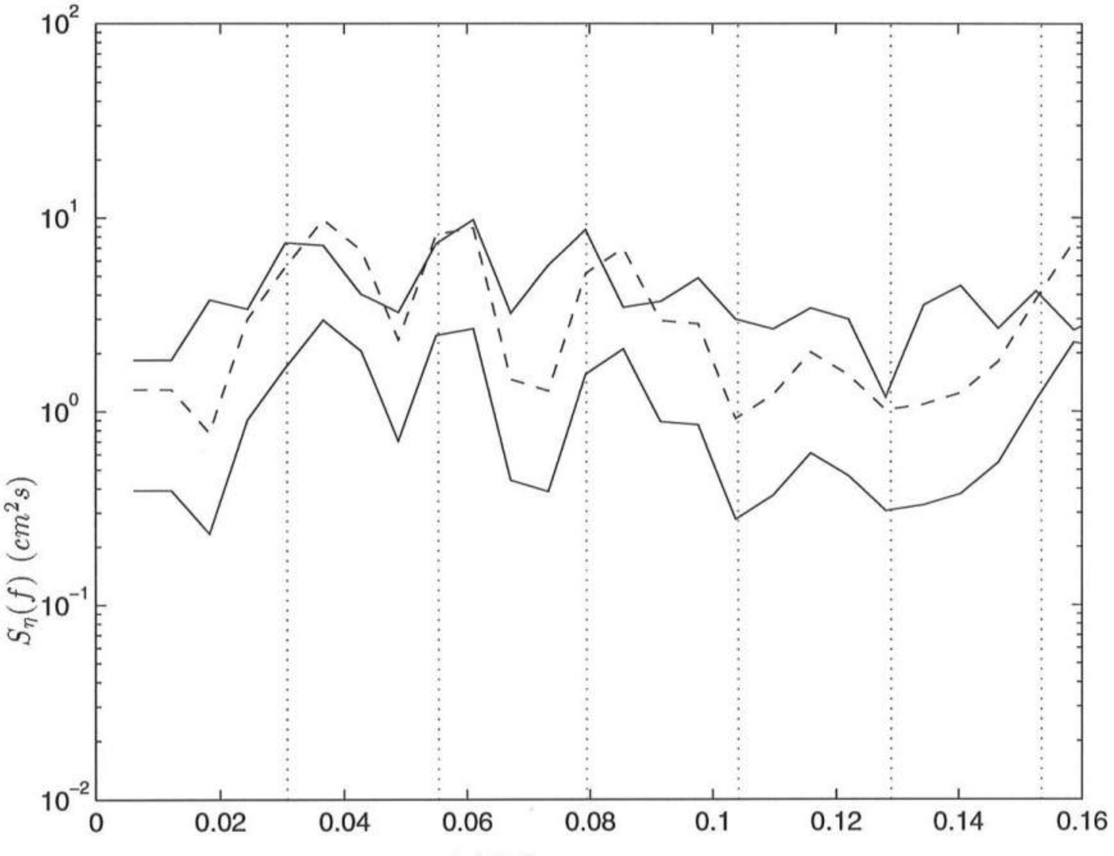

Figure 4.11: Low frequency portion of energy spectrum, 9 *cm* run, 14 DOF; from bottom to top: (—) energy spectrum, x=3.0 m, h=0.44 m; (- - -) energy spectrum, x=3.0 m, h=0.44 m, shoaled to h=0.04 m by Green's Law; (—) energy spectrum, x=25.5 m, h=0.04m

Table 4.2: Cutoff frequencies and spectral wave steepnesses

run	cutoff frequency (Hz)	H_{m0_o}/L_o
7 *cm*	0.34	0.0178
8 *cm*	0.15	0.0043
9 *cm*	0.15	0.0048

A sand beach with an initial slope of 1:10 was used for the SUPERTANK experiments. The slope was observed to change during the experiments due to erosion of the sand. To measure water surface elevation, 16 resistance wave gages were placed in the region from the wavemaker to the mid-surfzone and 10 capacitance gages, of identical design to those used here, were placed in the region of the shoreline area and on the beach face. Gages located shoreward of the initial shoreline extended below the sand surface and measured the intermittent wave activity as well as the saturated sand elevation in the absence of wave activity. This type of measurement is not possible with a wooden laboratory beach.

Data Comparison

Our comparison is with the SUPERTANK swash zone measurement trials conducted by Kreibel (1994b). Kreibel's target wave spectrum was based on a significant wave height (H_{m0_o}) of 0.66 *m* and a peak spectral period (T_p) of 6 seconds, for a spectral wave steepness of H_{m0_o}/L_o=0.01. Kreibel used a value of 0.5 times the spectral peak frequency as a cutoff for low and high pass filtering. Cutoff values for the present data set were chosen by visual inspection of the spectra, and are in the range from 0.6 to 0.7 times the measured spectral peak frequency. Table 4.2 lists the cutoff frequencies as well as the spectral wave steepness values for the 7 *cm*, 8 *cm*, and 9 *cm* runs.

Figure 4.12 shows fair agreement between the normalized low frequency wave height of Kreibel's spectrum and that of the 8 *cm* and 9 *cm* runs. Figure 4.13 shows that the ratio of the significant wave heights in the the low and high portions of Kreibel's spectrum corresponds very closely to that of the 8 *cm*, and 9 *cm* runs. In SUPERTANK, data recorded by the gages on the beach face show that the low frequency component increases steadily to a peak value at the initial shoreline, then decreases, but dominates the high frequency as one moves landward (Kreibel, 1994b).

4.2.2 DELILAH

Experimental Parameters

The DELILAH experiment was conducted during October of 1990 at the USACE CERC Field Research Facility (FRF) in Duck, North Carolina. The multi-institutional project was overseen by USACE CERC personnel. DELILAH was designed to study nearshore processes, and was a subset of the SAMPSON experiment, which measured the interaction of low frequency wind waves with the bottom on the continental shelf.

The FRF maintains a long-term directional array in 8 meters in water. In addition, 9 current meters and pressure gages were placed in a cross shore line with depths ranging from 4.25 meters to 0.28 meters. Bottom contours were basically parallel to the shoreline.

Data Comparison

The seven DELILAH data sets presented here were recorded on October 12, 1990 when Hurricane Lilli was 500 kilometers southeast of the test site. "Large regular swell waves were arriving from a direction nearly perpendicular to the shore but with a slight southerly slant ... Wave measurements at the directional array confirm[ed] the presence of swell with an exceptionally narrow spread in frequency and direction" (Thompson and Briggs, 1993). The seven trials all have spectral wave steepnesses of roughly 0.01, comparable to the SUPERTANK swash zone measurement trials.

Kreibel (1994a) performed low and high pass filtering on this data, choosing a cutoff value of 0.5 times the spectral peak frequency. Figure 4.14 shows fair agreement between the normalized low frequency wave heights of the DELILAH data, and that of the 7 cm, 8 cm and 9 cm runs. It appears that the field data contains slightly more energy in the low frequency portion of the spectrum far offshore, but that this energy does not increase as rapidly as that of the laboratory data. When depths are normalized by H_{m0_o}, the shoremost DELILAH gage is in relatively shallower water than the shoremost laboratory gage, thus there are no corresponding laboratory measurements at this location; however, extrapolating the curves based on the laboratory data to this location shows good agreement between field and laboratory data. The same evolution of low frequency energy in the field data is seen in Figure 4.15, where the ratio of the significant wave heights of the low and high ends of the spectra are plotted. These data suggest the existence of a limiting factor for the proportion of spectral energy in the low frequency modes in the saturated inner surfzone, irregardless of offshore conditions.

4.3 Truncation of Spectra

When running numerical spectral shoaling and breaking models, one difficulty always encountered is ensuring the availability of computer time necessary to complete the vast

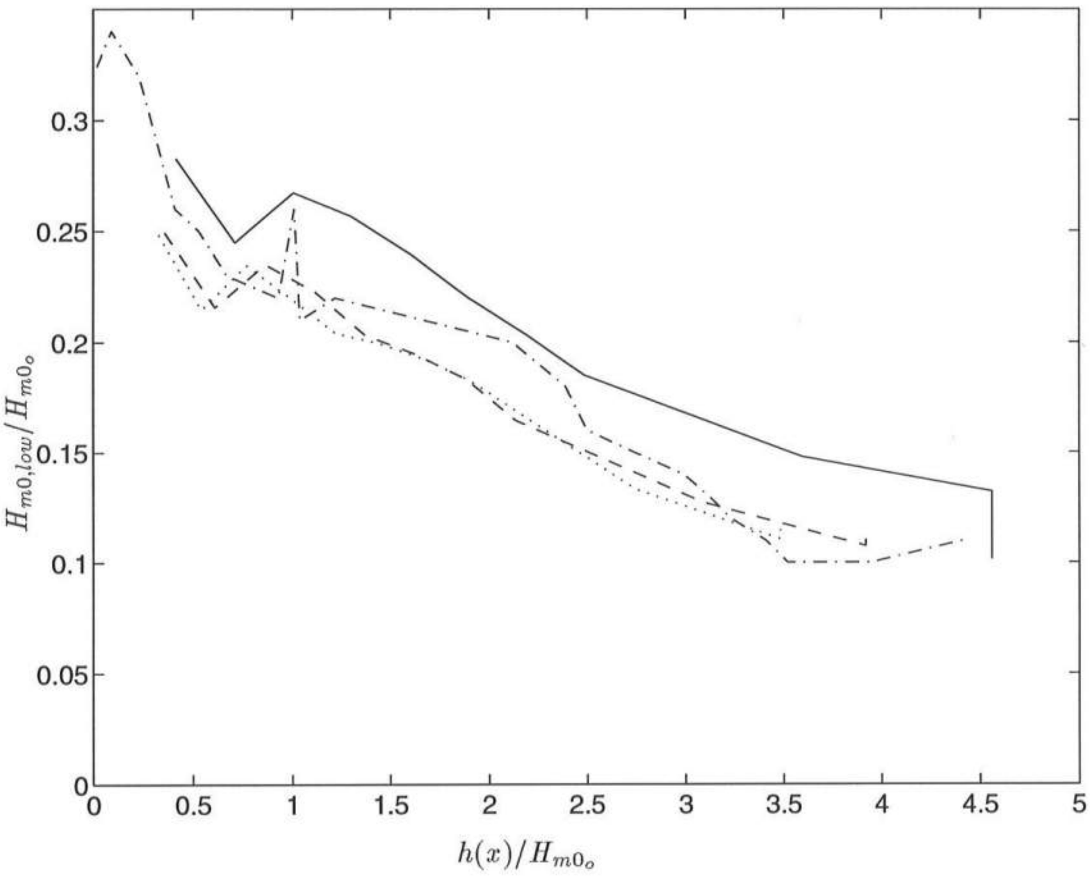

Figure 4.12: Normalized low frequency wave heights; (——) 7 *cm* run; (- - -) 8 *cm* run; (·····) 9 *cm* run; (-·-·-) SUPERTANK

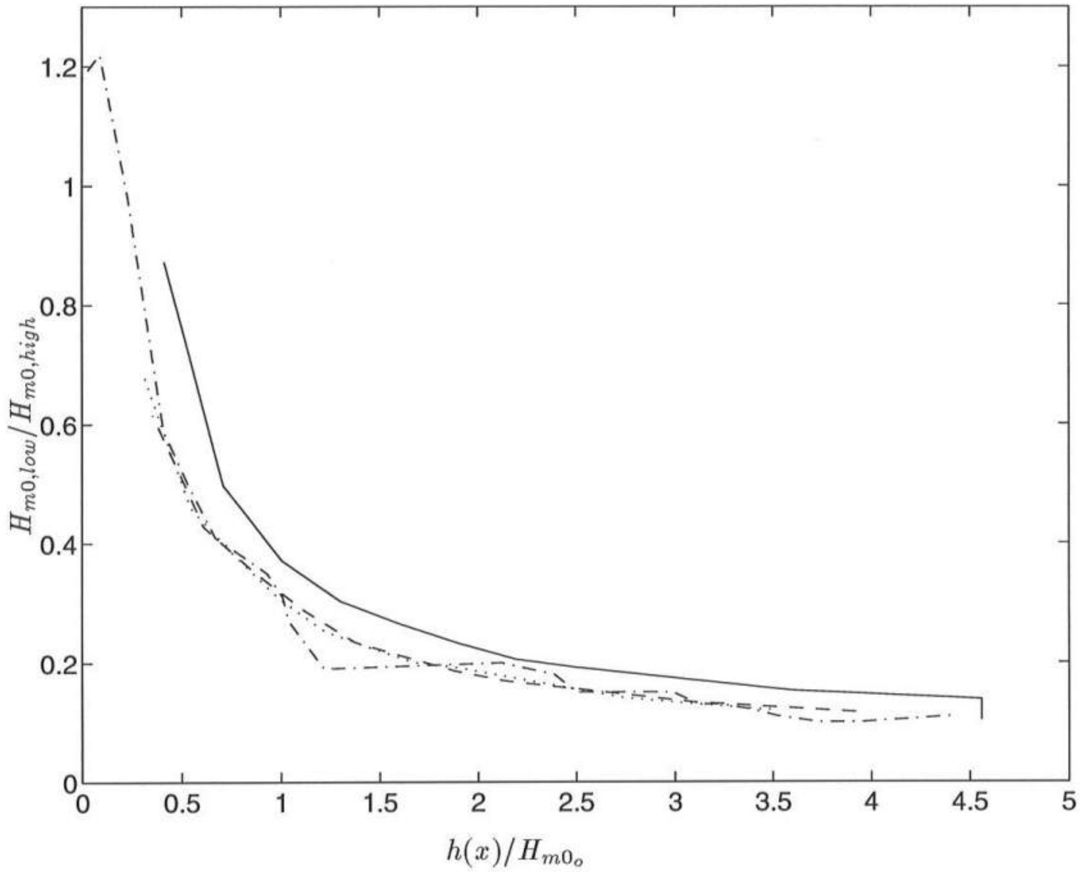

Figure 4.13: Ratio of low to high wave heights; (—) 7 *cm* run; (- - -) 8 *cm* run; (· · · · ·) 9 *cm* run; (-·-·-) SUPERTANK

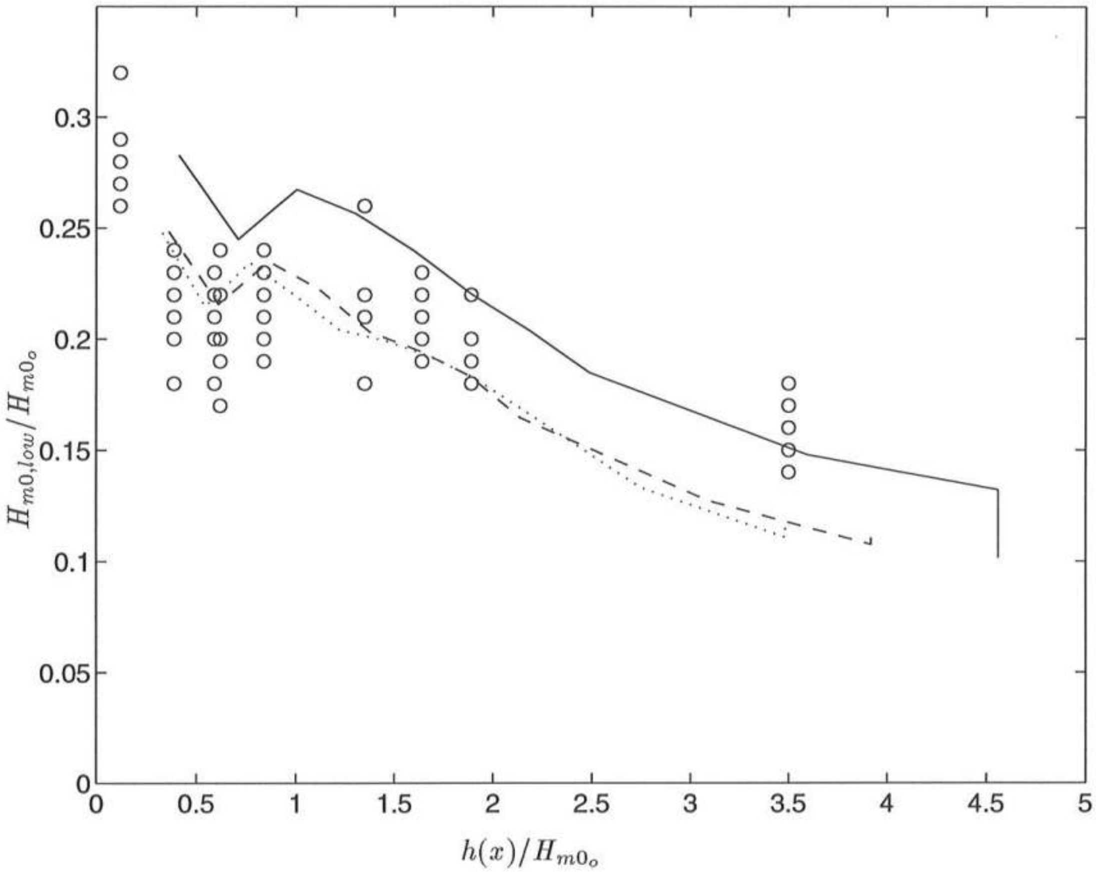

Figure 4.14: Normalized low frequency wave heights; (——) 7 *cm* run; (- - -) 8 *cm* run; (·····) 9 *cm* run; (ooooo) DELILAH

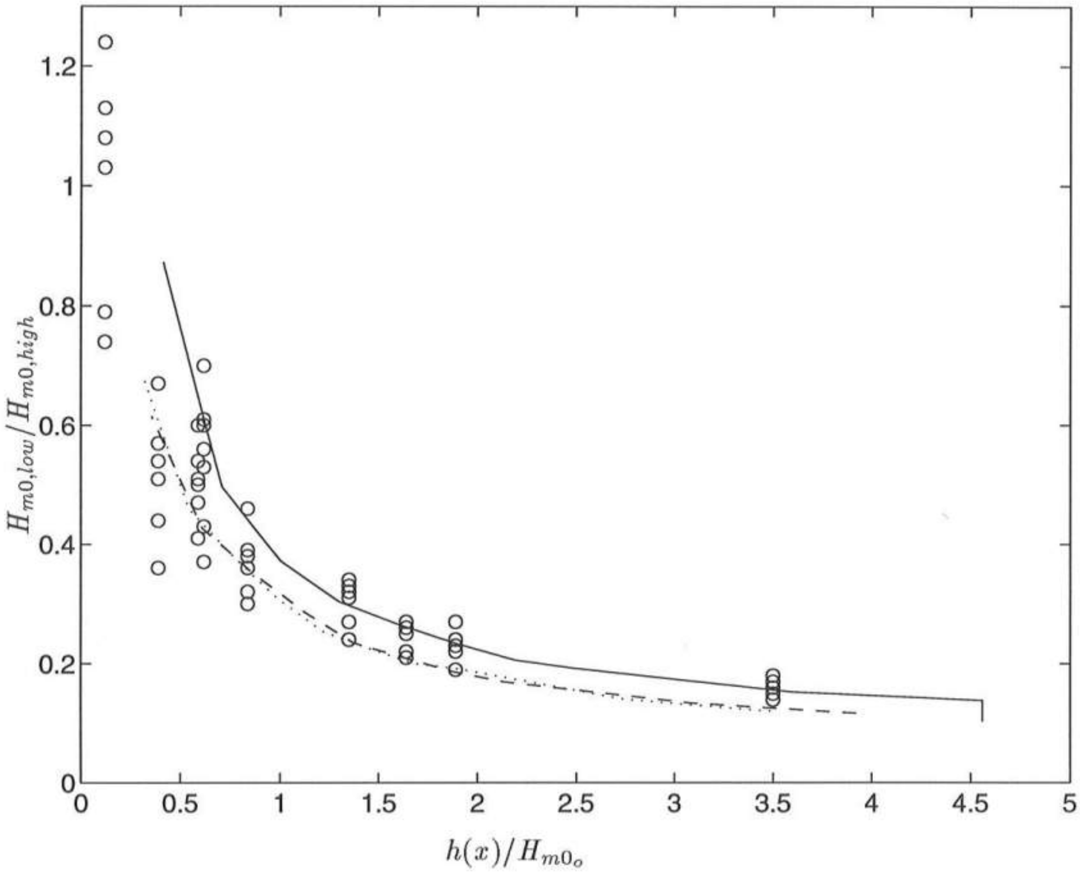

Figure 4.15: Ratio of low to high wave heights; (—) 7 *cm* run; (- - -) 8 *cm* run; (· · · · ·) 9 *cm* run; (ooooo) DELILAH

number of mathematical manipulations required. The most commonly applied approach to this problem is to shorten run duration by truncating the input spectra above a certain frequency. To date, the success of most research into numerical spectral shoaling and breaking models has been measured by a model's ability to return computed spectra that compare favorably to experimental data. Usually, the area of interest of the returned spectra is limited to the spectral peak and the first two to three harmonics. When one only wishes to examine this limited area, substantial computer time is saved, with a negligible effect on the returned spectra within the area of interest.

4.3.1 Effects on Wave Shape

When truncating the high end portion of the input spectra, it is found that third moment statistics computed from time series based on the returned spectra have lower values than those computed directly from measured data (Kirby, 1994). This warrants investigation into the contribution of the energy in the higher frequency modes of the laboratory data to the values of skewness and asymmetry.

The computational method used is as follows. First the spectrum is computed from the measured time series. Then, it is filtered above a certain frequency and inverse FFT'ed to produce a filtered time series. Skewness and asymmetry values are computed from the filtered time series according to Equations 3.1 and 3.2. When determining the cutoff frequency to be applied, 1.5 times the spectral peak frequency was used to filter above the spectral peak, 2.5 times the spectral peak frequency was used to filter above the second harmonic, and so on. Filtered time series were computed based on spectra truncated above the spectral peak, and the second, third, fourth, fifth, seventh, tenth and fifteenth harmonics.

Figures 4.16 and 4.17 show the shoreward evolution of skewness and asymmetry computed from time series based on the spectrum of the 7 *cm* run filtered above different cutoff frequencies. Figures 4.18 and 4.19 show the same values for the 8 *cm* run. These figures show a definite correlation between the portion of the measured spectrum used as input, and the accuracy of the third moments computed. For the 8 *cm* run, the skewness and asymmetry curves start to take on the correct shape only when one considers the tenth harmonic or so. For the 7 *cm* run, the convergence toward the measured values occurs with a lesser number of harmonics saved; however, as the spectral peak frequency of the 7 *cm* run is approximately twice that of the 8 *cm* run, only half as many harmonics need be retained to retain the same portion of the spectrum. This difference between measured values and filtered computed values of third moment statistics will become more important as increasingly sophisticated numerical spectral shoaling and breaking models are developed that use these values in their predictive scheme.

4.3.2 Filtered Time Series

Figures 4.20 through 4.22 show a portion of the measured time series for the 8 *cm* run with h=.44 m plotted *vs.* time series filtered above the spectral peak, the fifth harmonic, and the tenth harmonic, respectively. Figures 4.23 through 4.28 show the same comparisons with h=.211 m and h=.04 m, respectively. At all three locations, when only the spectral peak is retained, the wave crests are severely underpredicted (Figures 4.20, 4.23, and 4.26). At h=.44 m, the waves have traveled 3.0 meters from the wave paddle. Retaining the first five harmonics at this location yields very slight errors in the filtered time series (Figure 4.21), and retaining the first ten harmonics returns a filtered time series which is indistinguishable from the measured time series (Figure 4.22). This is expected, as the skewness and asymmetry have not yet begun to increase at this location. At h=.211 m, the waves have traveled 8.0 meters up the slope, and the measured skewness is nearing its peak. Here, retaining the first five harmonics (Figure 4.24) still yields wave crests that are severely underpredicted. In addition, the calculated values of the troughs are below the measured values. When the first ten harmonics are retained (Figure 4.25), the larger crests are still slightly underpredicted, whereas the troughs agree. As the measured skewness and asymmetry values are high in this region, the largest discrepancies may be expected. At h=.04 m, the waves have traveled 14.0 meters up the slope, and the measured skewness and asymmetry are both decreasing. Retaining the first five harmonics (Figure 4.27) yields crests that are underpredicted, but not to the extent that occurred at h=.211 m (Figure 4.24). Retaining the first ten harmonics yields very slight errors in the crests; however, the troughs are still underpredicted (Figure 4.28).

4.4 Overview of Spectral Shoaling and Breaking Models

Previous experimentation and modeling has shown that spectral shoaling models based on the Boussinesq equations can accurately predict wave height transformation and wave spectra and shape in the region prior to the occurrence of breaking, and models based on the nonlinear long wave equations can accurately predict the same quantities in the bore propagation region. However, an equally accurate parameterization of the breaking region, that would link the two extreme regions, has yet to be accomplished.

Attempts have been made to simulate breaking in spectral shoaling models by way of introducing a probabilistic dissipation term. One early attempt consisted of subtracting as a dissipation term a percentage of the energy in each frequency mode. As the percentage remained constant across the spectrum, the dissipation spectrum assumed the shape of the energy spectrum. Computer runs of this model exhibited gross errors in predictions of wave height transformation and energy spectra, and this model was subsequently discarded.

A subsequent model was based on the idea that since kinetic energy is localized near the front of the wave crests, dissipation should occur primarily in this region also. When examining dissipation in the time domain, one would then see a row of delta functions. The spectrum of this temporal distribution of delta functions will be nearly a white spectrum. Thus, in the numerical model, a constant amount of energy was subtracted from each frequency across the spectrum. This scenario enhanced the dissipation occurring in the higher frequency modes, where relatively less energy was present at the start. Kirby *et al.* (1990) demonstrated that this model was functional, but overpredicted the energy in the

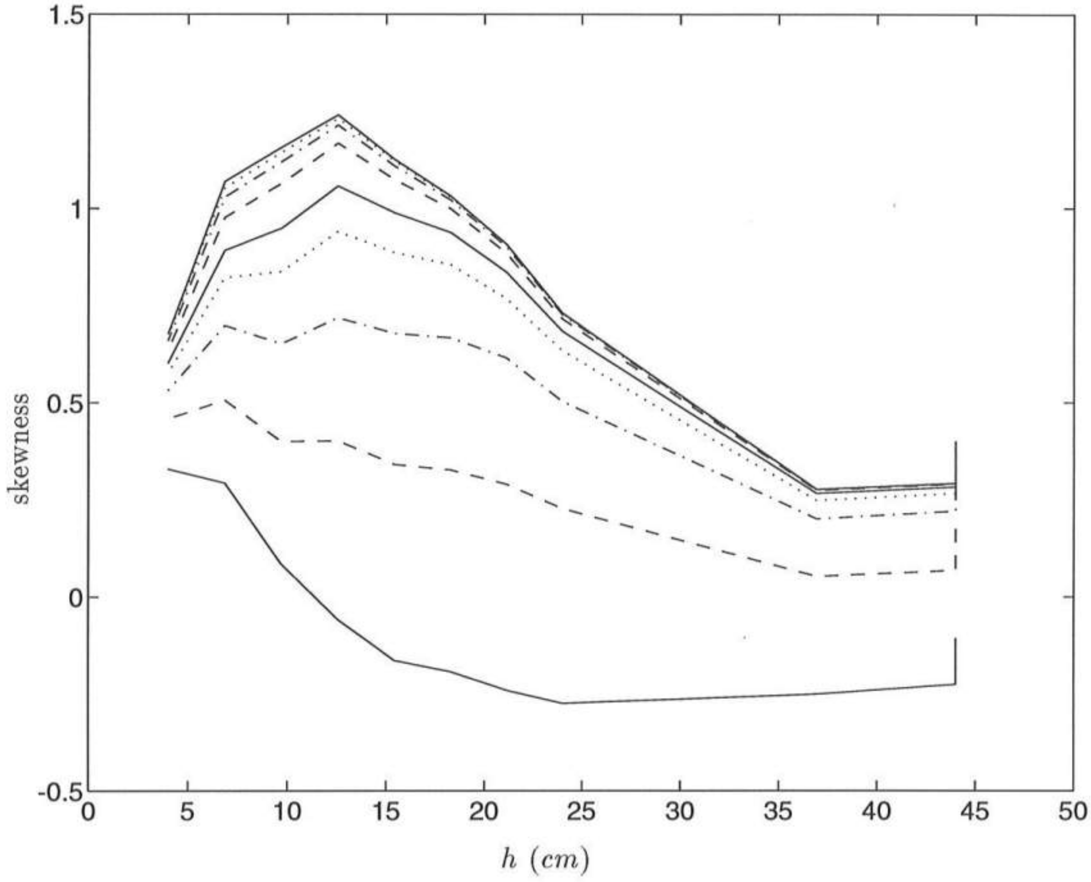

Figure 4.16: Shoreward evolution of skewness, 7 *cm* run; harmonics included (from bottom to top): (——) peak; (- - -) 2; (-·-·-) 3; (· · · · ·) 4; (——) 5; (- - -) 7; (-·-·-) 10; (· · · · ·) 15; (——) full spectrum

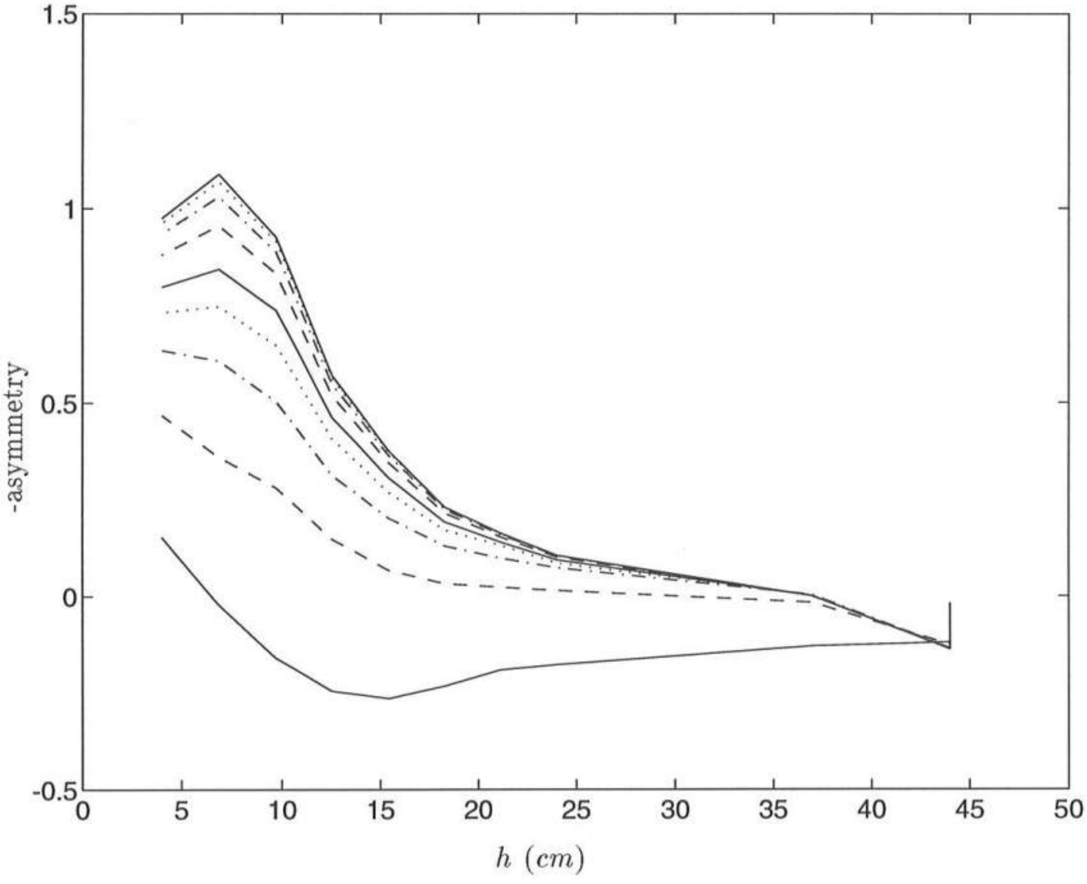

Figure 4.17: Shoreward evolution of asymmetry, 7 *cm* run; harmonics included (from bottom to top): (——) peak; (- - -) 2; (-·-·-) 3; (· · · · ·) 4; (——) 5; (- - -) 7; (-·-·-) 10; (· · · · ·) 15; (——) full spectrum

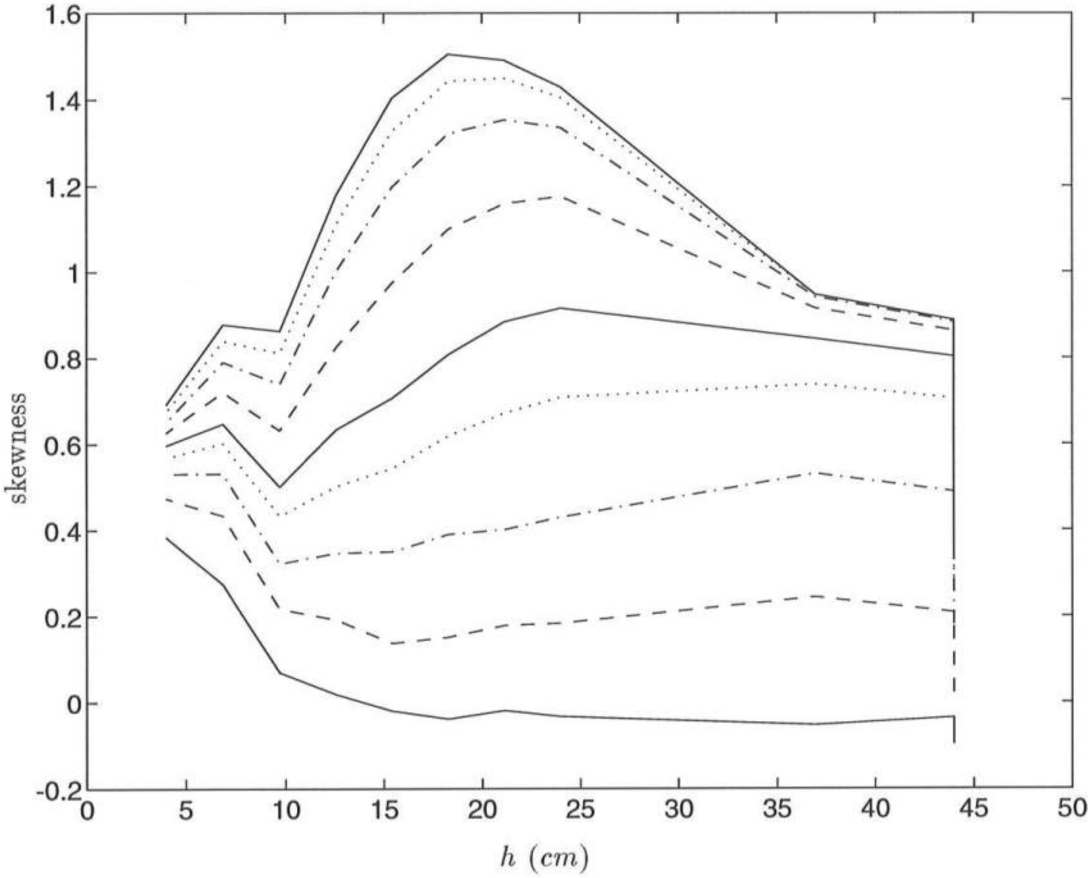

Figure 4.18: Shoreward evolution of skewness, 8 *cm* run; harmonics included (from bottom to top): (——) peak; (- - -) 2; (-·-·-) 3; (· · · · ·) 4; (——) 5; (- - -) 7; (-·-·-) 10; (· · · · ·) 15; (——) full spectrum

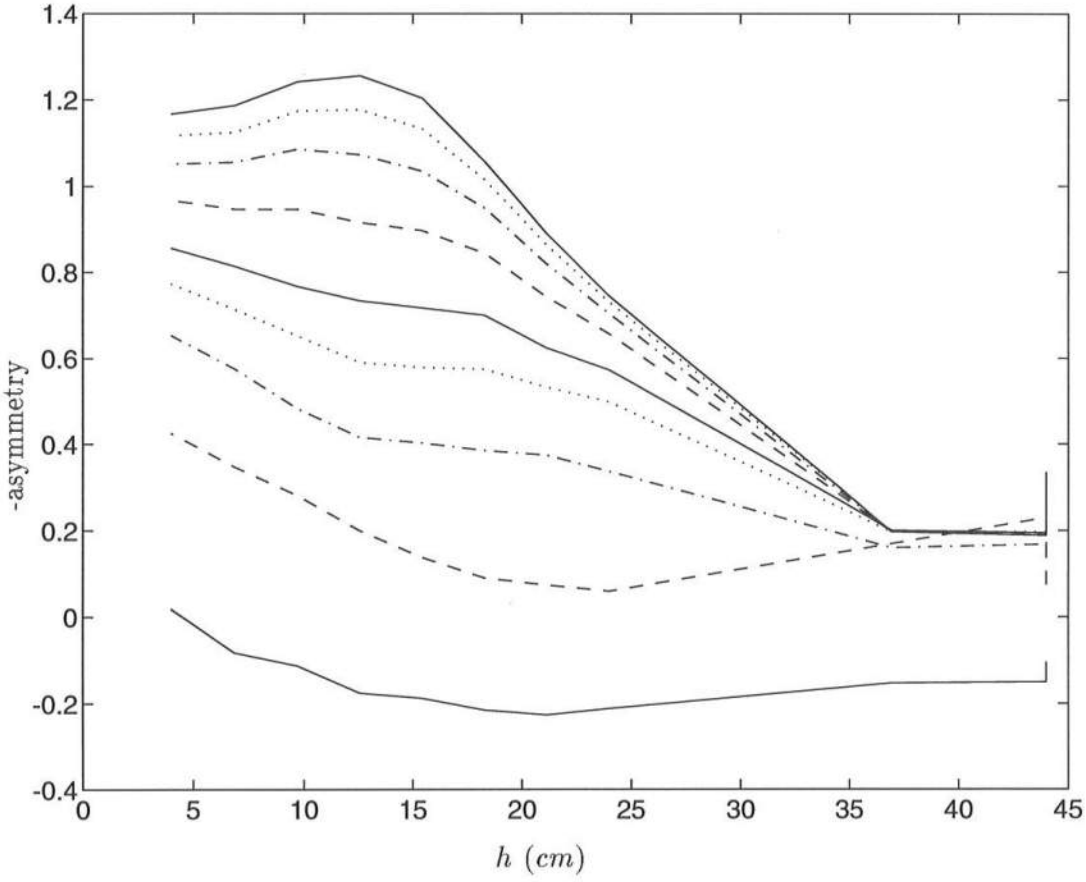

Figure 4.19: Shoreward evolution of asymmetry, 8 *cm* run; harmonics included (from bottom to top): (——) peak; (- - -) 2; (-·-·-) 3; (· · · · ·) 4; (——) 5; (- - -) 7; (-·-·-) 10; (· · · · ·) 15; (——) full spectrum

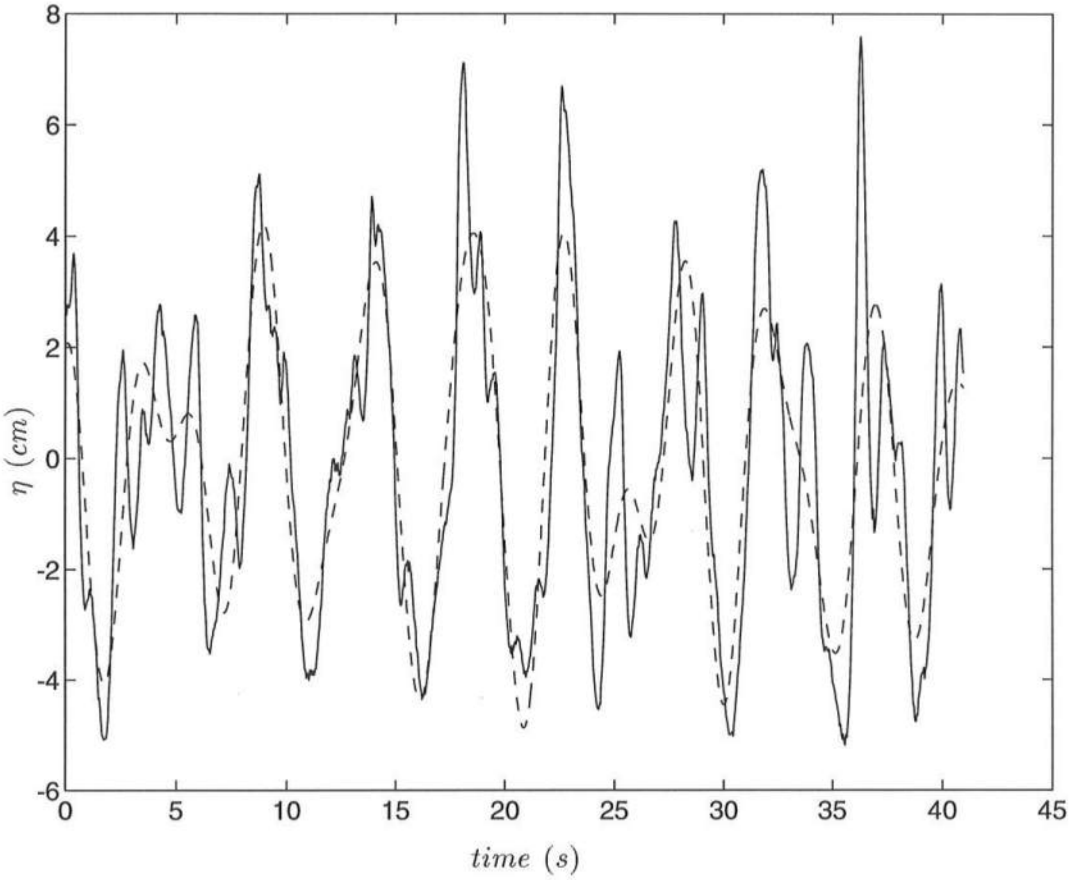

Figure 4.20: Surface displacement time series, 8 *cm* run, x=3.0 m, h=0.44 m; (- - -) spectrum filtered above peak; (—) full spectrum

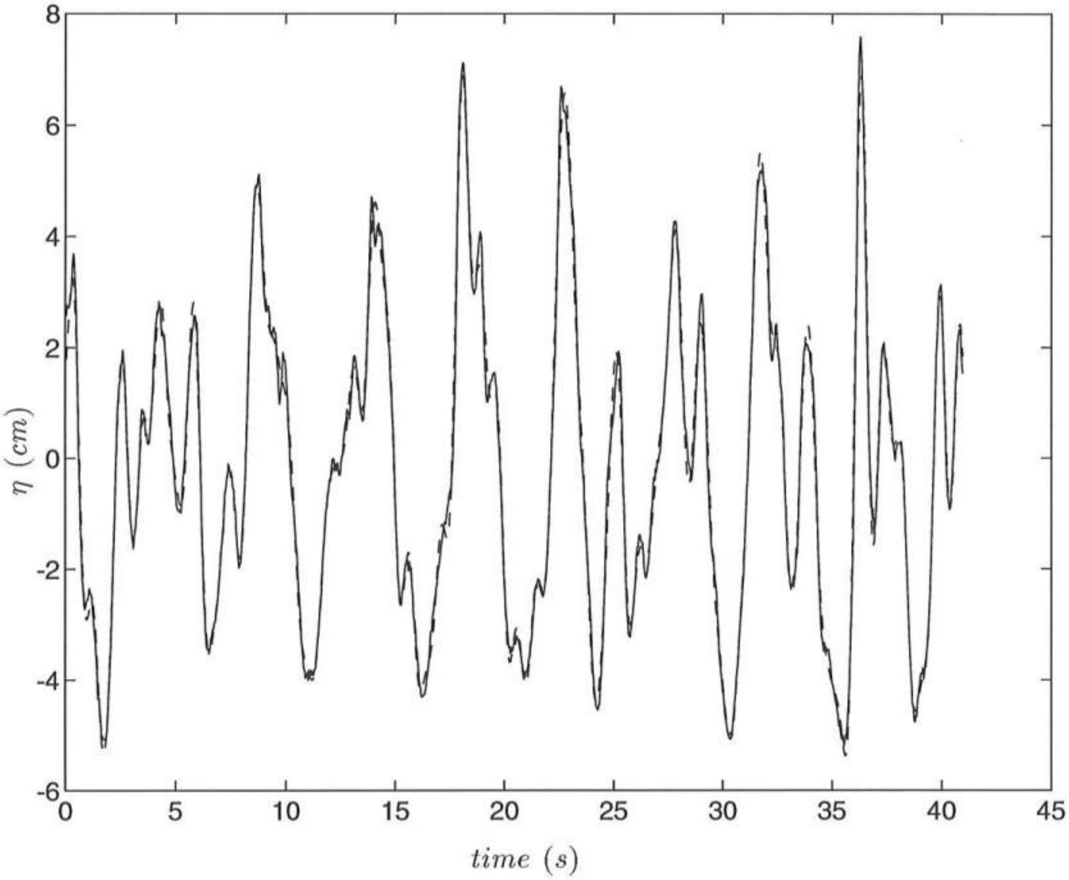

Figure 4.21: Surface displacement time series, 8 *cm* run, x=3.0 m, h=0.44 m; (- - -) spectrum filtered above 5^{th} harmonic; (—) full spectrum

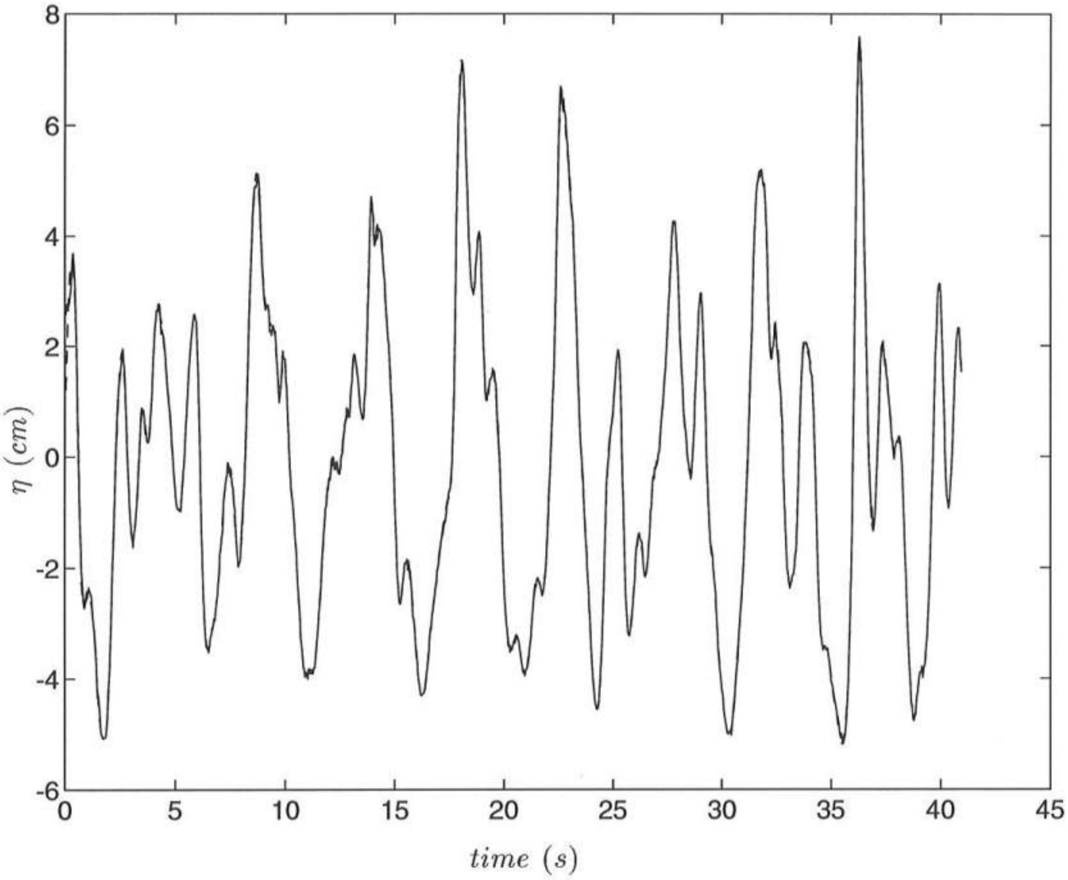

Figure 4.22: Surface displacement time series, 8 *cm* run, x=3.0 m, h=0.44 m; (- - -) spectrum filtered above 10^{th} harmonic; (—) full spectrum

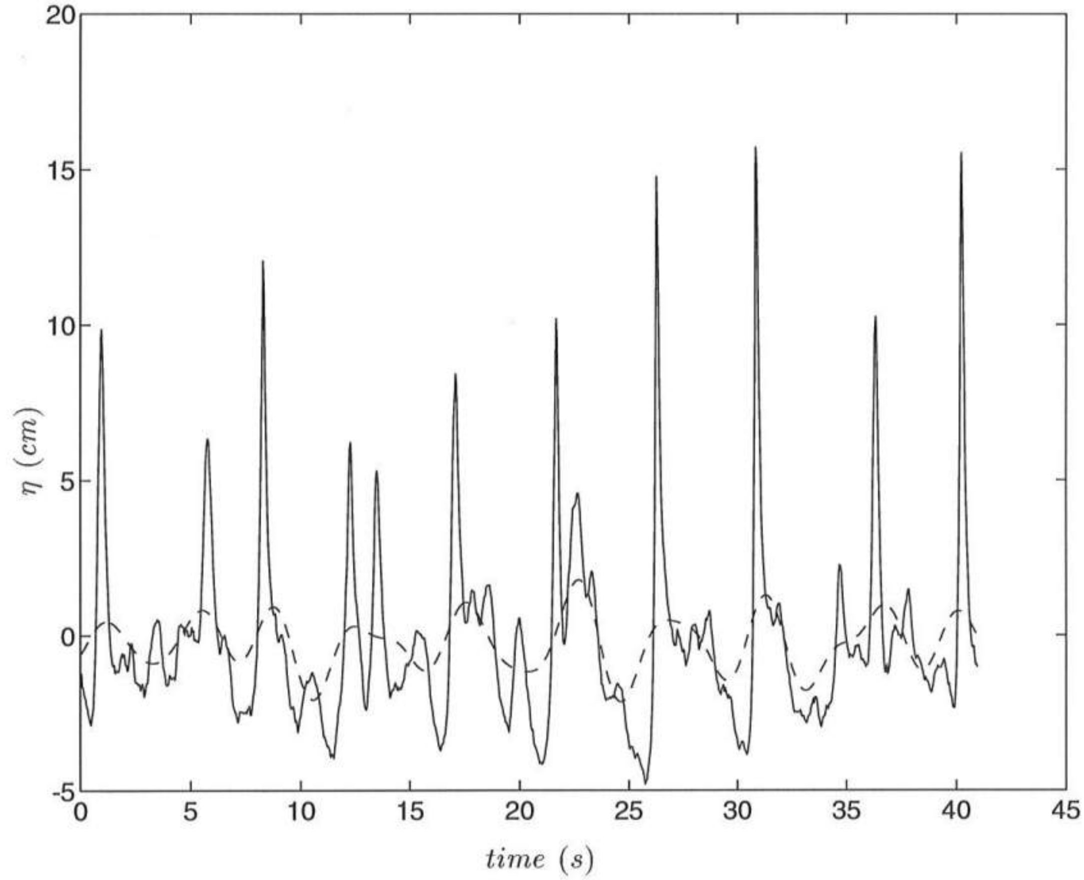

Figure 4.23: Surface displacement time series, 8 *cm* run, x=19.5 m, h=0.211 m; (- - -) spectrum filtered above peak; (—) full spectrum

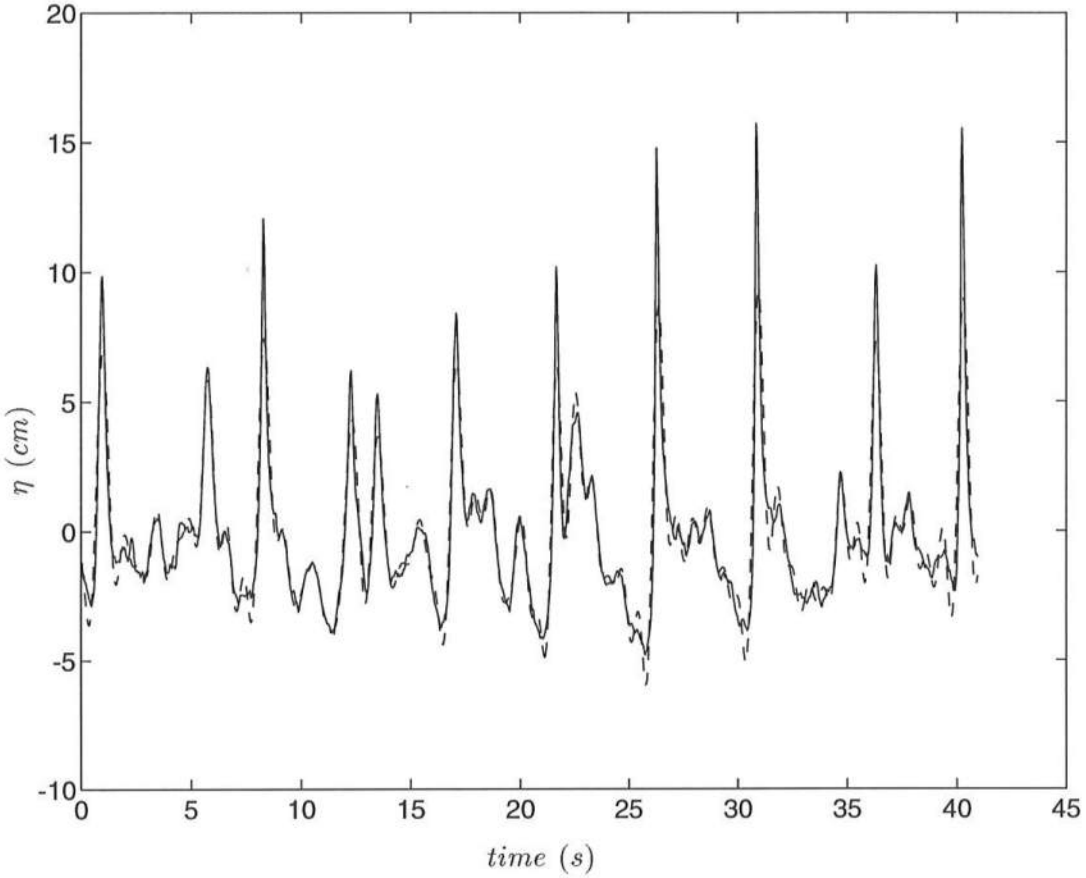

Figure 4.24: Surface displacement time series, 8 *cm* run, x=19.5 m, h=0.211 m; (- - -) spectrum filtered above 5^{th} harmonic; (—) full spectrum

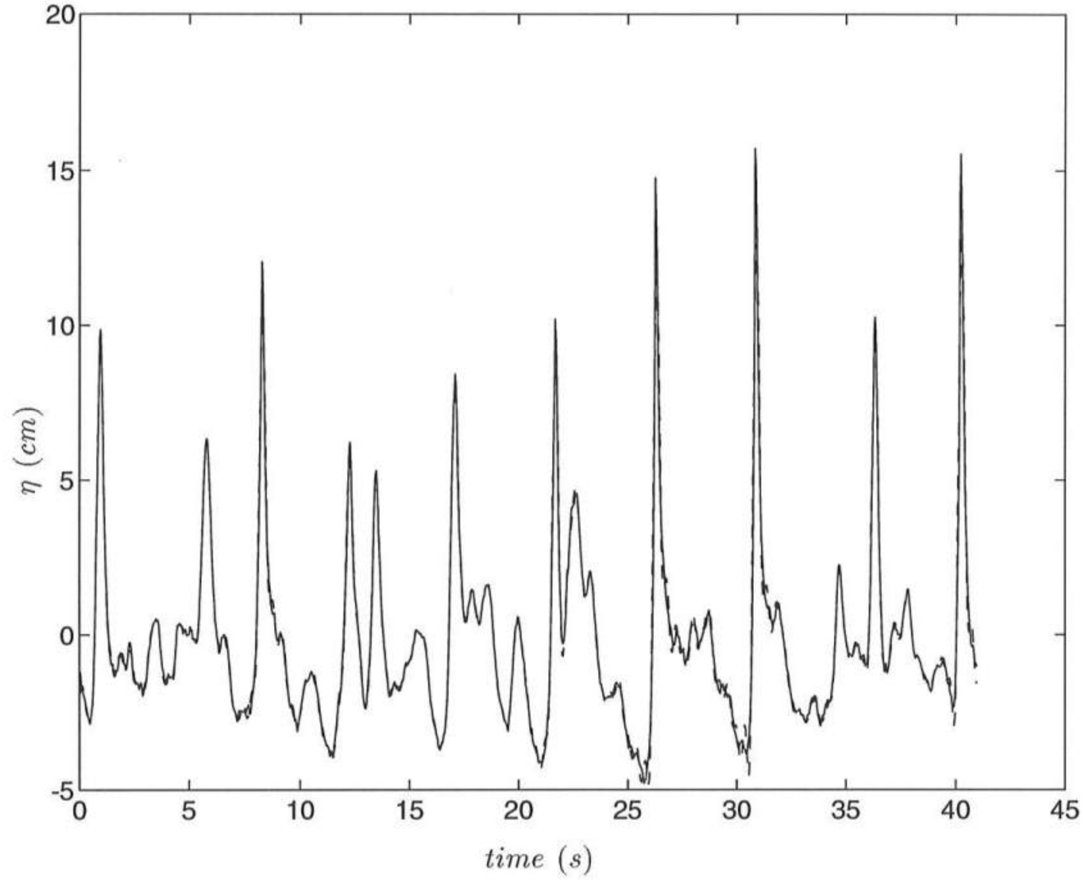

Figure 4.25: Surface displacement time series, 8 *cm* run, x=19.5 m, h=0.211 m; (- - -) spectrum filtered above 10^{th} harmonic; (—) full spectrum

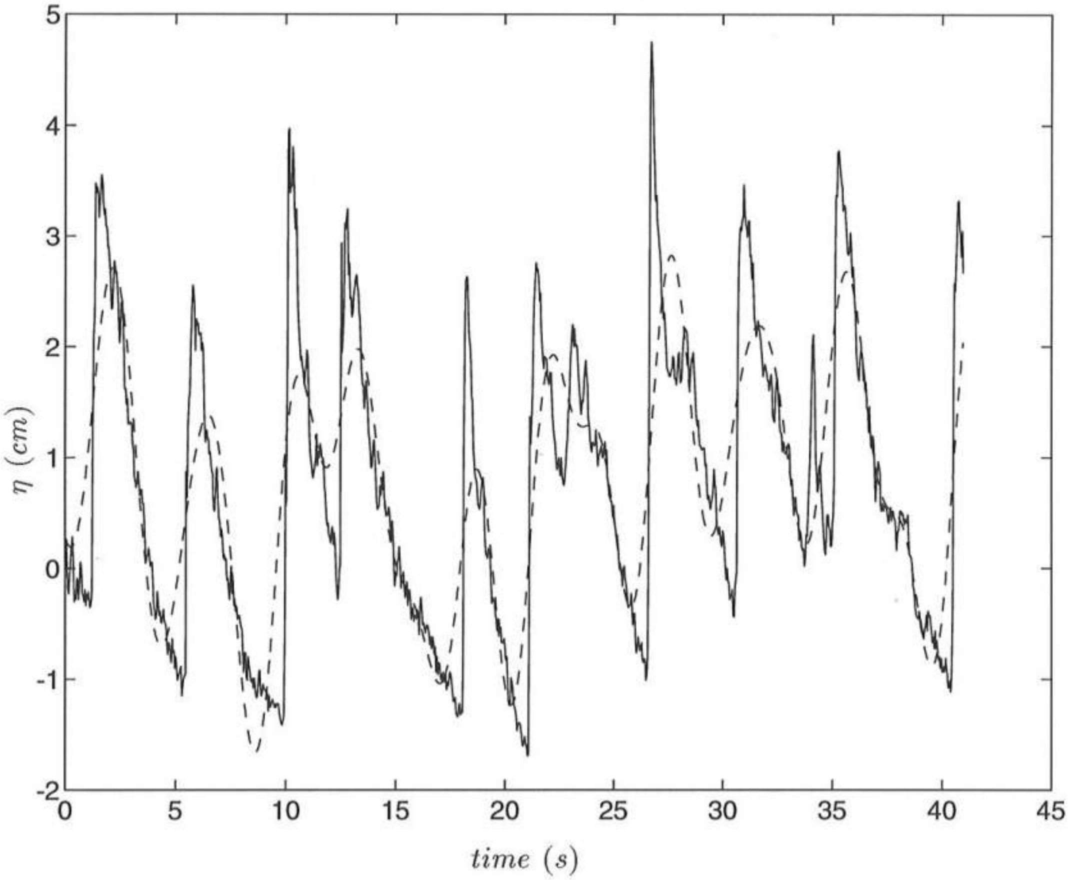

Figure 4.26: Surface displacement time series, 8 *cm* run, x=25.5 m, h=0.04 m; (- - -) spectrum filtered above peak; (—) full spectrum

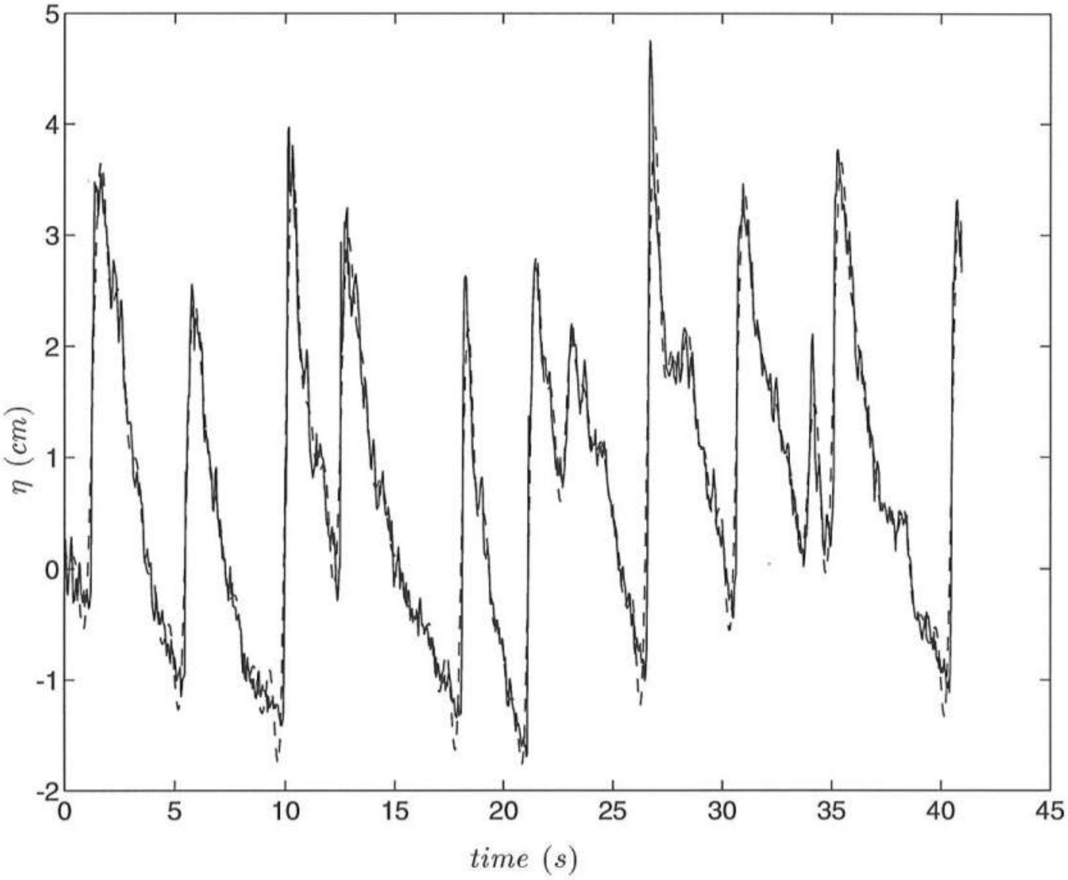

Figure 4.27: Surface displacement time series, 8 *cm* run, x=25.5 m, h=0.04 m; (- - -) spectrum filtered above 5^{th} harmonic; (—) full spectrum

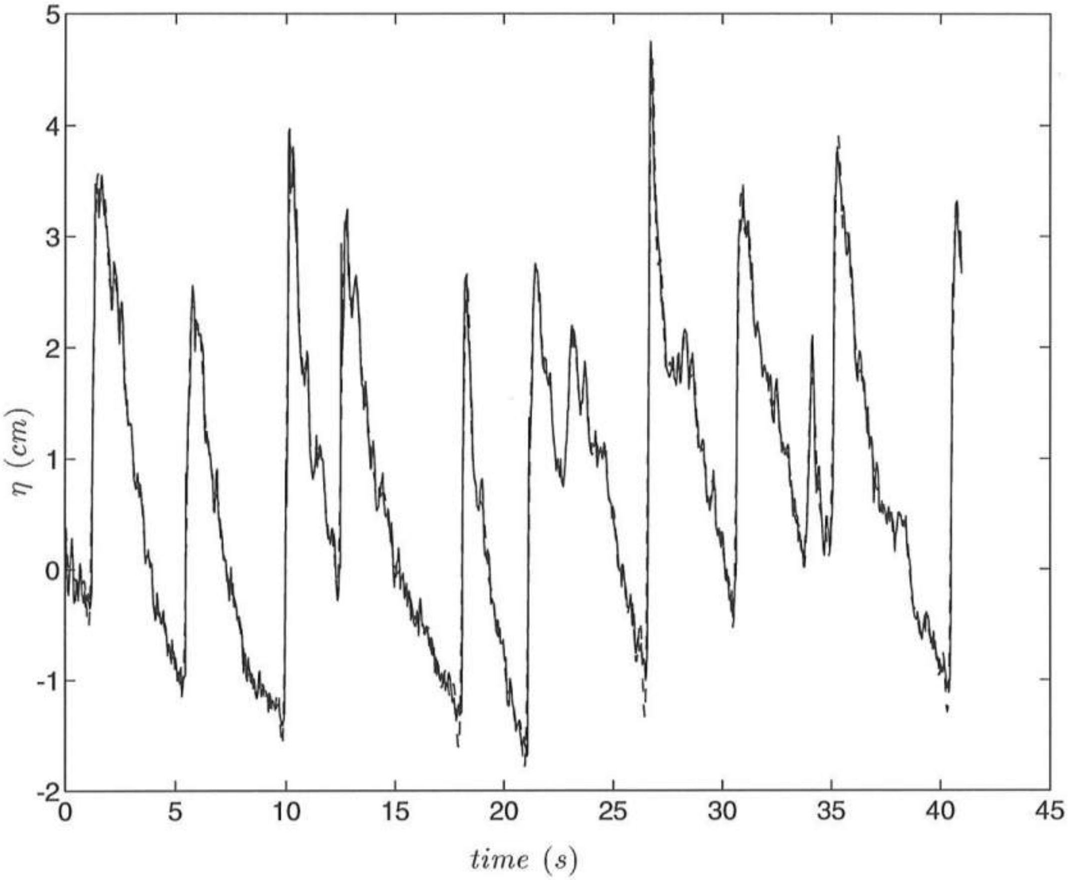

Figure 4.28: Surface displacement time series, 8 *cm* run, x=25.5 m, h=0.04 m; (- - -) spectrum filtered above 10^{th} harmonic; (—) full spectrum

high frequency tail of the spectrum.

Mase and Kirby (1992) compared the model of Kirby *et al.* (1990) to a hybrid model in which the dissipation term was composed of two components. The first was the constant amount of Kirby *et al.* (1990) and the second was a dissipation spectrum with an f^2 shape. This new model increased further the amount of energy dissipated in the higher frequency modes, and was seen to improve on the results of Kirby *et al.* (1990).

4.5 Simple Eddy Viscosity Model

All of the previously mentioned spectral models were probabilistic in nature and depended on a semi-empirical dissipation term, α. Spectra and wave heights were reproduced with increasing accuracy, while predictions of wave shape remained uniformly poor. (We now see that this may be due in large part to errors induced by truncating input spectra, as described in Section 4.3.)

In the current eddy viscosity time domain model, the strength or lack of the dissipation term is a function of the wave shape. This physical significance was lacking in the spectral shoaling models, where α was responsible for dissipation (although in small amounts) from the onset of modeling.

4.5.1 Mixing Length Parameter

Theoretical Background

Kirby and Wei (1994) add a dissipative term to the extended Boussinesq equations (written with tensor notation) of Nwogu (1993), resulting in

$$\eta_{,t} + [(h+\eta)u_i]_{,i} + \left\{ \left(\frac{z_\alpha^2}{2} - \frac{h^2}{6} \right) h u_{j,ji} + \left(z_\alpha + \frac{h}{2} \right) h (h u_j)_{,ji} \right\}_{,i} = 0 \tag{4.10}$$

$$u_{i,t} + g\eta_{,i} + u_j u_{i,j} + z_\alpha \left\{ \frac{z_\alpha}{2} u_{j,ji} + (h u_j)_{,ji} \right\}_{,t} - (\nu_b u_{i,j})_{,j} = 0 \tag{4.11}$$

where the eddy viscosity is defined as

$$\nu_b = -l^2 u_{j,j}. \tag{4.12}$$

The mixing length l is related to water depth by the mixing length parameter δ as

$$l = \delta(h+\eta). \tag{4.13}$$

Substituting Equation 4.13 into Equation 4.12, the eddy viscosity is rewritten as

$$\nu_b = -B\delta^2 h^2 u_{i,j} \tag{4.14}$$

following Zelt (1991). The parameter B determines the relative strength of the dissipation term. Whereas Zelt (1991) writes B in terms of a critical value of the velocity gradient, Kirby and Wei (1994) redefine B for ease of computation in terms of the change in the free surface and state

$$B = \left\{ \begin{array}{ccc} 1 & if & \eta_t \geq 2\eta_t^* \\ \left(\frac{\eta_t}{\eta_t^*} - 1\right) & if & \eta_t^* \leq \eta_t < 2\eta_t^* \\ 0 & if & \eta_t < \eta_t^* \end{array} \right. \tag{4.15}$$

where the critical slope is defined as

$$\eta_t^* = 0.3\sqrt{gh}. \tag{4.16}$$

Thus, dissipation is only applied when the slope of the passing wave exceeds the specified critical slope. The strength of the dissipation term is increased as the passing wave's slope increases. As the tail of the wave passes, the critical slope will not be met, B will equal 0, and dissipation will not be applied.

In order to compute δ, Kirby and Wei (1994) construct a statistical estimate of dissipation at a point as

$$\langle E\rangle_t + \langle F\rangle_x = -\langle\epsilon_b\rangle \tag{4.17}$$

where the local energy density

$$E = \frac{1}{2}\rho g\eta^2 + \frac{1}{2}\rho h u^2 \tag{4.18}$$

so that $\langle E\rangle_t = 0$ for a spectrum stationary in time, and the local energy flux

$$F = \rho g h \eta u. \tag{4.19}$$

Substituting Equation 4.19 into Equation 4.17 yields

$$\langle\frac{\rho}{h}\eta(\nu_b\eta_t)_t\rangle = -\langle\epsilon_b\rangle. \tag{4.20}$$

Equation 4.20 is then solved with δ=1, and compared to the prediction of $\langle\epsilon_b\rangle$ in Equation 3.4 (Thornton and Guza, 1983). These two quantities allow computation of δ as

$$\delta = (\langle\epsilon_b\rangle_{TG}/\langle\epsilon_b\rangle_{\delta=1})^{1/2} \tag{4.21}$$

Data Comparison

Kirby and Wei (1994) assume δ to be dependent on h, $\overline{f}$ and H_{rms}, for which dimensional analysis shows

$$\delta = F(\frac{H_{rms}}{h}, \left(\frac{h}{g}\right)^{1/2}\overline{f}). \tag{4.22}$$

Figure 4.29 shows a contour plot of δ which reveals that δ is not dependent on $\overline{f}$. Table 4.3 lists the values of δ computed and the percentage of waves broken for the 7 *cm*, 8 *cm*, and 9 *cm* runs.

Table 4.3: Evolution of δ for 7 *cm*, 8 *cm*, and 9 *cm* runs

h	7 *cm* run		8 *cm* run		9 *cm* run	
(m)	δ	% broken	δ	% broken	δ	% broken
0.333	0.631	1.24	0.472	9.04	0.405	8.57
0.269	0.360	4.45	0.337	12.68	0.077	19.92
0.240	0.360	8.44	0.221	19.80	0.216	30.89
0.211	0.329	16.50	0.223	30.20	0.216	42.80
0.183	0.343	27.58	0.234	42.53	0.265	54.89
0.154	0.366	40.70	0.268	52.61	0.316	66.07
0.126	0.412	60.00	0.370	69.26	0.426	84.69
0.097	0.469	75.07	0.581	77.12	0.692	81.01
0.069	0.538	83.03	0.838	84.94	0.989	93.06
0.040	1.598	83.27	2.805	86.41	3.263	85.88

In analyzing the broken solitary wave runup data of Synolakis (1987), Zelt (1991) determined that specifying δ=2 resulted in accurate predictions of the dissipation in the inner surfzone. Kirby and Wei (1994) analyze the data of Mase and Kirby (1992) and witness a slow, smooth growth of δ, with values less than 1, until the inner surfzone is reached, at which point a sudden jump in the value of δ occurs. The present data indicate the same trend, as Table 4.3 shows a large increase in the value of δ at the shoremost gage. (In the breaking spectra plots for the 7 *cm*, 8 *cm*, and 9 *cm* runs shown in Figures 3.3, 3.5, and 3.7, a sharp decrease is seen in the high frequency tail of the spectrum at the shoremost gage for each run.) The values of δ at h=0.04 *m* (1.598 for the 7 *cm* run, 2.805 for the 8 *cm* run, 3.263 for the 9 *cm* run) are in rough agreement with Zelt (1991).

4.5.2 Spectral Tail Dissipation

Kirby and Wei (1994) consider the case of a single peaked spectrum whose tail decays smoothly as $f^{-\alpha}$. They write the amplitude spectrum as

$$A_n = an^{-\alpha/2}. \tag{4.23}$$

Taking the natural logarithm of both sides of Equation 4.23 yields

$$\ln A_n = -\frac{\alpha}{2}\ln n + \ln a \tag{4.24}$$

which is a linear equation as $y = mx + b$. With A_n and n known, a linear least squares fit may be used to determine α. The viscosity spectrum is written as

$$\nu_{bn} = \nu_1 n^{-\beta/2} \tag{4.25}$$

Table 4.4: Spectral tail decay coefficients, 7 *cm* run

h m	α	β
0.440	4.24	0.059
0.369	4.67	0.052
0.240	4.13	0.263
0.154	3.28	0.223
0.097	2.65	0.212
0.040	2.24	0.122

and β is computed in the same fashion as α.

Kirby and Wei (1994) apply this formulation to the data set of Mase and Kirby (1992). The spectral tail is taken as the region from the spectral peak to 2.5 *Hz*, which was the highest frequency saved in the modeling. Figure 4.30 shows a log-log plot of the spectrum at x=3.0 *m* and h=0.44 *m* for the 7 *cm* run. Here, the spectral tail is taken as the region from the spectral peak to 5.0 *Hz*, where the spectrum is nearing a noise floor.

Surface Displacement Spectra

Figure 4.31 shows the tail of a surface displacement spectrum for the 7 *cm* run *vs.* the power law of Equation 4.23 at 6 locations, with h ranging from 0.44 *m* to 0.04 *m*. The spectral tails are modeled by the power law, and Equation 4.23 is shown to be a valid representation of the surface displacement spectrum. Table 4.4 lists the values of α for the 7 *cm* run, which decrease from about 4 at h=0.44 *m* to about 2 at h= 0.04 *m*. Kirby and Wei (1994) find the same evolution of the value of α in the data of Mase and Kirby (1992).

Viscosity Spectra

Figure 4.32 shows the tail of a viscosity spectrum for the 7 *cm* run *vs.* the power law of Equation 4.24 at the same 6 locations as above. The computed values of β are listed in Table 4.4. As the data of Mase and Kirby (1992) shows (Kirby and Wei, 1994), the present data also exhibit much stronger second harmonic in the viscosity spectra than in the surface displacement spectra. Both of these data show that modeling the viscosity spectra as Equation 4.24 yields inaccuracies.

Comparison of Decay Parameters

Figure 4.33 shows the computed values of β *vs.* those of α for the 7 *cm* run. A linear relation yields

$$\beta = 0.26 - 0.03\alpha. \tag{4.26}$$

The data of Mase and Kirby (1992) yields

$$\beta = 0.31 - 0.07\alpha \tag{4.27}$$

(Kirby and Wei, 1994). As Kirby and Wei (1994) suggest, approximating β as a constant, with a value of about 0.15, would be appropriate based on this analysis.

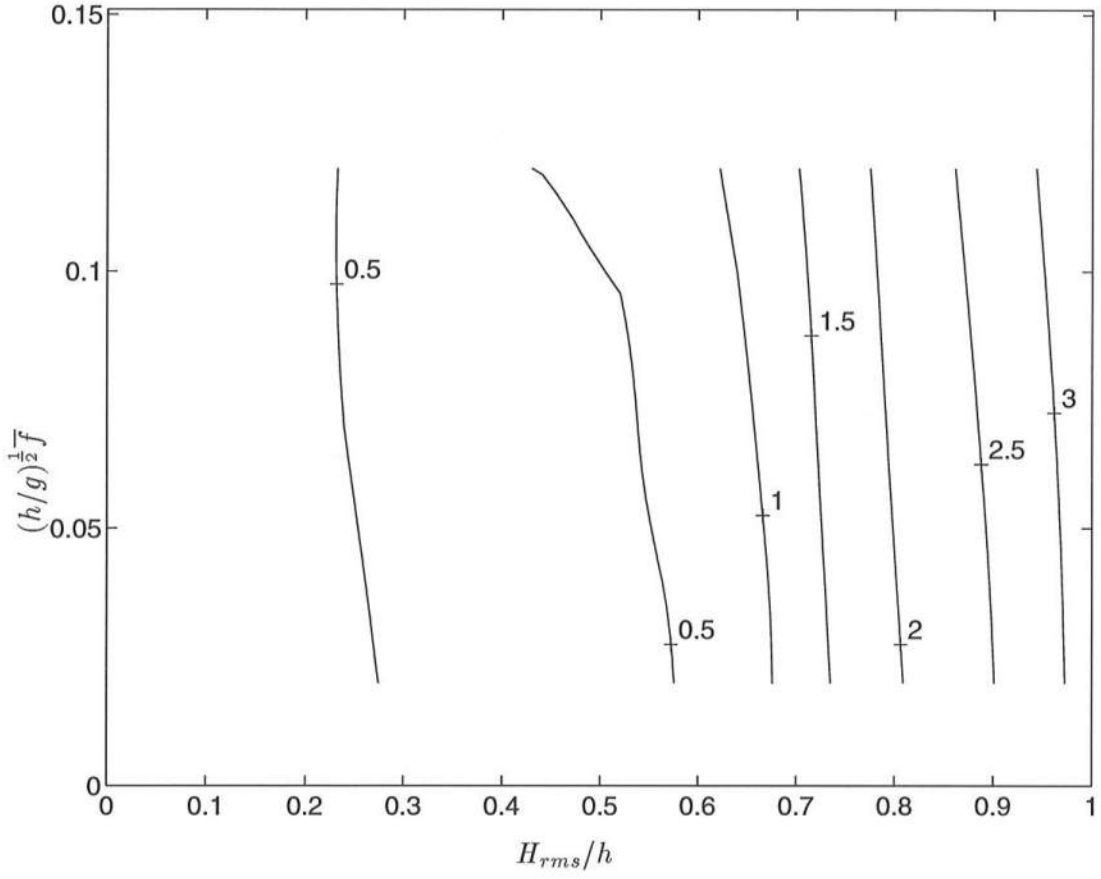

Figure 4.29: Contour plot of δ, 7 cm run

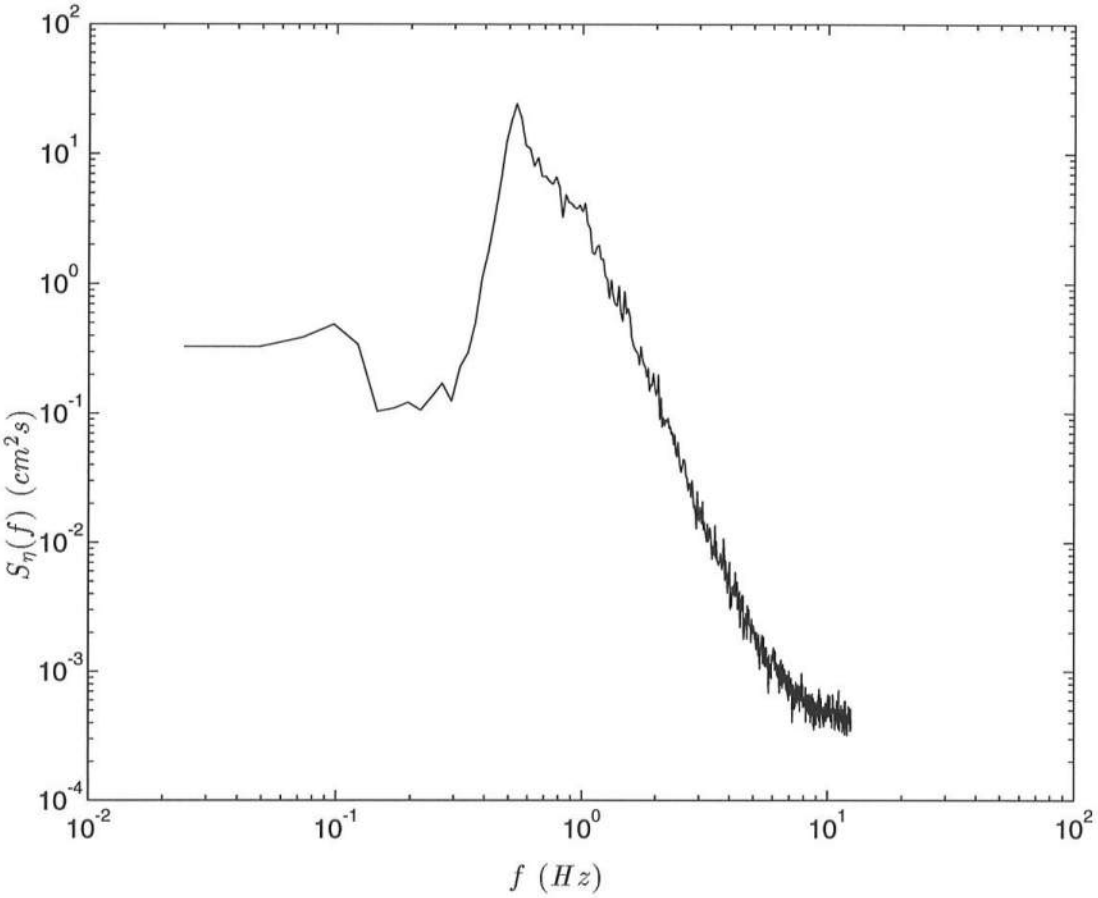

Figure 4.30: Energy spectrum log-log plot, 7 *cm* run, x=3.0 *m*, *h*=0.44 *m*

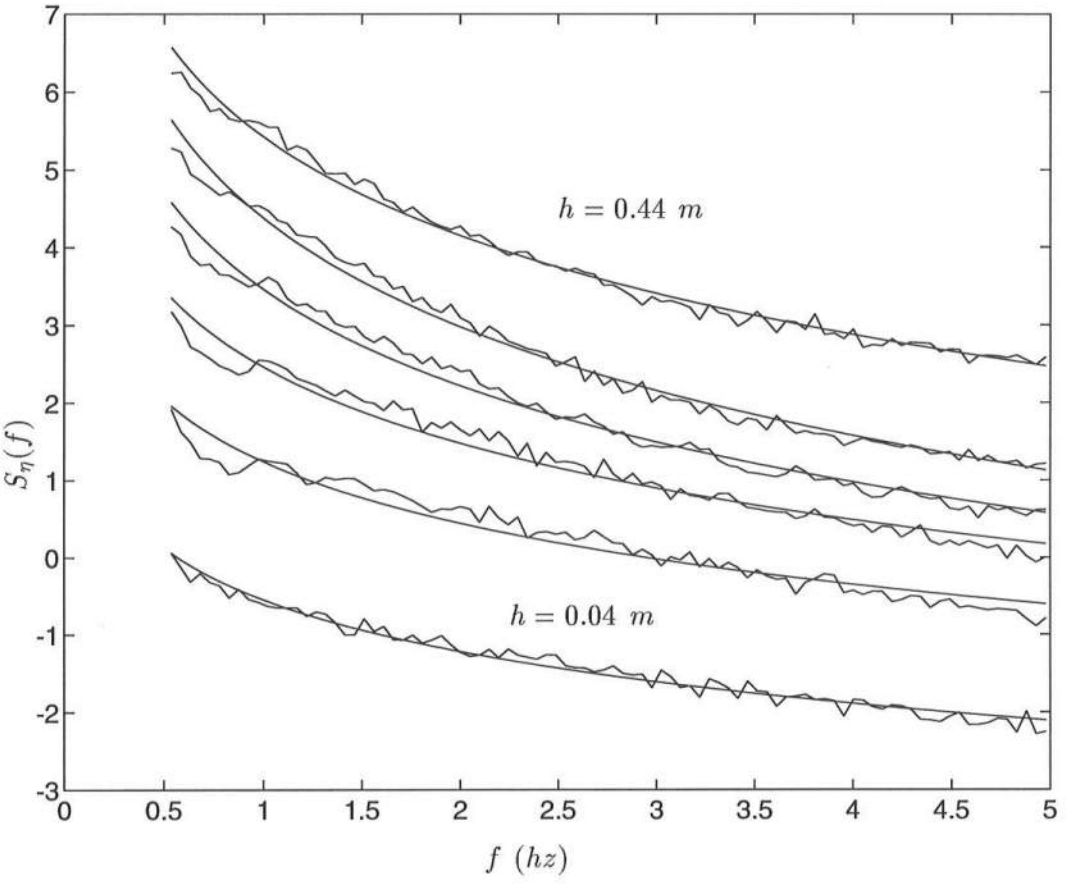

Figure 4.31: Power law fit to spectrum of η, 7 *cm* run; from bottom to top: h=0.04 *m*, h=0.097 *m*, h=0.154 *m*, h=0.240 *m*, h=0.369 *m*, h=0.44 *m* (from bottom, each curve was offset by an additional unit on the vertical axis to clearly show the evolution of the curve shape)

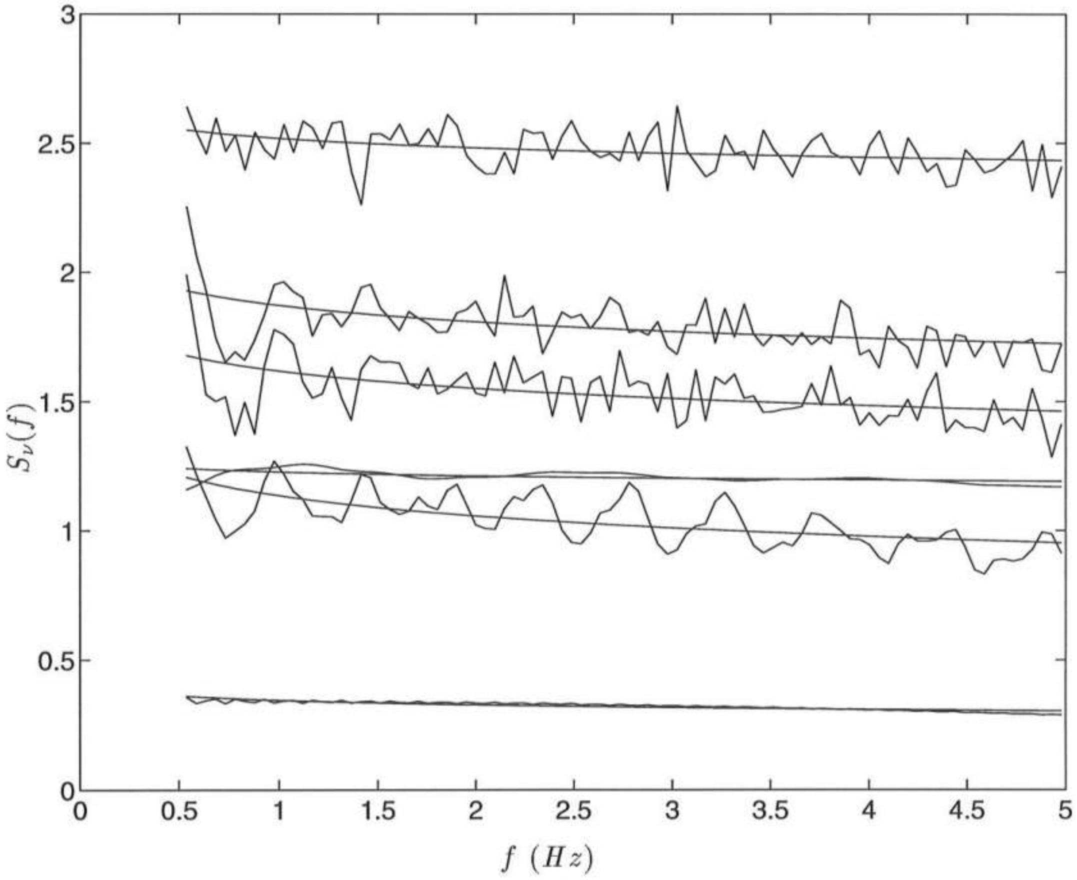

Figure 4.32: Power law fit to spectrum of ν_b, 7 *cm* run; from bottom to top: h=0.44 *m*, h=0.240 *m*, h=0.369 *m*, h=0.154 *m*, h=0.097 *m*, h=0.04 *m*

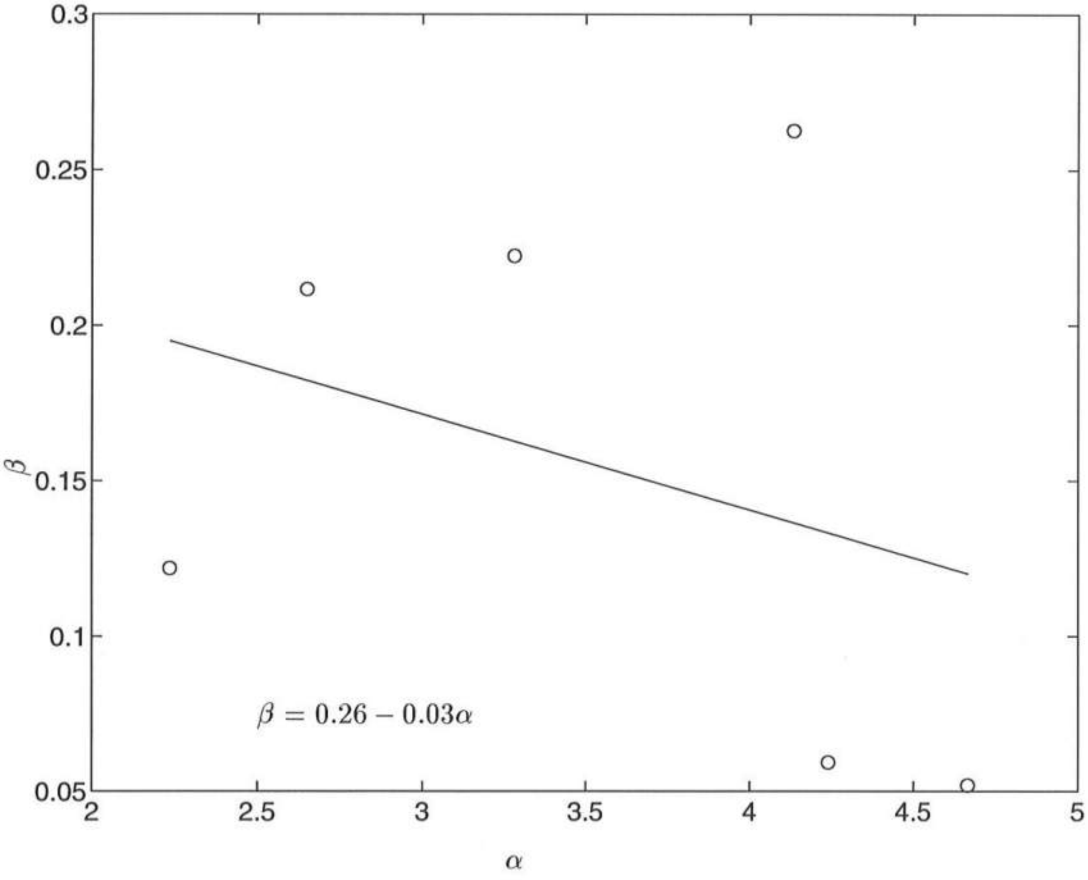

Figure 4.33: β *vs.* α, 7 *cm* run

Chapter 5

Conclusion

Due to the number of trials conducted and number of gage locations tested, the experiments conducted for this thesis provide a valuable data set for those interested in modeling the surfzone. The comparisons made herein are meant to provide information about the tradeoffs encountered when relying on laboratory data *vs.* field data as input for numerical shoaling and breaking models. A future study comparing skewness and asymmetry values computed from time series measured in the precision wave flume and time series measured in field experiments would be useful to determine what if any differences can be identified, and if their causes can be quantified. Accurate predictions of wave shape will become more and more important, as these characteristics are being increasingly considered in applying dissipation in a numerical model's predictive scheme.

As mentioned earlier, laboratory experiments are a less expensive method of gathering the extensive data records required for numerical modeling than field experiments are. But there are inherent drawbacks that the scientist and engineer must be cognizant of, mainly situations which do not occur in nature, and are unique to the lab environment, such as reflection off of the side walls of a tank or flume, or situations which do occur in nature, but are so distorted by scaling effects in the lab environment as to possibly render measured data meaningless, such as seiching. Analysis presented in Chapter 4 shows that reproduction of energy in the low frequency modes of the spectrum in the precision wave flume is in close agreement with that of a larger scale wave flume experiment with a sand beach, and a full scale comprehensive field experiment, although not for the same physical reasons. Thus, an experimental facility should be thoroughly tested so that any idiosyncracies may be identified and removed from the data record if possible, or at least factored in to conclusions drawn based upon the analysis of measured data or model results that used the measured data as input.

Bibliography

Cox, D.T., Irregular Wave Reflection and Runup on Rough, Permeable Slopes, Master's thesis, Department of Civil Engineering, University of Delaware, 1989.

Cox, D.T., N. Kobayashi and A. Wurjanto, Computer Programs for Spectral and Time Series Analyses for Random Waves, *University of Delaware Department of Civil Engineering Center for Applied Coastal Research, Research Report CACR-91-06*, Newark, DE, 1991.

Elgar, S., R.T. Guza and R.J. Seymour, Wave Group Statistics from Numerical Simulation of a Random Sea, *Applied Ocean Research*, 7(2), pp. 93-96, 1985.

Ferriole, M.A., Laboratory Observations of the Evolution of Surface-Gravity Waves Through the Shoaling and Breaking Regions and the Surfzone, Master's thesis, Department of Electrical Engineering, Washington State University, 1991.

Goda, Y., *Random Seas and Design of Maritime Structures*, University of Tokyo, 1985.

Kirby, J.T., Personal communication, 1994.

Kirby, J.T., J.M. Kaihatu, G.D. Bowen and J.M. Smith, Applications of Boussinesq Shoaling Models to Nearshore Wave Climate, in *Transactions of the American Geophysical Union Fall Meeting, EOS Supplement*, p. 1369, San Francisco, CA, 1990.

Kirby, J.T. and G. Wei, Application of a Simple Eddy Viscosity Model to Random Breaking Waves, Unpublished manuscript, 1994.

Kitaigorodskii, S.A., V.P. Krasitskii and M.M. Zaslavskii, On Phillips' Theory of Equilibrium Range in the Spectra of Wind Generated Water Waves, *Journal of Physical Oceanography*, 5, pp. 410-420, 1975.

Kraus, N.C. and J.M. Smith, Supertank Laboratory Data Collection Project, *U.S. Army Corps of Engineers Coastal Engineering Research Center, Technical Report CERC-94-3*, pp. 1-38, Vicksburg, Miss., 1994.

Kreibel, D.L., Personal communication, 1994a.

Kreibel, D.L., Supertank Laboratory Data Collection Project, *U.S. Army Corps of Engineers Coastal Engineering Research Center, Technical Report CERC-94-3*, pp. 74-91, Vicksburg, Miss., 1994b.

Mase, H. and J.T. Kirby, Hybrid Frequency-Domain KdV Equation for Random Wave Transformation, in *Proceedings of the 23rd International Conference on Coastal Engineering*, pp. 474-487, American Society of Civil Engineers, New York, 1992.

Nwogu, O., Alternative Form of Boussinesq Equations for Nearshore Wave Propagation, *Journal of Waterway, Port, Coastal and Ocean Engineering*, 119, pp. 618-638, 1993.

Sand, S.E., *Stochastic Processes: Practical Computation of Spectra*, Danish Hydraulic Inst., 1986.

Shemdin, O.H., K. Hasselman, S.V. Hsiao and K. Herterich, Nonlinear and Linear Bottom Interaction Effects in Shallow Water, in *Turbulence Fluxes through the Sea Surface, Wave Dynamics and Prediction*, pp. 347-372, Plenum, New York, 1978.

Smith, J.M., Nonlinear Shoaling of Double-Peaked Wave Spectra, *Term Project: CE872*, University of Delaware, 1990.

Synolakis, C.E., The Runup of Solitary Waves, *Journal of Fluid Mechanics*, 185, pp. 523-545, 1987.

Thompson, E.F. and M.J. Briggs, Surf Beat in Coastal Waters, *U.S. Army Corps of Engineers Coastal Engineering Research Center, Technical Report CERC-93-12*, pp. 40-62, Vicksburg, Miss., 1993.

Thornton, E.B. and R.T. Guza, Transformation of Wave Height Distribution, *Journal of Geophysical Research*, 88, C10, pp. 5925-5938, 1983.

Veeramony, J., Personal communication, 1994a.

Veeramony, J., Propagation and Breaking of Wave Groups, Master's thesis, Department of Civil Engineering, University of Delaware, 1994b.

Wilson, B.S., in *Encyclopedia of Oceanography*, Academic Press, New York, 1966.

Yoon, S.B., Propagation of Shallow-Water Waves Over Slowly Varying Depth and Currents, Doctoral dissertation, Department of Civil Engineering, Cornell University, 1987.

Zelt, J.A., The Runup of Nonbreaking and Breaking Solitary Waves, *Coastal Engineering*, 15, pp. 205-246, 1991.